UNIVERSITETET
I OSLO

Thesis for Master of Science

Noble bimetallic surfaces relevant for the ammonia oxidation process

Alexandra Jahr Kolstad

Materials Science for Energy and Nanotechnology
60 credits

Department of Chemistry
Faculty of Mathematics and Natural Sciences

2022

Noble bimetallic surfaces relevant for the ammonia oxidation process

Alexandra Jahr Kolstad

http://www.duo.uio.no/

Printed at Reprosentralen, University of Oslo

Abbreviations

AES	Auger Electron Spectroscopy
AP	As prepared
bcc	Body centered cubic
BE	Binding energy
CHA	Concentric hemispherical analyser
EBE	Electron beam evaporator
fcc	Face centered cubic
FWHM	Full width at half maximum
hcp	Hexagonal close packed
LEED	Low-Energy Electron Diffraction
OX	Oxidation
PA	Post annealed
QMS	Quadrupole Mass Spectrometer
RT	Room temperature
sc	Simple cubic
STM	Scanning Tunneling Microscope (Microscopy)
TOF-ICISS	Time-Of-Flight Impact-Collision Ion Scattering Spectroscopy

UHV	Ultra-high vacuum
UiO	University of Oslo
XPS	X-ray Photoelectron Spectroscopy (Spectrometer)

Abstract

This thesis is dedicated to surface science investigations of bimetallic platinum (Pt)-based materials relevant for industrial ammonia oxidation reactions. In the first part, sub-nm thick platinum rhodium (PtRh) films were prepared *in situ* on a Pt(111) crystal and explored using a *Scanning Tunneling Microscope* (STM) for the purpose of investigating oxidation properties the surfaces. High coverage deposition of Rh (over 1.5 monolayer (ML)) on Pt(111) at temperatures in the range 350 – 450 K were prepared, and subsequently post annealed at temperatures of 600 – 700 K. The resulting surfaces after post annealing showed a new surface reconstruction; *the honeycomb pattern*. Comparison with the previous results on Pt/Rh(111) and Rh/Pt(111) obtained at the same ReactorSTM lab, showed that the honeycomb reconstruction appeared as a result of high Rh coverage. It was found to be unaffected by crystal temperature and post annealing temperature. A roadmap was made to summarize the resulting high coverage Rh/Pt(111) surfaces after preparation and post annealing at variable temperatures. Further oxidation of the surfaces at 600 K in 10^{-3} mbar led to a wide range of results which depended on the temperature of the previous preparation. It was concluded that lower deposition and post annealing temperature is crucial for oxide formation, in agreement with previous literature.

The second part of the work is dedicated to platinum palladium (PtPd) films and bulk samples investigated with STM and *X-ray Photoelectron Spectroscopy* (XPS), respectively, to investigate the properties of the surface as a Pt catchment material in the ammonia oxidation process.

As prepared sub monolayer Pd/Pd(111), Pt/Pd(111), and Pd/Pt(111) surfaces were studied in an STM as a function of deposition temperature, coverage, and the deposition material (Pd and Pt). The bare Pd(111) single crystal had a lot of dirt present during scanning. Therefore, it was concluded that the applied cleaning procedure was not sufficiently optimized to produce a reliable, clean surface. Surprisingly, for the bimetallic surfaces, little to no literature were found on the surfaces at the time of writing. Overall, all three surfaces featured a 3D growth of layers, numerous defects, and irregular shaped islands. Interestingly, following literature procedure, oxidation of Pd/Pt(111) surfaces at 700 K in a partial pressure of oxygen gas ($p(O_2)$) of 10^{-7} and 10^{-5} mbar did

not produce oxides. This is in contrast with a reported Pd-O surface phase diagram, which presents formation of PdO bulk at the applied conditions.

In the last section of the thesis, bulk PtPd samples were studied with an XPS equipped with a chemistry cell for the purpose of studying the surface composition in an oxidative environment. The six samples denoted Pt_xPd_{100-x} ($x = \{0.5, 10, 27, 50, 90, 100\}$), which are shortened to Pt_x or Pt*x*, were subjected to a treatment consisting of two oxidation steps at 0.21 bar: 1) oxidation at 900 °C, and 2) oxidation at 500 °C, with a cleaning procedure performed before each oxidation, and subsequently scanned. For the oxidation at 900 °C, only the lowest Pt content alloy, Pt0.5, had formed PdO. This is not expected through a previously reported Pd-O surface phase diagram. In contrast, after oxidation at 500 °C, all alloys formed PdO and PtO, and the two highest Pt content alloys, Pt50 and Pt90, additionally formed PtO_2. It was therefore concluded that Pd content is a prerequisite for a PtPd alloy to oxidize in these conditions. Similarly, only higher Pt content samples formed PtO_2. For Pt50 and higher Pt content samples, it is hypothesized that the adsorbed O is a precursor to oxide formation, specifically PtO_2.

Acknowledgements

The work presented in this MSc was performed at the NAnostructures and FUnctional MAterials (NAFUMA) research group at the Department of Chemistry, Faculty of Mathematics and Natural Sciences at the University of Oslo, lasting from August 2020 to November 2022.

I would firstly like to thank my supervisors Anja O. Sjåstad and Oleksii Ivashenko for allowing me to work on this MSc thesis. Learning about the world of surface chemistry and STM has been more interesting than I hoped for. Thanks you for the guidance and the laughs, especially by naming yourself old people.

Secondly, I would like to mention all the friends I have made during the bachelor and master at UiO. The social community at UiO has been incredibly important in order to withstand all the trials endured, both personal and as a consequence of choosing a niche field.

Thirdly, my family for all the love and support in my life. You have given me the motivation to continue and be stubborn in the face of challenge.

Lastly, I would like to thank Yani. You are both my rock, my ground, and my personal destresser. I cannot image being where I am without you.

Table of contents

1 Introduction

PtRh and PtPd alloys are well-known for their catalytic properties, especially used in the ammonia oxidation in the Ostwald process for fertilizer production. PtRh is for instance used as the catalyst for the ammonia oxidation reaction [1], while Pd-alloys, for instance PtPd, are used as Pt catchment gauzes in this reaction [2]. The significance of Pt catchment will be examined by first exploring the fertilizer production, then continuing into the Ostwald process.

The following sections will focus on the properties of Pt, Rh, and Pd relevant for Pt catchment. Firstly, relevant phase diagrams will be presented. Secondly, PtRh and PtPd surfaces investigated using *Scanning Tunneling Microscopy* (STM) reported in literature are presented in separate Sections. Finally, the chemical state of Pt and Pd surfaces reported using *X-ray Photoelectron Spectroscopy* (XPS) in literature are presented.

Lastly, the motivation of the thesis is presented in Section 1.9.

1.1 The importance of fertilizer production

Fertilizers are one of the most crucial technological advancements in modern society. The invention of synthetic nitrogen fertilizers through ammonia production gave Fritz Haber the Nobel prize in chemistry in 1918 and Carl Bosch in 1931 for reproducing the process at an industrially large scale [3]. Today, without synthetic nitrogen fertilizers produced industrially via the Haber-Bosch process, half the population of the world would not be fed [4]. The Haber-Bosch process is, in general terms, reacting N_2 with H_2 to produce ammonia, NH_3, see Section 1.2. Figure 1.1 demonstrates the need of fertilizers for the world population from 1900 to 2015. It is also worth noting in Figure 1.1 that industrial production of synthetic nitrogen-based fertilizers increased significantly at the beginning of the 1960's, leading partly to a boom in population with a steady, nearly linear increase. Taking all these points into consideration, it would not surprise anyone that the Haber-Bosch process is widely recognized as one of the most important inventions in the last century, or even for the humankind through all ages [5].

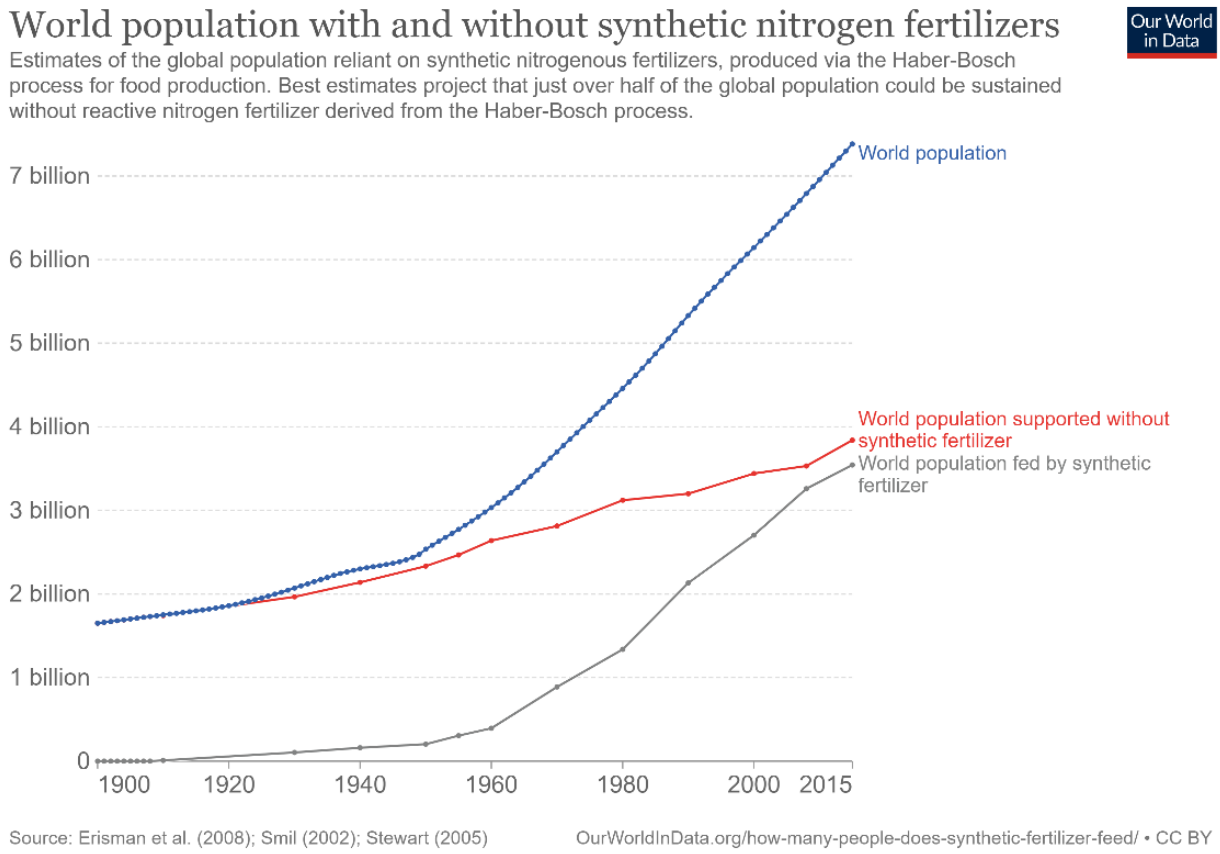

Figure 1.1: The importance of nitrogen-based fertilizers in terms of world population. The figure is taken from [4].

1.2 Basics of nitrogen-based fertilizer production

To describe the fertilizer production, it can be useful to base the explanation on a well-known nitrogen-based fertilizer production company. Globally, Yara International is the largest producer of nitrogen based mineral fertilizers, with its headquarters, research centre, and a big production site at Herøya, Norway. Yara makes multiple kind of mineral fertilizers. Their most common types are based on nitrogen, phosphorus, and potassium. Figure 1.2 below describes the production of these three main types of fertilizers in flow chart form.

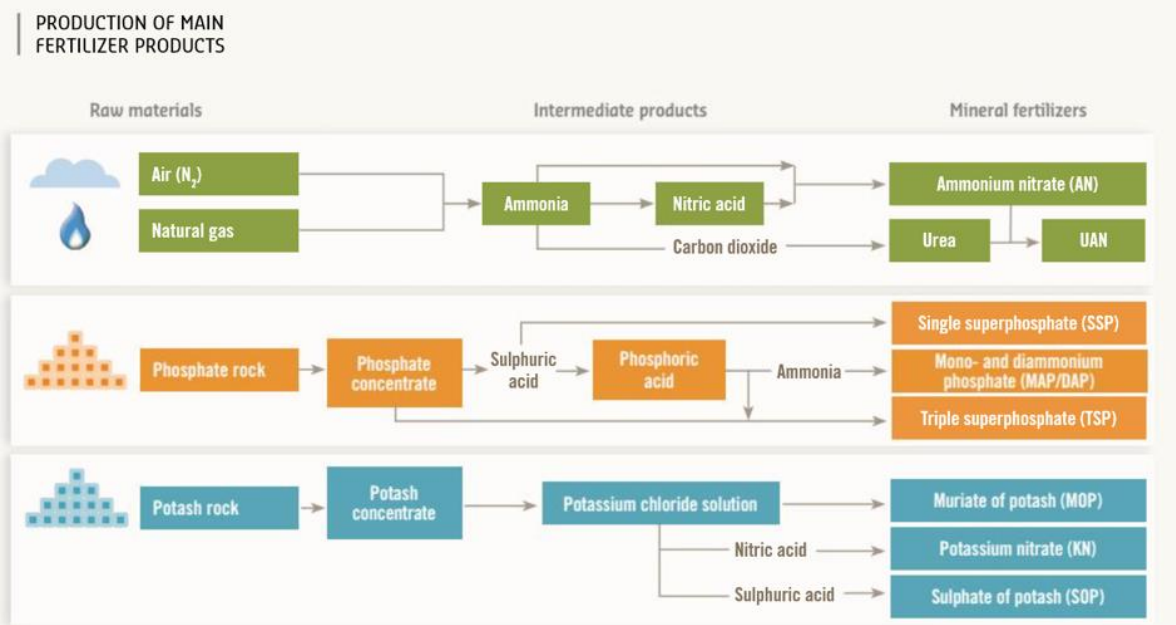

Figure 1.2: Flow chart for mineral fertilizer productions, based on nitrogen, phosphorus, and potassium. The illustration is taken from [6].

Nitrogen based fertilizers is the most common type of fertilizer in the world [4]. At Yara International, their nitrogen fertilizers are produced from natural gas, mainly methane, CH_4. During several steps methane is transformed to hydrogen-gas, H_2, which is in turn combined with nitrogen from the air, N_2, to form ammonia, NH_3. Here the Haber-Bosch process is employed; see Equation 1.1.

$$3H_2(g) + N_2(g) \rightleftharpoons 2NH_3(g) \qquad 1.1$$

The process is reversible and exothermic [7], with a standard enthalpy change is approximately $\Delta H_r^0 = -92.4\ \mathrm{kJ/mol}$ [8]. According to the Le Châtelier principle, the production of ammonia is favoured at lower temperatures and higher pressures. Therefore, to produce as much ammonia as possible the pressure should be as high as possible and the temperature as low as possible. The compromise for the process conditions typically used are approximately 400 °C and 200 bar [9].

Despite the need of a high energy input for the process to take place, the Haber-Bosch process is the most widely used process for ammonia production [7]. Another disadvantage with the process is that ammonia production alone accounts for 2% of the worldwide energy usage and 1.6% of the CO_2 emissions [3].

There are two main products of nitrogen fertilizer production: ammonium nitrate, NH_4NO_3, and urea, CH_4N_2O or $CO(NH_2)_2$. Urea is made by combining ammonia with carbon dioxide, CO_2, see Equation 1.2 [10, p250].

$$2NH_3(g) + CO_2(g) \rightarrow CO(NH_2)_2(s) + H_2O(g) \quad 1.2$$

Ammonium nitrate is produced by oxidizing ammonia with oxygen, O_2, to from the intermediate nitric acid, HNO_3. This process is performed in multiple steps and is denoted the Ostwald process [10, p250]. Equation 1.3 describes the overall chemical reaction for nitric acid production, starting with the step where ammonia is oxidized. See Section 1.3 for more details.

$$NH_3(g) + 2O_2(g) \rightarrow H_2O + HNO_3(aq) \quad 1.3$$

Then the nitric acid is subsequently combined with ammonia, and the end product is ammonium nitrate, as shown in Equation 1.4.

$$NH_3(g) + HNO_3(aq) \rightarrow NH_4NO_3(s) \quad 1.4$$

As seen from Figure 1.2, ammonium nitrate and urea are often also combined to form the third fertilizer urea ammonium nitrate (UAN) [11,12]. Phosphorus- and potassium-based fertilizers are not discussed further.

1.3 Ammonia oxidation in the Ostwald process

The Ostwald process is another Nobel Prize worthy discovery within chemistry [13]. Wilhelm Ostwald was awarded the Nobel prize in chemistry in 1909 partly for his work within catalysis [13]. Ostwald discovered that by oxidizing ammonia in two steps followed by a reaction with water, the end product would be nitric acid, HNO_3. The three reactions are performed in this order: first, ammonia is oxidized by oxygen from the air. The oxidation of ammonia can give three different end products (NO, N_2, and N_2O), as shown in Equations 1.5 – 1.7 below.

$$4NH_3(g) + 5O_2(g) \rightleftharpoons 4NO(g) + 6H_2O(g) \quad 1.5$$

$$4NH_3(g) + 3O_2(g) \rightarrow 2N_2(g) + 6H_2O(g) \quad 1.6$$

$$2NH_3(g) + 2O_2(g) \rightarrow N_2O(g) + 3H_2O(g) \quad 1.7$$

The three reactions described in Equations 1.5 – 1.7 above are highly exothermic, with an enthalpy change of $-907\ \mathrm{kJ/mol}$, $-1266\ \mathrm{kJ/mol}$, and $-1104\ \mathrm{kJ/mol}$, respectively [14]. The ammonia oxidation process can be optimized for each of the possible oxidation products; thus it can be a highly selective process. This implies that by tuning the conditions for the reaction, for instance temperature and pressure, as well as the chemical composition of the catalyst, it is possible to enhance selectivity toward desired end products. In the case of ammonia oxidation for fertilizer production, nitric oxide, NO, is the desired end product. When the catalyst used is a platinum-rhodium, PtRh, alloy with operating conditions of approximately 900 °C and 1 – 10 bars, ammonia will be oxidized according to Equation 1.5. The selectivity is approximately 90 – 98% for all of the nitrogen to be converted to nitric oxide [15]. Another possible end product is N_2O, nitrous oxide. Nitrous oxide is known as a strong greenhouse gas, along with carbon dioxide. The main significant difference is that N_2O is 300 times more potent to directly contribute to global warming than CO_2 [15]. Nitrous oxide is known to destroy the ozone layer, which indirectly leads to global warming [16]. Furthermore, nitric acid plants are the largest source of nitrous oxide emissions in the chemical industry [17]. Therefore, to supress N_2O release produced from the process to the

atmosphere, a N_2O decomposition catalyst is installed downstream in the HNO_3 production process to clean out the produced N_2O [18].

The next reaction in the Ostwald process is the oxidation of the intermediate product nitric oxide, NO, into nitrogen dioxide, NO_2, see Equation 1.8. This reaction proceeded without adding a catalyst.

$$2NO(g) + O_2(g) \rightleftharpoons 2NO_2(g) \qquad 1.8$$

This reaction to form nitrogen dioxide is also exothermic, but to a much smaller extent. The enthalpy change is $-114\ \mathrm{kJ/mol}$. The third and last reaction is to disproportionate nitrogen dioxide in water to form end product nitric acid and nitric oxide, written in Equation 1.9.

$$3NO_2 + H_2O(l) \rightarrow 2HNO_3(aq) + NO(g) \qquad 1.9$$

Now the end product nitric acid is synthesized. This reaction is also exothermic, with an enthalpy change of $-117\ \mathrm{kJ/mol}$. Nitric oxide formed in Equation 1.9 is recycled back to the oxidation step described in Equation 1.8. In total the Ostwald process can be written as Equation 1.3. All above information is taken from [10, p250].

In this thesis, aiding the first reaction in the Ostwald process is the main focus, shown in Equation 1.5. The catalyst for ammonia oxidation is most commonly PtRh gauzes. The gauze consist of approximately 90 wt.% of Pt and the rest Rh, where 60 – 70 µm threads of the elements are woven into a net [1]. The reaction is performed at 900 °C and 1 – 10 bars. The combination of high temperatures to perform the reaction and the reaction being extremely exothermic, damages the catalyst because of locally very high temperatures. Consequently, hot spots appear on its surface and when sending oxygen over the catalyst to perform the oxidation, platinum will react with the oxygen and sublimate as PtO_2. This gas will then escape from the surface, causing high loss of the valuable noble metal platinum. To negate this effect, Pt catchment nets are implemented downstream [19]. Similarly, hot spots will sublimate Rh to rhodium oxides, RhO_x. Most common

is rhodium dioxide, RhO_2. Unfortunately, there have been less effort to make Rh catchment nets [1].

1.4 Pt catchment in the Ostwald process

The first palladium-based Pt catchment net was invented in 1968 by Hermann Holzmann [20]. It was an alloy consisting of 20 wt.% gold (Au) and 80 wt.% palladium (Pd). These elements were chosen because of a couple of important properties. One property is that the alloy metals should not form oxides in the temperature range where ammonia oxidation of nitric acid, HNO_3, production is performed, which is 900 °C. Another property is that the metals of the net cannot react with the gases in the process gas stream. These gases are for instance, ammonia (NH_3), nitrogen monoxide (NO), oxygen (O_2), and water (H_2O). Lastly, it was important to make the gauze of ductile metals. Originally there were three metals suggested to make the gauze: gold, palladium, and platinum. However, at the time platinum was eliminated because of the steep prize. Holzmann then concluded on making a PdAu alloy, which proved successful and became the predecessor for all Pt catchment nets used in nitric acid plants today.

Today the most used Pt catchment gauzes are Pd and PdNi. For instance, PdNi is commonly used by Yara International. PdNi gauzes are capable of capturing Pt to an extent where around 50 wt.% are Pt [2]. However, the nets are subject to multiple destructive effects. The main degradation effect is grain reconstruction. Fjellvåg *et al.* [19] found that this is caused by the presence of PtO_2 vapour irrespectively of the partial pressure of PtO_2 present in the gas phase. PtO_2 vapour reacts on the Pd or PdNi surface, causing a severe grain reconstruction and formation of PtPd crystals [19]. The extensive grain reconstruction causes wire swelling, loss of mechanical strength, dissolution, and formation of pores for the gauze, and additionally pressure drops in the reactor. Furthermore, nickel metal oxidizes to nickel oxide, NiO, which in turn is transformed to nickel hydroxide, $Ni(OH)_2$. Nickel hydroxide forms as a gas, causing Ni depletion of the Pt catchment gauze. The Ni loss is concluded not to give rise to the heavy reconstruction of the nets, as the same reconstruction occur in Pd nets [19]. All these phenomena combined illustrates the detrimental

effects of the PdNi catchment gauzes, and therefore a need for further research into improvements are called for.

Other Pt catchment materials have also been tested [19]. For instance glass wool and marble chips, although they proved to not be as efficient as gauzes [19]. Recently our research group started up an activity on exploring suitability of various oxide materials. Lanthanum nickelate, $LaNiO_3$, is found to be a good candidate for Pt catchment as recently described in a paper by Hessevik *et al.* [21].

1.5 Relevant phase diagrams

The binary PdPt phase diagram for bulk components is shown in Figure 1.3. Above the liquidus curve, only the liquid phase is present. Between the solidus and the liquidus is a liquid + (Pd,Pt) solid phase. Under solidus is the (Pd,Pt) solid solution phase. Under the dome shown by the dotted line with a maximum temperature of approximately 770 °C, the (Pd,Pt) solid phase separates into two phases consisting of (Pd) + (Pt), one being enriched in Pd and the other enriched in Pt. This dome is still not experimentally proven, which is why it is drawn with a dotted line.

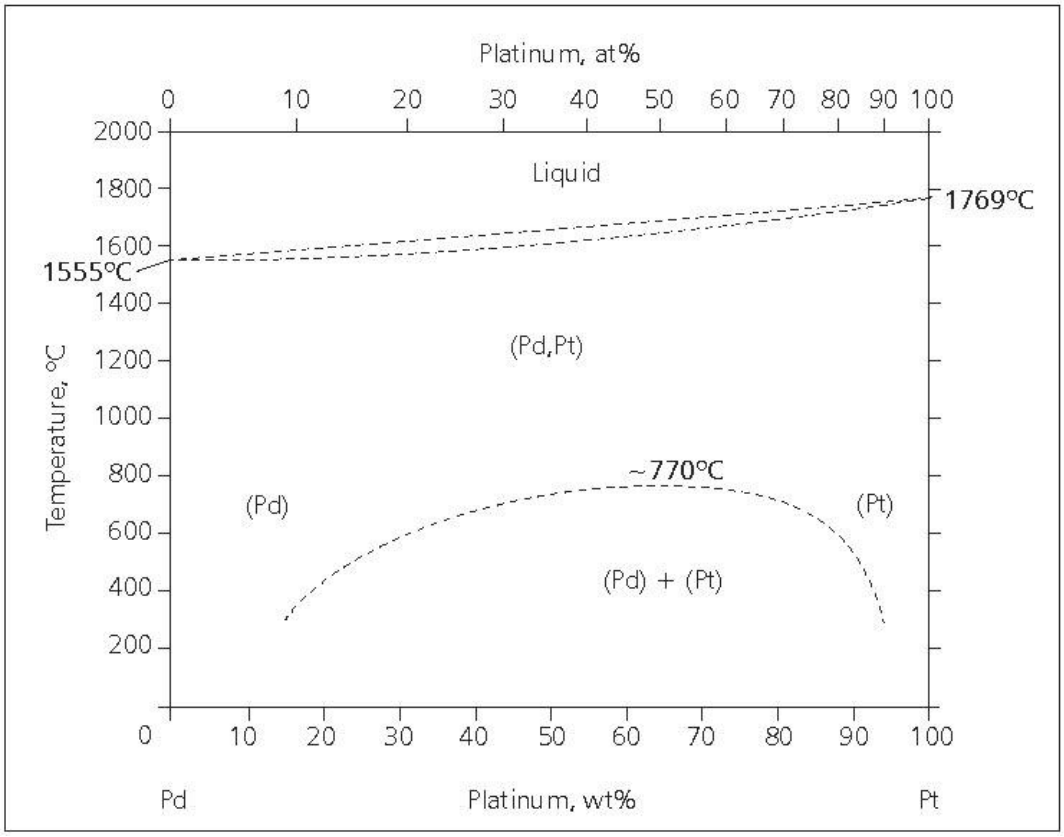

Figure 1.3: The binary phase diagram of the Pd-Pt system. Retrieved from [22].

The surface phase diagram in Figure 1.4 shows the formation of palladium oxides at the surface. For high partial pressures of oxygen and low temperatures (the black region on the phase diagram), a palladium bulk oxide, PdO, is formed. An increase in temperature over the entire $p(O_2)$ region, a surface oxide $\sqrt{6} \times \sqrt{6}$ is formed (green region). At even higher temperatures, the surface chemisorbs oxygen, and the oxygen layer O(2×2) is formed (pale red region). At the highest temperatures no oxygen layers are formed, neither as oxide nor chemisorbed oxygen, so the surface is metallic Pd(111) (white region). The larger the partial pressure of oxygen is, the more stable all oxygen layers are at higher temperatures. Lower pressures decrease the stability of the oxygen layers.

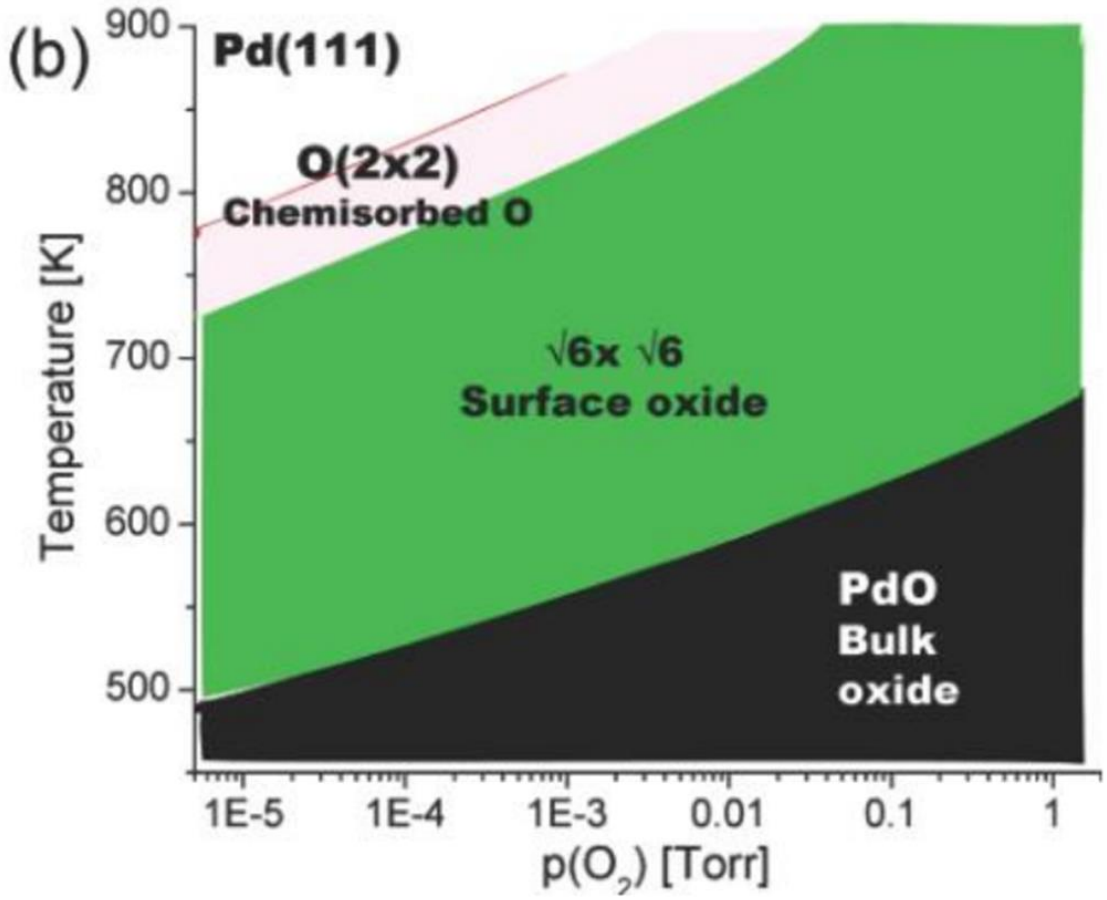

Figure 1.4: The temperature (K) – $p(O_2)$ (torr) surface phase diagram of Pd(111). Retrieved from [23].

1.6 PtRh alloys in literature at University of Oslo

This thesis is part of a larger effort in the NAFUMA research group at University of Oslo on developing understanding of PtRh nanostructured surfaces at ultra-high vacuum (UHV) and variable oxygen containing conditions. The work is reported in three scientific publications and one MSc thesis [24–27] . In the following, a short review of this literature is given.

1.6.1 Roadmap for Modelling Rh/Pt(111) Surfaces

The first paper published on PtRh systems at the ReactorSTM lab at the University of Oslo is "*Roadmap for Modeling RhPt/Pt(111) Catalytic Surfaces*" by Zheng *et al.* [24] in 2018. In this work a series of distinct Rh/Pt(111) model surfaces were prepared to pave the way for developing optimized PtRh-alloyed catalysts and explain the role of Pt and Rh for future intermediate-temperature ammonia oxidation operando studies.

Zheng *et al.* used a Pt(111) single crystal cleaned by repetitive sputtering and annealing cycles, prepared with subsequent Rh deposition by means of Electron Beam Evaporator (EBE) at room temperature (RT) and select temperatures in the range 300 – 700 with coverages of 0.2 to 0.92 ML. Samples prepared at RT were post annealed (PA) at temperatures of 400 – 1050 K for 5 min. Samples prepared at higher deposition temperatures were often flash annealed at 450 – 750 K. Pt was evaporated at RT on the Pt(111) crystal with a coverage of 0.38 ML, and subsequently post annealed, with the conditions mentioned above for PA of Rh/Pt(111), to compare between the effect of post annealing for Rh/Pt(111) and Pt/Pt(111).

The resulting surfaces were summarized in Figure 1.5, which has been built upon by Pettersen *et al.* [27]. Further information is found in Section 1.6.4. The top panel of images visualizes surfaces prepared at room temperature with subsequent annealing, while the bottom panel shows surface prepared at higher temperatures with subsequent annealing. Zheng *et al.* found multiple different island morphologies for both deposition at higher temperatures and RT. The most common shapes are triangles and hexagons. Triangles are formed at mostly lower temperatures, while hexagons are formed at higher temperatures. High temperature deposition and post annealing was compared because high temperature promotes mixing of Pt and Rh. The most notable discovery in the paper is that RT deposition resulted in the most stable ad-islands after high temperature post annealing. Additionally, high temperature deposition without post annealing is not enough to form hexagonal islands. The optimal post annealing temperature for good Pt and Rh mixing was found to be 550 ± 50 K. The surface morphologies can furthermore be varied by means of coverage. The morphologies obtained were triangles, hexagons, worms, and domains between 0.2 and 0.92 ML. After deposition at 450 K, small nuclei composed of a couple of atoms were found formed on the surface between the islands.

Because of the wide range of ad-island morphologies obtained by simple adjustment of the preparation conditions, Zheng *et al.* predicts these surfaces to be useful for optimization of catalytic PtRh alloys.

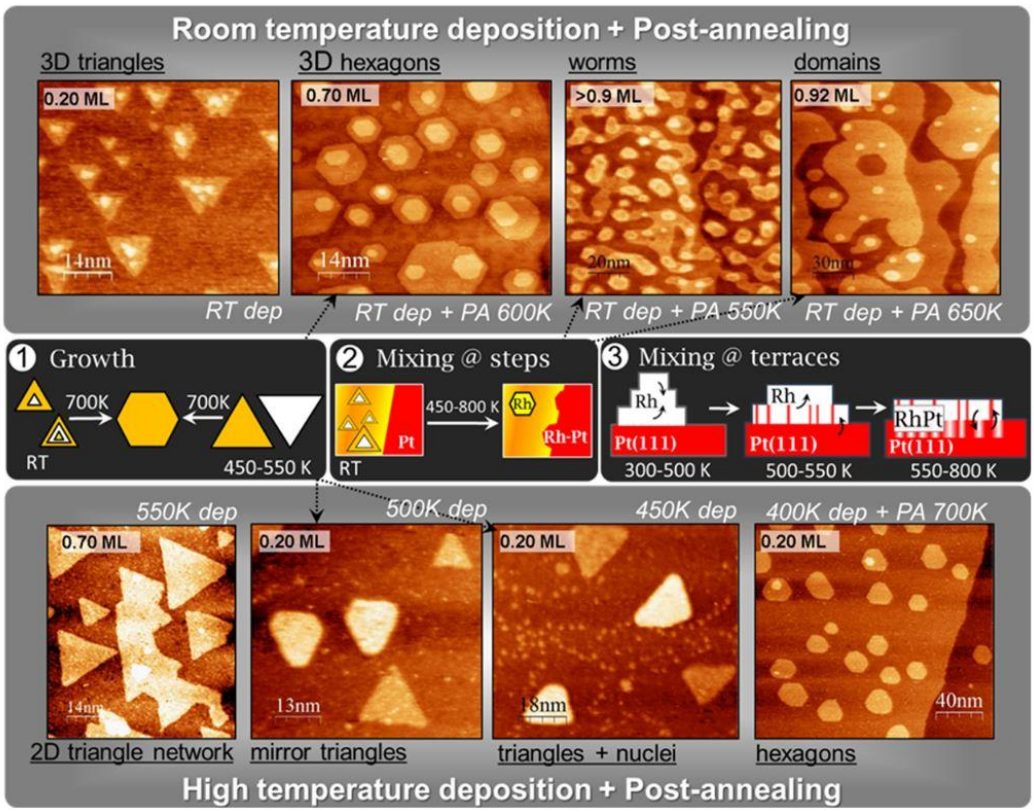

Figure 1.5: Roadmap of how to prepare various PtRh alloy island morphologies on Pt(111). Retrieved from Zheng *et al.* [24].

1.6.2 Pt/Rh(111) and Rh/Pt(111) surfaces studied by STM and NAP-XPS

The motivation of the MSc thesis "*Preparation, Characterization and Oxidation of Nanostructured Pt-Rh Surfaces*" by Pettersen [25] was "to utilize surface sensitive techniques to understand the role of how elemental mixing and morphology of bimetallic PtRh alloyed surfaces affects interaction with oxygen". The complimentary systems Pt/Rh(111) and Rh/Pt(111) were examined using STM, ReactorSTM, *Near Ambient Pressure XPS* (NAP-XPS), and *Low-Energy*

Electron Diffraction (LEED), operated in the pressure regime from UHV to ambient oxygen pressure.

The STM experiments were solely performed on the Rh(111) single crystal. After repetitive cleaning cycles, Pt was evaporated in the temperature range of 300 – 700 K with a coverage in the range of 0.1 to 2.3 ML. Subsequent post annealing were performed in the range 600 – 700 K for 5 – 10 min. Some samples were additionally oxidized at 700 K for 20 min in $1 \cdot 10^{-3}$ mbar O_2. Additionally, both clean Rh(111) and Pt/Rh(111) were prepared and scanned during oxidation *in situ* with an O_2 partial pressure of 1 bar.

NAP-XPS were performed on a cleaned Pt(111) single crystal. After cleaning, Rh was evaporated at 360 K in UHV with coverages of 0.4, 0.5, and 1.2 ML. All the samples were then post annealed at 600 – 770 K for 5 – 20 min. The NAP-XPS experiments, carried out at MAXIV, were performed at 1 mbar O_2 at 600 K.

Pettersen concludes that the choice of the starting substrate, whether Pt(111) or Rh(111), dictates the preparation steps performed for the desired oxidation of the PtRh systems. This is because the oxidation process is determined by the amount of Rh located at the surface. When the substrate is Pt(111), the amount of Rh metal at the surface can be controlled by the temperature used for both the deposition and the post annealing, because higher temperatures cause Pt to diffuse to the surface, therefore forming PtRh alloys. If the substrate is Rh(111), the amount of PtRh oxides formed is easily controlled by the amount of Pt deposited. A summary of how to prepare the surfaces is given in Figure 1.6 below, as well as the roadmap in Figure 1.7. Pettersen report two different oxygen structures in the condition ranges used: a surface oxide and oxygen chemisorbed to the surface. The temperature used for PA in this thesis, 600 K and 700 K, should result in surface oxide formation for a Rh/Pt(111) surface. However, she found that oxide formation is hindered by a large extent of alloying, because the amount of Rh on the surface determines the amount of oxides formed. Furthermore, the amount of Rh on the surface was found to be controlled by the PA temperature. Lastly, in agreement with the literature on oxidation of Rh(111), Pettersen presented that formation of a Moiré pattern is an indicative of oxide formation.

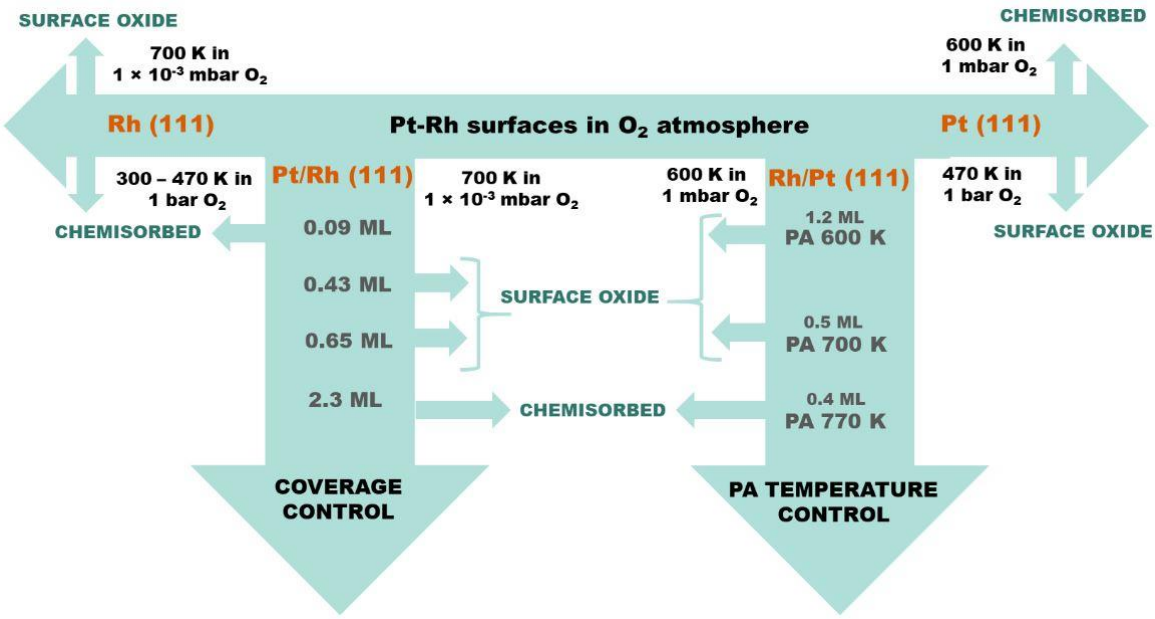

Figure 1.6: Summary of how to prepare PtRh surfaces to form specific oxygen structures on either Pt(111) or Rh(111). Retrieved from Pettersen [25].

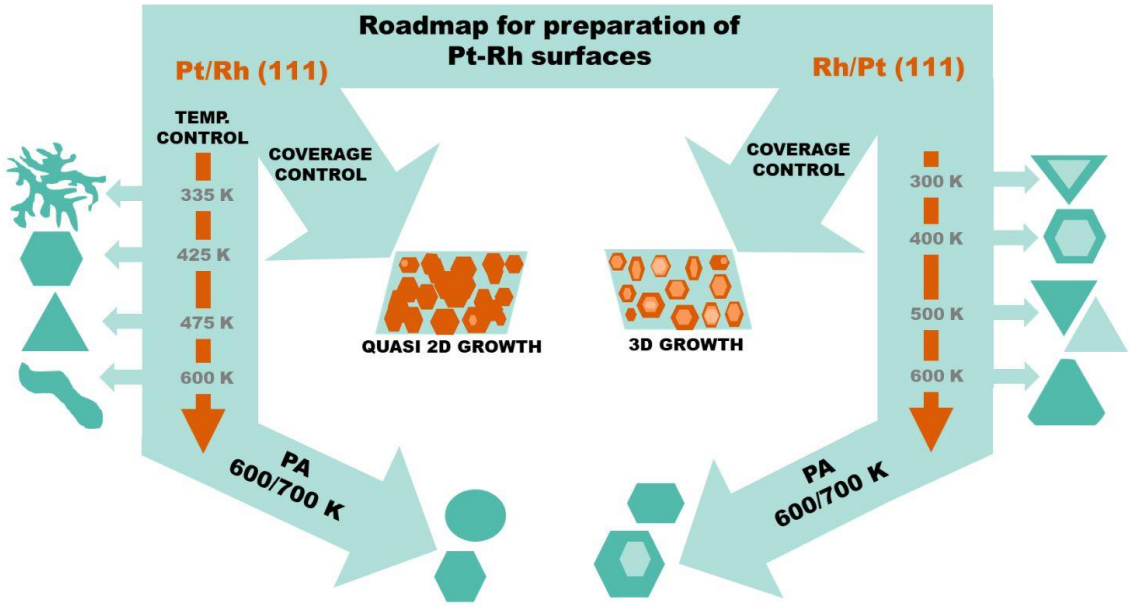

Figure 1.7: Roadmap on how to prepare both the Pt/Rh(111) system and the complementary Pt/Rh(111) system. The map is a further expansion of the roadmap reported by Zheng *et al.* [24]. Retrieved from Pettersen [25].

1.6.3 STM and operando NAP-XPS study on Rh/Pt(111) surfaces

In 2021, the ReactorSTM lab published the paper titled "*How Surface Species Drive Product Distribution during Ammonia Oxidation: An STM and Operando APXPS Study*" by Ivashenko *et al.* [26]. The purpose of this study was "to understand the behaviour of PtRh alloys, namely, what is their active phase under reaction conditions and how the alloy composition leads to a particular product distribution, we study the oxidation of ammonia over PtRh/Pt(111) surfaces by simultaneous operando ambient pressure X-ray photoelectron spectroscopy and mass spectrometry at 1 mbar total reaction pressure". STM topographic images were used to examine the morphology of clean, prepared, and oxidized surfaces.

A Pt(111) single crystal was firstly cleaned by repetitive sputtering and annealing cycles, before evaporation of Rh at 375 K giving coverages of 0.5 and 1.2 ML. Subsequent post annealing were performed at temperatures up to 770 K. Samples used for NAP-XPS were additionally exposed to either 1 mbar O_2 or 1 mbar O_2 + NH_3 mix (99:1 or 50:50) at 600 K.

Ivashenko *et al.* first concludes that the post annealing temperature, i.e., the Rh enrichment at the surface, determines what oxygen-rich structures are formed. The second conclusion is that the structures formed during ammonia oxidation are largely dependent on the gas mix, as well as the annealing temperature. The 99:1 mix results in oxygen structures that closely resembles those formed during oxidation of pure O_2. An oxygen-rich oxidation drives the ammonia oxidation products towards NO, while the 50:50 mix results in N_2. If the atomic N coverage on the surface is too low, the N_2 will be further oxidized to NO. The obtained STM surfaces after preparation at 375 K and PA at 700 or 600 K are depicted in Figure 1.8.

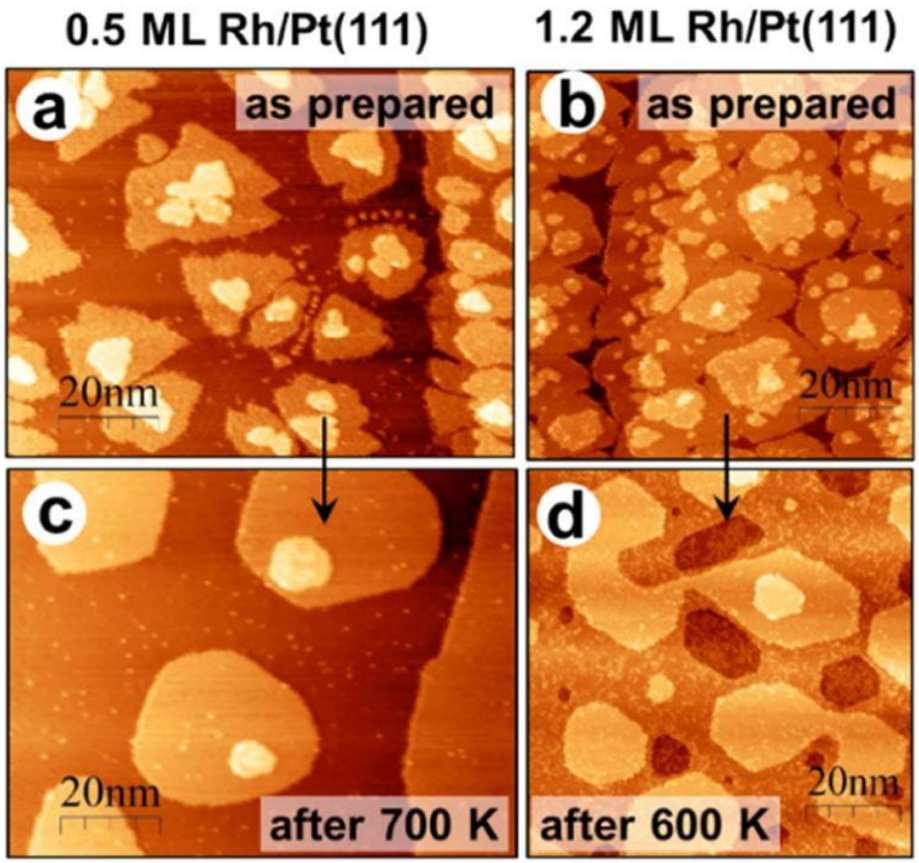

Figure 1.8: The STM surfaces obtained by Ivashenko *et al.* of AP at 375 K and PA at 700 or 600 K of 0.5 and 1.2 ML Rh/Pt(111) surfaces. Retrieved from [26].

1.6.4 Reconstructions of as prepared Rh/Pt(111) and Pt/Rh(111) surfaces characterized by STM

The most recent paper published by NAFUMA research group is "*Near-Surface Alloys of PtRh on Rh(111) and Pt(111) Characterized by STM*" by Pettersen *et al.*, in late 2021 [27]. The purpose of the study was to "investigate the growth, elemental nanostructuring, and reconstruction behaviour of various Pt-Rh near-surface alloys (NSA) on fcc Rh(111) and Pt(111)".

Clean Pt(111) and Rh(111) single crystals were prepared with deposition of either Pt or Rh at temperatures of 300 – 700 K with coverages of 0.2 ML. The subsequent post annealing was performed at 600 – 700 K for 5 – 10 min.

Figure 1.9 is a roadmap of the possible PtRh (near-) surface alloys after deposition. Multiple different surface reconstructions and alloys islands shapes can be obtained at different temperatures. Most notably, for surfaces prepared between 400 – 500 K, *ad-island* reconstruction is formed for Pt/Rh(111), and *network* reconstruction is formed for Rh/Pt(111). In both scenarios, Pt is compelled to reconstruct if Rh is present either as the substrate or as the deposited metal. The ad-island reconstruction of Pt/Rh(111) was found to not be associated with PtRh mixing. The island reconstruction is formed due to strain of the larger Pt lattice deposited on the smaller Rh lattice. Pt rows is shifted slightly upwards, in the range 0.01 – 0.09 nm, because of the lattice mismatch, resulting in formation of a lamellar domain structure. Furthermore, the reconstruction demonstrates a high thermal stability due to its formation in a larger temperature range. The domains are separated by 0.7 ± 0.1 nm wide boundaries and the atom rows are approximately 3.5 nm in length on average, with a periodicity 4.44 nm per 10 rows. In contrast, the Rh/Pt(111) network reconstruction was found to occur because of Rh integration into the Pt surface, which results in either localized surface alloys or localized near-surface alloys. Additionally, in this temperature range, the deposited metal prefers to remain at the surface. This reconstruction is formed due to strain, because Rh tends to go subsurface into the Pt(111) substrate. Small nuclei are formed along the strain lines, which eventually induce the reconstruction through nucleation at the strain lines. The network reconstruction is formed on Pt terraces and surrounds the Rh islands, in a seemingly hexagonal mesh. The reconstruction consists of double rows of small nuclei lifted approximately 0.02 nm with a spacing of 2.5 ± 0.5 nm. There is seemingly no periodicity to the structure because the double lines appear as straight lines with rotors (Rc and Rcc), stars (S), and elbows (E), which bend the lines in what looks like a random pattern. Figure 1.10 is retrieved from Pettersen *et al.*, and showcases the formation of network reconstruction of 0.2 ML Rh/Pt(111) surfaces at four different temperatures: 450, 500, 525, and 550 K. The surfaces prepared at 450, 500, and 525 K show the small nuclei formed along the three crystallographic symmetry directions. The surfaces prepared at 525 K show that the nuclei have started to form the network reconstruction, while the 550 K surface has completely converted all nuclei to the double-lined reconstruction.

An alternative route for well-mixed bimetallic islands was found to be co-deposition of Pt and Rh on either crystal, as this will produce surface alloys during the preparation.

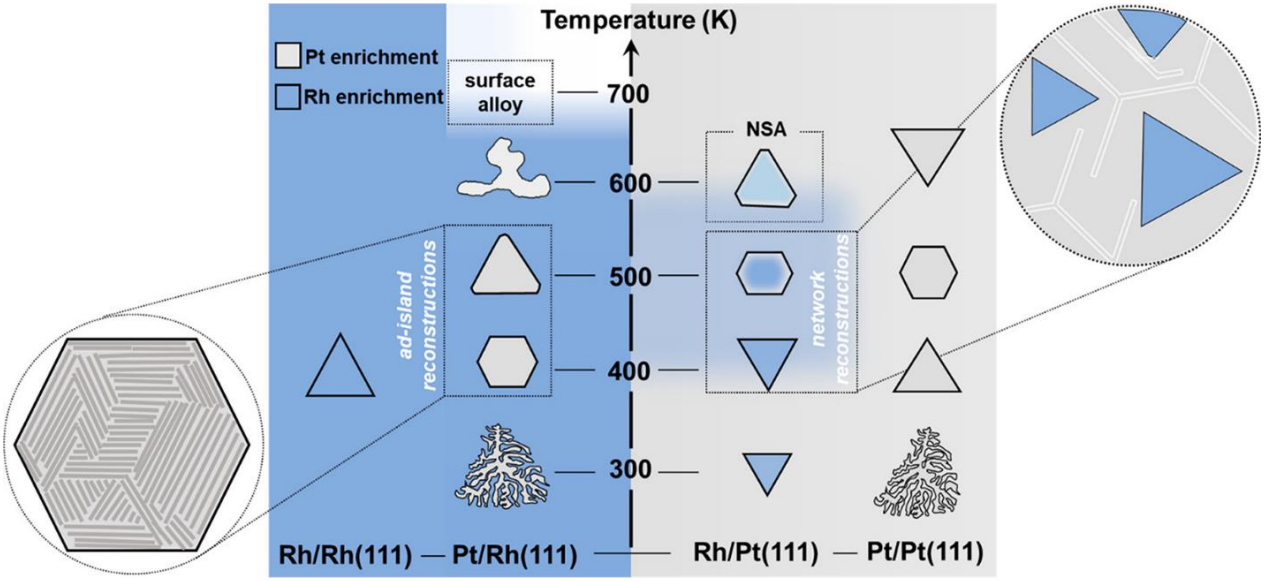

Figure 1.9: Morphology-mixing-reconstruction roadmap of as prepared PtRh (near-) surface alloys of low coverage surfaces prepared on Rh(111) and Pt(111). Retrieved from Pettersen *et al.* [27].

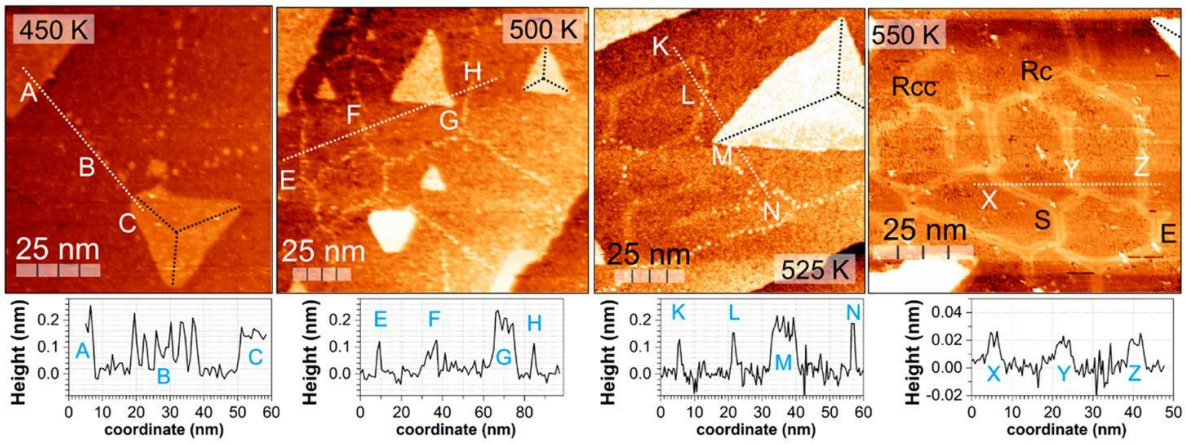

Figure 1.10: STM images and corresponding height profiles of four 0.2 ML Rh/Pt(111) surfaces prepared at different temperatures: 450, 500, 525, and 550 K, respectively. Retrieved from [27].

1.7 Morphology of PtPd alloys using STM

Few studies explore the PtPd system using a STM. Unfortunately, no literature examining Pd/Pd(111) and Pt/Pd(111) surfaces in a STM were found at the time of writing this thesis. However, two papers about as prepared (AP) Pd/Pt(111) surfaces were found. These two papers will thus be the main source of literature for the PtPd system.

1.7.1 STM study of Pd/Pt(111) surfaces

The earliest paper on Pd/Pt(111) as prepared (AP) surfaces, to the best of our knowledge, was written by Narihiro *et al.* [28] and published in 2007, titled "*Scanning Tunneling Microscopy Study of Pd Adsorption on Pt(111)*", which studies the adsorption mechanisms of Pd on a Pt(111) single crystal. The motivation was to study the growth mechanism and perform a structural characterization at the atomic layer of a Pd overlayer, here chosen with a Pt(111) substrate. As they explain, "the activity of palladium overlayers depends strongly on the surface structure", thus such studies are essential to understand the activity of palladium overlayers.

They cleaned a Pt(111) single crystal through repetitive cleaning cycles consisting of ion sputtering and annealing. After the crystal was clean, Pd was evaporated at room temperature (298 K) at a rate of $7 \cdot 10^{-3}$ ML/min, giving coverage between 0.043 and 0.73 ML. The surfaces were scanned using STM in room temperature.

The scanned surfaces are presented in Figure 1.11. The images are varied through coverage and the scale is not identical for all images. The coverage and scale of the six images are: **a)** 0.043 ML, 93 nm; **b)** 0.13 ML, 93 nm; **c)** 0.23 ML, 60 nm; **d)** 0.34 ML, 60 nm; **e)** 0.57 ML, 60 nm; **f)** 0.73 ML, 93 nm. With increasing coverage, it is clear that Pd prefers to decorate the steps as ad-islands with irregular shapes. At coverages of 0.57 and 0.73 ML, Pd additionally forms islands on top of the underlaying terraces. These islands are indication of formation of a second layer before the first layer of Pd coverage is completed. The second layer is facilitated because of the increasing number of defects, seen as holes in the terraces, with increasing coverage.

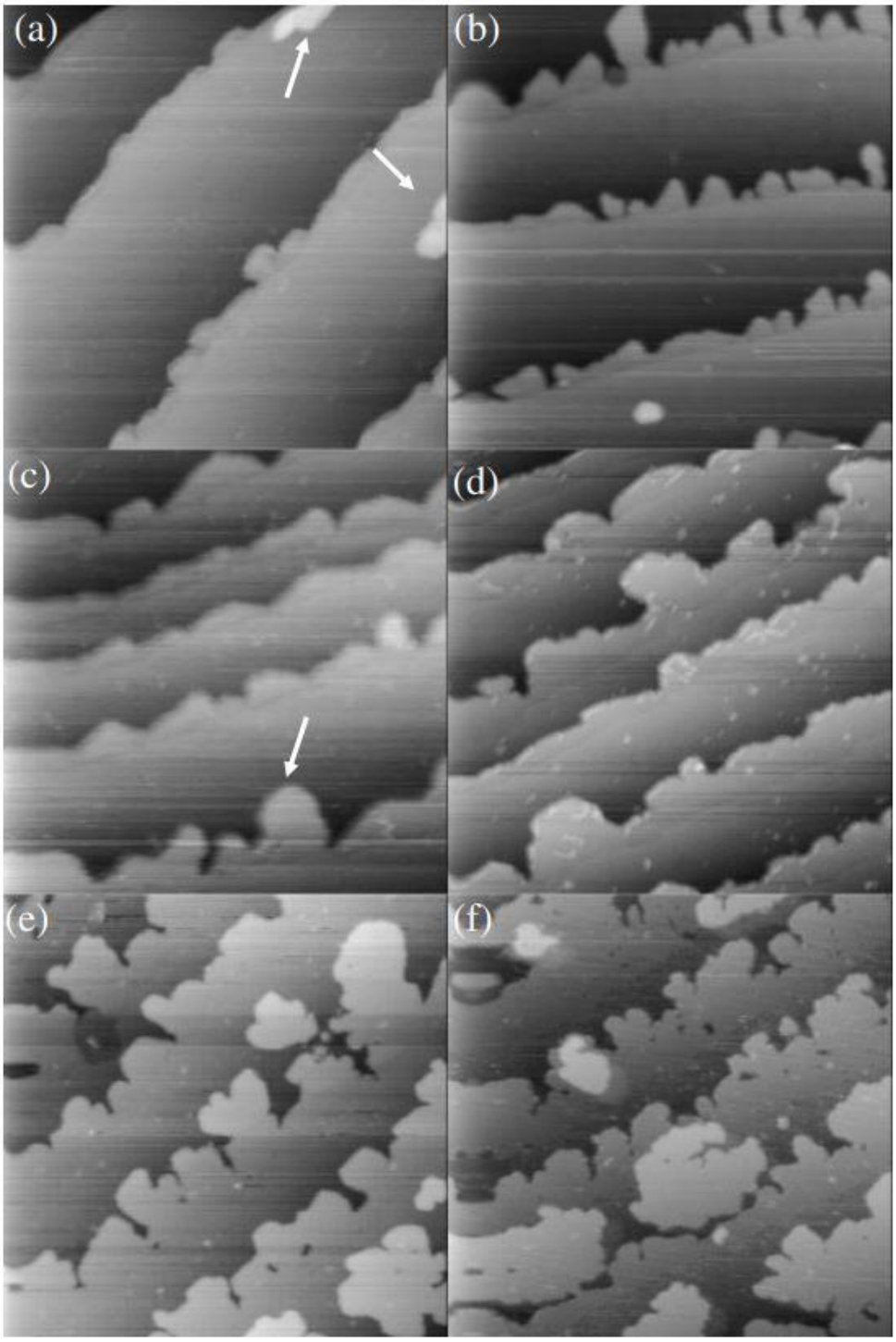

Figure 1.11: STM images of as prepared (AP) Pd/Pt(111) surfaces after evaporation of Pd at room temperature (298 K). The coverage and scale of all images are: **a)** 0.043 ML, 93 nm; **b)** 0.13 ML, 93 nm; **c)** 0.23 ML, 60 nm; **d)** 0.34 ML, 60 nm; **e)** 0.57 ML, 60 nm; **f)** 0.73 ML, 93 nm. Retrieved from [28].

1.7.2 Study of growth mode of Pd/Pt(111) using STM and TOF-ICISS

Umezawa *et al.* [29] published the paper "*Pd/Pt(111) surface structure and metal epitaxy by time-of-flight impact-collision ion scattering spectroscopy and scanning tunneling microscopy: Does lattice mismatch really determine the growth mode?*" in 2008, which builds upon the paper of Narihiro *et al.* [28], described in Section 1.7.1. The purpose of this study was to examine the growth mode of Pd/Pt(111). The motivation was because the lattice mismatch between Pt and Pd was found to be insignificant (less than 1.0 %) [28,29]. Such tiny lattice mismatch is commonly indicative of homoepitaxy (layer-by-layer growth mode), which is growth in 1D. However, Narihiro *et al.* found that defects cause new layers to grow without full completion of the previous layer, indicating a 2D or 3D growth mode. The growth mode was investigated using time-of-flight impact-collision ion scattering spectroscopy (TOF-ICISS) and scanning tunneling microscopy (STM). Solely the STM experiments are relevant to this thesis.

The STM experiments were performed on a Pt(111) single crystal, cleaned through repeated cycles consisting of ion sputtering and annealing. Subsequently, the clean crystal was exposed to Pd deposited at room temperature (298 K) at a rate of $7 \cdot 10^{-3}$ ML/min, giving surfaces with Pd coverage between 0.13 and 0.9 ML, and scanned using an STM at room temperature.

The STM images in Figure 1.12 are incredibly similar to the surfaces obtained by Narihiro *et al.*, see Figure 1.11. Both studies show that Pd prefers to decorate the steps, and that with increasing coverage, the number of defects on the terraces increase and results in formation of new Pd layers without completing the previous layers. At 0.90 ML coverage, see image **c)** and **d)**, a third layer of Pd has started forming, without completion of either the first layer or second layer. Umezawa *et al.* concludes that the images show a 3D growth mode of Pd layers on Pt(111). This is further supported by their calculations of surface and interface energies, which concludes that the growth mode that satisfies the equilibrium condition, $\gamma = \gamma_f + \gamma_i - \gamma_s$ (γ_f and γ_s are the surface energies of deposited film and substrate, respectively and γ_i is the interfacial energy), are the 3D growth mode. Umezawa *et al.* concludes that the Pd/Pt(111) surface demonstrates 2D and 3D growth, with no indication of homo epitaxial growth.

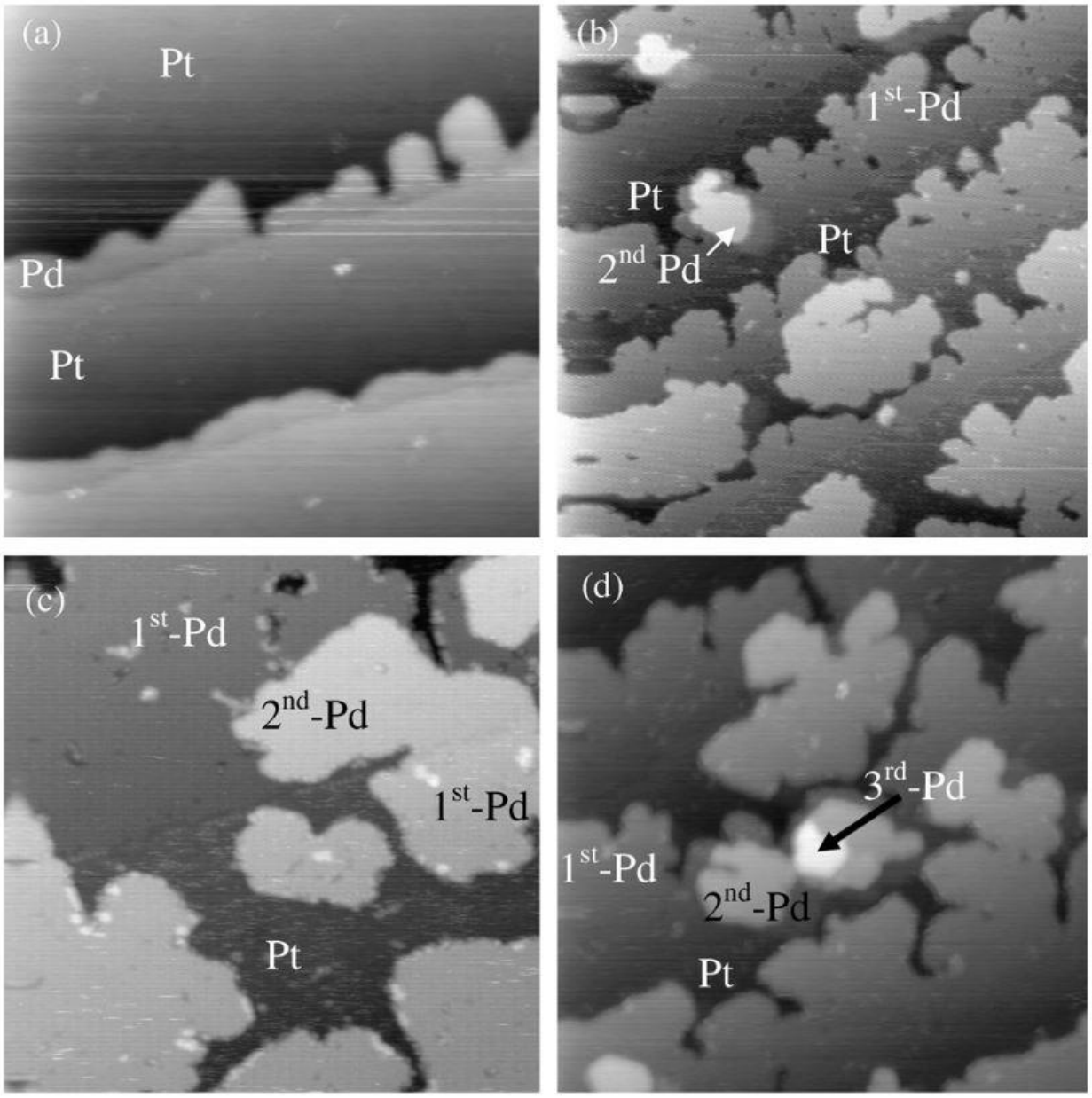

Figure 1.12: STM images of as prepared (AP) Pd/Pt(111) surfaces after evaporation of Pd at room temperature. The coverage and scale of all images are: **a)** 0.13 ML, 60 nm; **b)** 0.73 ML, 92 nm; **c)** 0.90 ML, 32 nm; **d)** 0.90 ML, 60 nm. Retrieved from [29].

1.8 Chemical state of Pt and Pd surfaces by XPS

For the further XPS analysis of oxidation of PtPd alloys, the following sections include a table over reported relevant binding energies (BE) for Pt, Pd, O, and chemical species with these constituents, and their species determined by XPS in Section 1.8.1. Lastly, an extensive summary and overview of the literature is presented in Section 1.8.2.

1.8.1 Relevant Pt and Pd binding energies reported in literature

The binding energies of Pt, Pd, and O species reported in literature are summarized in Table 1.1. The species are categorized under the core level regions they correspond to. Furthermore, the sample and the cleaning or oxidation treatment are presented in accompanying columns. The last column presents the literature the information was retrieved from. This table give a clear overview of the binding energies which are used for comparison with the found binding energies in this experimental work.

Table 1.1: Literary values for core level binding energies for elements Pt, Pd and O. The footnotes represent the cleaning procedure utilized in the respective papers.

Core level region	***Binding energy [eV]***	***Assignment***	***Sample***	***Treatment***	***Ref.***
Pt $4f_{7/2}$	70.5	Pt surface	Pt(111)	Cleaned 1[1]	[30,31]
	70.9	Pt bulk	Pt(111)	Cleaned 1	[30,31]
	71.1	O on Pt	Pt(111)	Up to 5 Torr O_2, 300 K to 720 K	[31]
	71.2	Pt metal	Pt(111)	Cleaned 1	[32]

[1] Cleaned 1 consists of ion sputtering and annealing at various conditions.

	70.9, 71.2	O on Pt	Pt(111)	10^{-7} to 10^{-8} mbar, O_2, room temperature	[32]
	72.3	PtO	Pt(111)	10^{-7} to 10^{-8} mbar O_2, room temperature	[32]
	74.1	PtO_2 bulk	Pt(111)	10^{-7} to 10^{-8} mbar O_2, room temperature	[32]
Pt 4*d*$_{5/2}$	314.2	Pt 4*d*$_{5/2}$ foil	Pt foil	Cleaning 2[2]	[33]
	331.2	Pt 4*d*$_{3/2}$ foil	Pt foil	Cleaning 2	[33]
Pd 3*d*$_{5/2}$	334.9	Pd 3*d*$_{5/2}$ metal	Pd(111)	Cleaned 2 + O_2 flashing	[34]
	335.5, 336.2	Surface 2D oxide Pd_5O_4	Pd(111)	0.4 mbar O_2, 494 K or 501 K	[35]
	335.5, 336.2	Surface 2D oxide Pd_5O_4	Pd(111)	$2 \cdot 10^{-3}$ mbar O_2, 571 K and 598 K	[34]
	335.7	O on Pd	Pd(100)	$2.5 \cdot 10^{-6}$ Pa O_2, 400 K	[36]
	336.3 - 336.4	Surface 2D oxide Pd_5O_4	Polycrystalline Pd foil	RF discharge of 0.2 bar O_2, 2 to 5 min, 300-400 K	[37]
	336.5	PdO bulk	Polycrystalline Pd foil	RF discharge of 0.2 bar O_2, 2 to 5 min, 300-400 K	[37]

[2] Cleaned 2 consists of only ion sputtering at various conditions.

336.7	PdO 3$d_{5/2}$	High purity Pd foil	600 °C, 1 h, O_2	[38]
336.55	PdO bulk	Pd(111)	0.4 mbar O_2, 494 K or 501 K	[35]
336.9	PdO bulk	Polycrystalline Pd foil	1 bar O_2, 1070 K, 1 h	[37]
337.2	PdO	PdO polycrystalline powder	No in situ preparation	[39]
338.0 - 338.2	PdO_2	Polycrystalline Pd foil	RF discharge of 0.2 bar O_2, 2 to 5 min, 300-400 K	[37]
338.3	PdO_2	High purity Pd foil	600 °C, 1 h, O_2	[38]
339.8	Shake-up satellite peak Pd 3$d_{5/2}$	PdO polycrystalline powder	No in situ preparation	[39]
340.3	Pd 3$d_{3/2}$ metal	Pd(111)	Cleaned 1 + O_2 flashing	[34]
342.1	Plasmon loss peak Pd 3$d_{5/2}$	Pd polycrystalline foil	Cleaned 2	[40]
342.5	PdO 3$d_{3/2}$	PdO polycrystalline powder	No in situ preparation	[39]
345.5	Shake-up satellite peak Pd 3$d_{3/2}$	PdO polycrystalline powder	No in situ preparation	[39]

	346.6	Plasmon loss peak Pd 3$d_{3/2}$	Pd polycrystalline foil	Cleaned 2	[40]
Pt 4$p_{3/2}$	519.5	Pt 4$p_{3/2}$ metal	Pt sample	Cleaned 3[3]	[41]
O 1*s*	528.8, 529.6	Surface 2D Pd oxide Pd_5O_4	Polycrystalline Pd foil	RF discharge of 0.2 bar O_2, 2 to 5 min, 300-400 K	[37]
	528.9, 529.5	Surface 2D oxide Pd_5O_4	Pd(111)	$2 \cdot 10^{-3}$ mbar O_2, 571 K and 598 K	[34]
	528.9, 529.6	Surface 2D oxide Pd_5O_4	Pd(111)	0.4 mbar O_2, 494 K or 501 K	[35]
	529.2, 529.9	PdO	Polycrystalline Pd foil	RF discharge of 0.2 bar O_2, 2 to 5 min, 300-400 K	[37]
	529.7	PdO bulk	Pd(111)	0.4 mbar O_2, 494 K or 501 K	[35]
	529.7	O on Pt	Pt(111)	Up to 5 Torr O_2, 300 K-720 K	[31]
	530.3	PdO	Pd(111)	NO_2 at or above 530 K	[42]
	530.3	PtO_2 bulk	Pt(111)	10^{-7}-10^{-8} mbar, O_2, RT	[32]
	530.4	O on Pd	Pd(111)	0.4 mbar O_2, 494 K or 501 K	[35]

[3] Cleaned 3 consists of cleaning in situ using a micro-mill with a rotating diamond edge.

	530.4	O on Pd	Pd(111)	$2 \cdot 10^{-3}$ mbar O_2, 571 K and 598 K	[34]
	530.5	PtO	Pt(111)	10^{-7}-10^{-8} mbar O_2, RT	[32]
	529.8, 530.2, 530.8	O on Pt	Pt(111)	10^{-7}-10^{-8} mbar O_2, RT	[32]
Pd 3*p*$_{3/2}$	532.2	Pd bulk	High purity Pd foil	Cleaned 4[4]	[43]
	532.4	Pd 3*p*$_{3/2}$ metal	Pd polycrystalline foil	Cleaned 2	[40]
	533.8	PdO	High purity Pd foil	10^{-6} bar, NO_2, 150 °C, 30 min	[43]
	534.2	PdO	PdO polycrystalline powder	No in situ preparation	[39]
	537.8	Plasmon loss peak Pd 3*p*$_{3/2}$	Pd polycrystalline foil	Cleaned 2	[40]
	543.7	Shake-up satellite peak Pd 3*p*$_{3/2}$	PdO polycrystalline powder	No in situ preparation	[39]
	560.2	Pd 3*p*$_{1/2}$ metal	Pd polycrystalline foil	Cleaned 2	[40]
	562.1	PdO 3*p*$_{1/2}$	PdO polycrystalline powder	No in situ preparation	[39]

[4] Cleaned 4 consists of ion sputtering, annealing, heating in NO_2, and annealing, in this specific sequence.

	565.6	Plasmon loss peak Pd $3p_{1/2}$	Pd polycrystalline foil	Cleaned 2	[40]
	570.9	Shake-up satellite peak Pd $3p_{1/2}$	PdO polycrystalline powder	No in situ preparation	[39]

1.8.2 Overview of the literary reported species

The overview of the XPS literature is divided into four sections: metallic platinum, oxidation of platinum, metallic palladium, and oxidation of palladium, based on the findings on Pt, Pt-O_x, Pd, and Pd-O_x, respectively. The relevant binding energies and their attributed species are mentioned with the accompanying literature.

1.8.2.1 Metallic platinum

The Pt 4*f* core level is well reported by literature, as it is the main region for platinum. Both Puglia *et al.* [30] and Miller *et al.* [31] agree that the surface and bulk binding energies for Pt $4f_{7/2}$ for a Pt(111) sample are 70.5 eV and 70.9 eV, respectively, for the Pt metal doublet. Both groups used the same cleaning procedure, as Miller *et al.* cites Puglia *et al.* for their cleaning procedure. It consists of first sputtering using Ar^+, followed by high temperature annealing. When the experimental resolution is not sufficient to resolve component peaks with close binding energies, such as between surface and bulk components, or when X-ray photon energy is not particularly surface sensitive, the peak fitting is performed using one broader, common peak located between the surface and bulk component. Parkinson *et al.* [32] reported this combined peak at 71.2 eV for Pt $4f_{7/2}$, which is labelled Pt metal with oxidation state 0. Most of the literature agrees with this value for the Pt metal binding energy. However, it is notably 0.5 eV higher than the peak position

of 70.7 eV, cited as the combined surface and bulk components reported by Puglia *et al.* and Miller *et al.*.

For PtPd alloys, platinum also contributes with Pt 4*d* and Pt 4*p* core level regions in the same spectral windows as the main regions Pd 3*d* and O 1*s*, respectively. These regions can be used to analyse Pt/Pd ratios and metal surface enrichment. Shyu *et al.* [33] found the binding energy for clean platinum Pt $4d_{5/2}$ to be 314.2 eV and $4d_{3/2}$ to be 331.2 eV. The Pt $4p_{3/2}$ binding energy for clean platinum was found by Nyholm *et al.* [41] to be 519.5 eV.

1.8.2.2 Oxidation of platinum

Three types of oxidized platinum species are considered: chemisorbed O, PtO, and PtO_2. In the Pt 4*f* core level region, the platinum oxides PtO and PtO_2 appear at 72.4 and 74.1 eV, respectively, according to Parkinson *et al.* [32]. However, there is a general disagreement in the literature for the binding energy for chemisorbed oxygen on platinum, written as O on Pt in Table 1.1. Miller *et al.* and Parkinson *et al.* reports three different binding energies, giving an expected interval for the binding energy to be 70.9 – 71.2 eV. Parkinson *et al.* found these values when oxidizing with low pressures, in the range 10^{-7} to 10^{-8} mbar, while Miller *et al.* varied their pressures from UHV up to 5 Torr (1 Torr = 1.33 mbar). The contributions for metallic platinum and chemisorbed oxygen on platinum can therefore overlap.

In the O 1*s* core level region, peaks are used to confirm the presence of oxidized platinum or chemisorbed oxygen and quantify the amount of oxygen on the surface. The three platinum-oxygen species mentioned above should also be found in the O 1*s* region. The binding energy for oxygen atoms in PtO and PtO_2 are very close, 530.5 and 530.3 eV respectively, according to Parkinson *et al.*. For oxygen chemisorbed on platinum in O 1*s*, the situation is similar to the Pt 4*f* region, where chemisorbed O is reported in a wide range of binding energies. Miller *et al.* reports O on Pt at 529.7 eV. On the other hand, Parkinson *et al.* reports O on Pt at three different binding energies depending on oxidation conditions: 529.8, 530.2, and 530.8 eV. Parkinson *et al.* found these values when oxidizing with low pressures, in the range of 10^{-7} to 10^{-8} mbar, while Miller *et*

al. varied their pressures from UHV up to 5 Torr. The latter is most relevant to the experiments described in this thesis.

1.8.2.3 Metallic palladium

Pd 3*d* is the most intense core level for palladium. The Pd $3d_{5/2}$ peak for clean metal is expected at 334.9 eV according to Zemlyanov *et al.* [34] and the Pd $3d_{3/2}$ peak at 340.3 eV. In addition, plasmon loss peaks for Pd 3*d* can form on the clean surface. These are expected at 342.1 eV and 346.6 eV for Pd $3d_{5/2}$ and Pd $3d_{3/2}$, respectively [40].

The Pd 3*p* core level region also contributes to the O 1*s* region and can therefore be used to verify Pd 3*d* fitting. Smirnov *et al.* [43] reports Pd $3p_{3/2}$ bulk at 532.2 eV and Militello *et al.* [40] reports the Pd metal peak (definition described in Section 1.8.2.1) at 534.2 eV. For this region plasmon loss peaks are also expected, at binding energy 537.8 eV for Pd $3p_{3/2}$ and 565.6 eV for $3p_{1/2}$ [40].

1.8.2.4 Oxidation of palladium

From the surface phase diagram in Figure 1.4, palladium can form three species upon oxidation. These are chemisorbed oxygen on the surface, a surface oxide, Pd_5O_4, and palladium oxide, PdO. In addition, palladium dioxide, PdO_2, is included for reference. PdO_2 is not expected to form according to the surface phase diagram. Depending on oxidation conditions, Gabasch *et al.* [35] and Kibis *et al.* [37] reports PdO bulk with binding energies given in the interval 336.5 to 336.9 eV. These values were found in mostly higher partial pressures of oxygen and during radio frequency (RF) discharge in oxygen by Kibis *et al.*. RF discharge involves in this case oxidation of noble metals at low temperatures using plasma treatments in an oxygen atmosphere. This is a method opposed to oxidation with molecular oxygen at low temperatures, because then palladium has kinetic limitations for forming oxides [37]. Otto *et al.* [38] reported PdO at 336.5 and 336.7 eV. Chemisorbed oxygen on the palladium surface has the binding energy 335.7 eV, according to Titkov *et al.* [36]. However, most papers do not report the formation of O on Pd, as according to Gabasch *et al.* [35] the ad layer is expected to decompose at 470 K. The surface oxide Pd_5O_4 is

also expected in a broad interval, from 335.5 to 336.4 eV, according to Gabasch *et al.* [35], Zemlyanov *et al.* [34], and Kibis *et al.* [37]. Lastly, PdO_2 is expected at 338.0 to 338.3 eV according to Kibis *et al.* [37] and Otto *et al.* [38]. It is important to remember that according to the surface phase diagram, this oxide is not expected to form. After oxidation, shake-up satellite peaks can form on the surface. According to Militello *et al.* [39], for Pd $3d_{5/2}$ the peak is expected at 339.8 and for $3d_{3/2}$ at 345.5 eV.

As for platinum, every palladium-oxygen species produces a corresponding contribution in the O 1*s* core level. The bulk PdO binding energy is reported by Gabasch *et al.* [35] to be 529.7 eV. Furthermore, PdO is reported in the range 529.2 to 530.3 eV by Kibis *et al.* [37] and Banse *et al.* [32], which too is a wide range. The surface oxide Pd_5O_4 reported by Zemlyanov *et al.* [34], Gabasch *et al.* [35], and Kibis *et al.* [37] has a binding energy ranging between 528.8 and 529.6 eV. Lastly, the binding energy of O 1*s* for PdO_2 is rarely reported, likely because it is too unstable in the experimental conditions. According to Kibis *et al.* [37] the PdO_2 O 1*s* peak is expected beyond 532 – 533 eV, and therefore may coincide with the Pd 3*p* core level peaks.

The oxidized Pd 3*p* core level is reported with some shifts in binding energy. According to Smirnov *et al.* [33] and Militello *et al.* [39] the expected value for PdO Pd $3p_{3/2}$ binding energy is between 533.8 and 534.2 eV. Shake-up satellites can also form for this region. The peaks are expected at 543.7 and 570.9 eV for Pd $3p_{3/2}$ and Pd $3p_{1/2}$, respectively [39].

1.9 Motivation of the thesis

The NAFUMA research group has collaborated with Yara International for decades on various chemistries related to the reaction steps needed to transform ammonia into nitrogen-based fertilizers. In particular, the reaction step where ammonia is oxidized selectively to NO has been given priority. Activities to deepen the fundamental understanding of the PtRh catalytic gauzes with respect to noble metal loss, chemical state of the catalyst at operative process conditions and the role of degree of Rh alloying in the PtRh catalyst have been carried out. Likewise, studies on how to catch Pt lost from the PtRh gauzes during the exothermic oxidation reaction has been a

major topic. The NAFUMA research group have studied Pd-based Pt catchment materials, which currently are in operation in the plants.

The motivation behind this Master of Science project is to develop our understanding on a) the surface chemistry of both the PtRh catalytic ammonia oxidation gauzes, and b) the Pd-based catchment materials with respect to Pt-alloying at the top atomic layers in tandem with oxide formation. Surface sensitive techniques used in the study is the UiO ReactorSTM and the Kratos XPS with the chemistry cell. The UiO ReactorSTM system is used with the preparation stage for sputtering, annealing, metal deposition by electron beam evaporation (EBE), high precision leak valve for introducing O_2 up to 10^{-3} mbar and the high-pressure reactor itself (max 6 bar). The Kratos XPS with the chemistry cell is used to collect XPS spectra of cleaned surfaces (after sputtering and annealing) and after being exposed to synthetic air at a total pressure of 1 bar in the chemistry cell at 500 and 900 °C.

In the first part of the work, we apply a systematic approach to the PtRh system where we prepare well-defined PtRh surfaces by depositing Rh on a Pt(111) single crystal to develop the PtRh synthesis strategy roadmap to include information on the PtRh nanostructuring at higher Rh-coverages. Synthesis parameters explored are Rh deposition coverage and temperature, post annealing steps and oxygen treatments. The obtained results will be put in perspective to the existing PtRh roadmaps reported by our research group [24–27].

The second part of this study is dedicated to developing insight into PtPd nanostructuring on Pd/Pd(111), Pt/Pd(111) and Pd/Pt(111) single crystals by means of STM. Main focus is put on identifying a cleaning procedure on how to clean a Pd(111) crystal, as this is an unexplored territory for the NAFUMA research group.

In the third and last part of the study we aim to investigate XPS spectra obtained on a series of six Pt_xPd_{100-x}, $x = \{0.5, 10, 27, 50, 90, 100\}$ samples after being cleaned at UHV conditions, followed by oxidation at 900 °C in $p(O_2)$ = 0.21 bar in the chemistry cell, and finally after being exposed to $p(O_2)$ = 0.21 bar at 500 °C. In particular, the study focuses on understanding at what conditions Pt and Pd are in their metallic and oxidized forms, as well as the preference of the metal to be located at the top atomic layers on the surface or to go subsurface. To the best of our knowledge, no such systematic studies over a series of PtPd compositions have been carried out before.

2 Theory

An overview of relevant theory on surfaces, STM, and XPS are presented in this chapter in the Sections 2.1 and 2.2, respectively.

2.1 Characteristics and preparation of surfaces

The following sections will focus on how surfaces are described and preparation for use in vacuum experiments, specifically for STM and XPS.

2.1.1 Describing a surface

Surfaces are defined using the same notation as for bulk. Most commonly used are the Miller indices (hkl). They describe the orientation of crystal planes in the periodic structure based on three points of intersection with the crystal axes. The lowest indexed planes are the (100), (110), and (111) planes [44, pp109-112]. When the crystal manufacturer prepares a crystal surface, for instance Pt, the raw metal material is aligned and cut along either of these three planes, therefore exposing for instance the Pt(111) surface, hence the notation.

The periodic structure of atoms for a material is called a crystal structure. Metals are often naturally ordered in these structures. The most common crystal structures are simple cubic (sc), face centered cubic (fcc), hexagonal close packed (hcp), body centered cubic (bcc), and diamond cubic structure [45, pp11-13]. For instance, Pt, Pd, and Rh all have the face centered cubic structure (fcc) [45, p20]. Figure 2.1 depicts the fcc crystal, both with the three crystal orientations mentioned earlier, (100), (111), and (110), and with a cross section of each crystal orientation to illustrate the atoms at the surface with the respective orientation. The (100) surface can be observed to have a square atom arrangement, and similarly (110) a rectangular arrangement and (111) a hexagonal arrangement [46, p3].

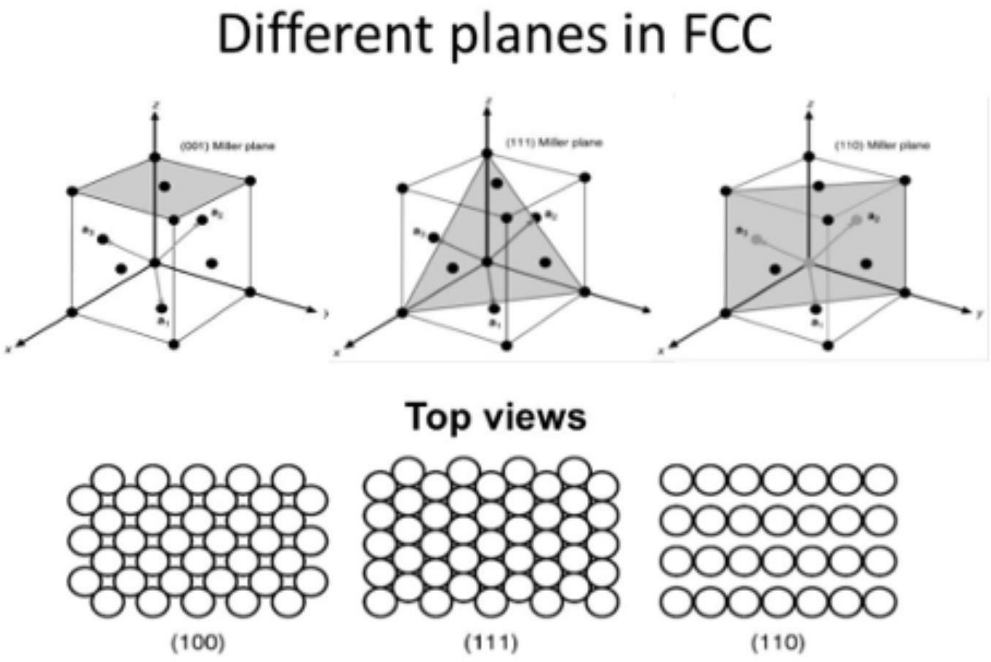

Figure 2.1: Illustration of the (100), (111), and (110) planes for an fcc crystal. Top three images visualize the planes in the crystal, while the bottom three images display the cross section of the crystal orientations. Retrieved from [47].

The crystal structure of a surface can either result from the native structure of the substrate or the atoms deposited on the substrate. This results in either homo- or heteroepitaxial materials. *Homoepitaxy* is growth of layers of the same material as the substrate, for instance Pd/Pd(111). *Heteroepitaxy* is the opposite; the new layers are made of a different material than the substrate, for instance Rh/Pt(111) [48]. The crystal structure of the surface is then given by which epitaxial growth the new layers have. Despite small lattice mismatch caused by heteroepitaxial growth, the material is likely to strain, which later causes defects on the surface [49]. For instance, Pd/Pt(111) has a small lattice mismatch (<1%), which may be described as resulting from homoepitaxial growth, but the surface is relatively characterized by numerous defects, shown in Sections 1.7.1 and 1.7.2 [28,29].

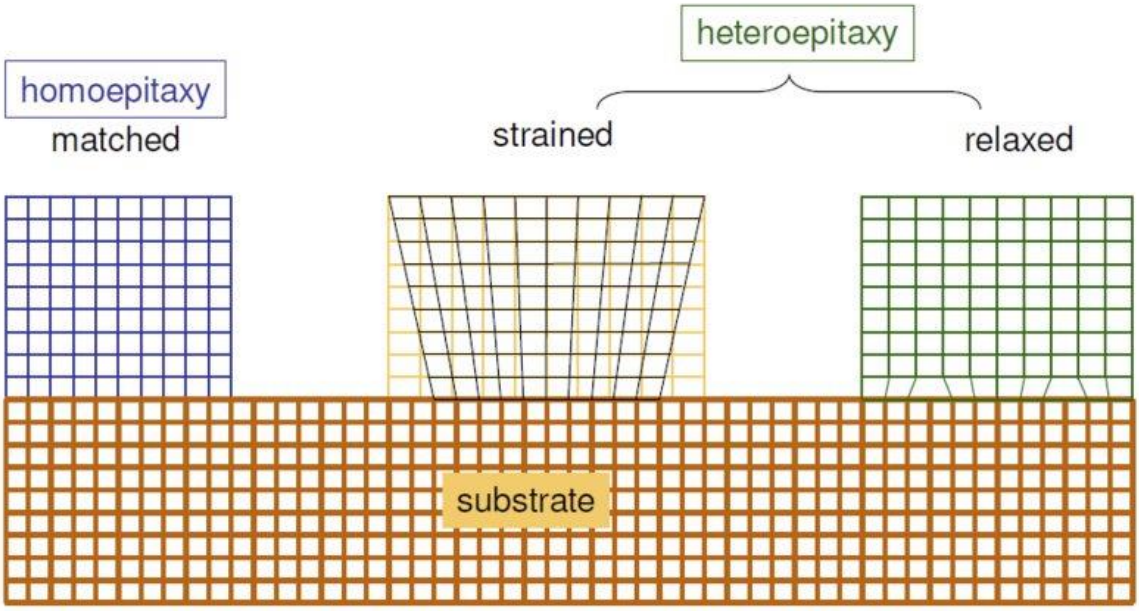

Figure 2.2: Illustration of homo- and heteroepitaxial growth on a substrate. Heteroepitaxial growth can either lead to a strained or relaxed lattice structure at the surface. The lattice is relaxed due to dislocations and defects at the interface. Retrieved from [50].

2.1.2 Cleaning a surface

In order to obtain well-defined pristine surfaces, the metal crystals must firstly be cleaned to remove bulk and surface impurities and contaminations. Metal surfaces prepared for STM and XPS are often cleaned with similar treatments. After a reliable cleaning procedure is established, it can be used after each preparation treatment to clean the surface. A typical cleaning procedure consists of cycles of ion bombardment, also called ion sputtering, and annealing. *Ion sputtering* is the process of bombardment of ions with typical energy of 0.5 – 2 keV onto the surface to remove contaminations, often C, S, and O based. It is important to use low-energy ions to make sure the surface is not excessively and irreversibly roughened in the process. Another important aspect is to use a non-reactive element in order to not alter the surface chemistry, hence Ar^+ is typically used [51,52]. After the ion sputtering, annealing is performed. *Annealing* is a heat treatment of the surface at high temperatures to remove adsorbates and flatten the roughness of the surface caused by ion sputtering. In vacuum, annealing is often accomplished with different modes: resistive

heating, laser irradiation, or electron beam heating. When annealing it is important to choose a temperature which is high enough to have an annealing effect, but does not alter the surface composition, such as a phase transition [52]. For instance, in this experimental work, the Pt(111) single crystal was annealed at roughly 1100 K ≈ 830 °C. According to the binary phase diagram for Pt-Pd in Figure 1.3, Pt melts at around 1769 °C. Annealing at 830 °C is thus a good annealing temperature. Often, *oxidation* is performed simultaneously as annealing. When the surface is subjected to oxidative environments at higher temperatures, the contaminations at the surface will oxidize, and the subsequent cycle will remove or decompose the oxides [52]. After numerous cycles, the cleanliness is determined, for instance by Low-Energy Electron Diffraction (LEED).

2.1.3 Deposition of atoms

Further preparation and functionalization of the surface is accomplished by vacuum deposition or evaporation of atoms and molecules. This is commonly done through an Electron Beam Evaporator (EBE). An electron beam with a voltage of several kV is directed onto the source rod or crucible, heating up the source material to the evaporation temperature, which produces a flux of the material accelerated towards the sample [52]. Because of the high temperature produced inside the EBE body, a water-cooling system has to be implemented and used during the evaporation.

2.1.4 Post annealing

Post annealing is a heat treatment performed after the preparation of the surface. Annealing is described in Section 2.1.2. Post annealing is performed, for instance, to desorb adsorbates, induce surface restructuring, promote alloying of the surface constituents, change the band gap of the material, alter the particle grain sizes, and other alterations to the chemical and physical properties of the surface [53]. In this thesis work, the main purpose of post annealing is to induce mixing and alloying of the bimetallic surfaces.

2.1.5 Oxidation

Lastly, some surfaces are oxidized to investigate the changes in the surface composition. Oxidation of surfaces are for instance highly relevant for catalysis, semiconductor devices, and protective or functional oxide films [54]. Lower pressure oxidation ($\leq 10^{-3}$ mbar) can be performed in regular preparation chambers, such as in the STM chamber, however, higher pressures, such as 1 bar, must be performed in designated chemistry cells. Both are further described in Sections 2.2.1.2 and 2.2.1.3, respectively.

2.2 Characterization methods

The two characterization methods used in this thesis are STM and XPS. In the sections below, their operating principle and instrumentation will be explained. Additionally, the ReactorSTM is described.

2.2.1 STM

The *Scanning Tunneling Microscope* (STM) is one of the several most important characterization methods in the field of surface science. Invented in 1982 by Gerd Binnig and Heinrich Rohrer, it earned them the Noble Prize in Physics in 1986 [55, p172,56, p3]. The instrument is revolutionary for its ability to scan surfaces at both ultra-high vacuum (UHV) conditions as well as at high pressure conditions, bridging the so-called pressure gap. Additionally, it can also function at extremely low (mK) as well as high temperatures (>1000 K) [56, p3] . The combination of high pressure and elevated temperatures allows for study of catalysts at industrially relevant conditions.

2.2.1.1 Operating principle

The STM is a Scanning Probe Microscope (SPM). SPMs uses a tip or a stylus to probe a surface. By moving the tip across the surface, a 2D image of the topographic features of the surface are produced. There are two types of SPMs most commonly used: the STM and the Atomic Force Microscope (AFM). The STM employs tunneling of electrons between the surface and the tip to map the density of states of the surface atoms. The AFM uses a cantilever to probe the surface directly by using near-field forces (van der Waals, electrostatic, and chemical) between the tip and the surface [44, p165]. The tip is mounted on a cantilever, which scans across the features of the surface and thus creating an image. Both these methods have a possible lateral resolution of a few nanometres. The main difference between the instruments is that the STM can only be applied on conducting surfaces, whereas the AFM can be applied to both conductive and non-conductive samples.

Focusing on the STM, tunneling is a quantum mechanical phenomenon involving minute particles travelling across an energy barrier, which according to classical physics should be impassable. The phenomenon is possible because of the wave nature of the small particles [57]. Electrons are a typical example of tunneling particles. In an STM, quantum tunneling occurs through the energy barrier in the form of a nanoscopic vacuum gap between the tip and the surface. When the gap between the tip and the conductive sample is significantly less than 1 nm, an unassisted tunneling can occur. By applying an external bias voltage between the tip and the surface, the electrons are able to tunnel across a larger gap. The produced current is called the tunneling current, and is given by the relation in Equation 2.1 below [56, p4].

$$I(d) \propto eVe^{-\kappa d} \qquad 2.1$$

Because the electrons are only able to tunnel if the gap between the tip and the surface is very narrow, around a nanometre, the instrument is exponentially sensitive to the barrier height [55, pp216-220]. Since the tunneling current and tip-sample distance are correlated through Equation 2.1, the surface 2D topographic map can be determined with hight presented using intensity scale.

The obtained raw image shows a grayscale image with bright areas corresponding to high tunneling probability, and dark areas showing low electron density. To better facilitate the contrast perception, a colour pallet is often applied to the raw images, typically orange. An example of STM images with the orange colour pallet is depicted in Figure 2.3.

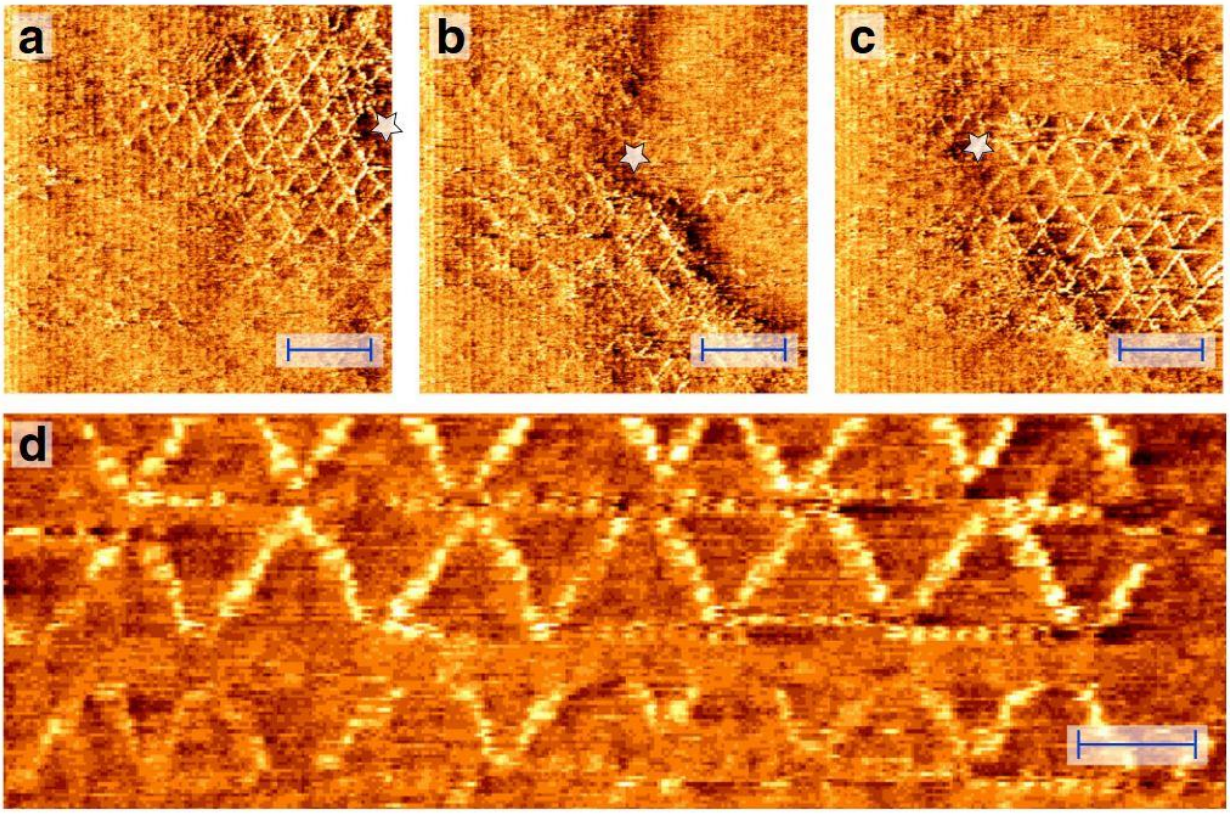

Figure 2.3: STM images of Pt(111) while exposing the surface to 1 bar of O_2 at 529 K. The observed triangles form a superstructure called the spoked-wheel structure. Scale bars represent 4 nm for **a)** – **c)** and 2 nm for **d)**. Retrieved from [58].

There are four operating modes of an STM: constant current mode, constant height mode, spectroscopic mode, and manipulation mode. *Constant current mode* is the most used scanning mode. Here the current and the voltage is kept constant, while the height is measured during scanning. The image created is contour of the local density of states (LDOS), but at small scales on homogeneous samples, this is nearly identical to the topography of the surface [44, p168,56, p5]. A second mode is *constant height mode*, where the height is kept constant and the tunneling

current is varied. This mode can be performed at a higher scan speed because there is no need for continuous adjustment of the tip-sample distance. However, it can only be used for relatively flat and homogeneous surfaces, as the risk for the tip to crash is significantly higher. A third mode is *spectroscopic mode*. This mode is used to record the tunneling current as a function of applied bias or height, and gives information on the surface properties, both electronical and chemical information [44, p168,56, p5]. The last mode is the *manipulation mode*. Relatively often, the tip picks up atoms from the surface. In a regular scan this leads to interference and noise in the images, and the tip needs to be pulsed to return to better quality scans. However, as Binnig and Rohrer realised, this creates an opportunity where it is possible to relocate adatoms by varying the height and voltage. To accommodate for diffusion of the atoms, the sample needs to be kept at very low temperatures, only a few kelvins. This technique has been used to make the "smallest stop motion film ever made" called "A Boy And His Atom", created by IBM [44, p168,55, p174]. The vast difference between the four modes exemplifies how the STM is very versatile within surface science.

2.2.1.2 Instrumentation of an STM at UHV conditions

The STM instrumentation will be described using the STM installed at the University of Oslo (UiO). Figure 2.4 below shows the ReactorSTM used in this MSc thesis. In the case of ultra-high vacuum (UHV) instrument, the chambers are separated by gate valves to ensure the retainment of vacuum. The chambers in an STM are the STM chamber, the load lock, the preparation chamber, and possibly the XPS chamber [56, p9]. The samples are inserted into the STM through the load lock chamber. The load lock is normally kept at pressures around 10^{-8} mbar by a turbomolecular pump and scroll backing pumps, in order to not damage the equipment, such as the ion source and the EBE [56, p8]. After inserting the sample, the load lock is pumped down to ultra-high vacuum (UHV) around 10^{-7} – 10^{-8} mbar in order to transfer the sample to other chambers, because the chamber pressures need to be comparable. The pressure difference cannot be larger than two orders of magnitude.

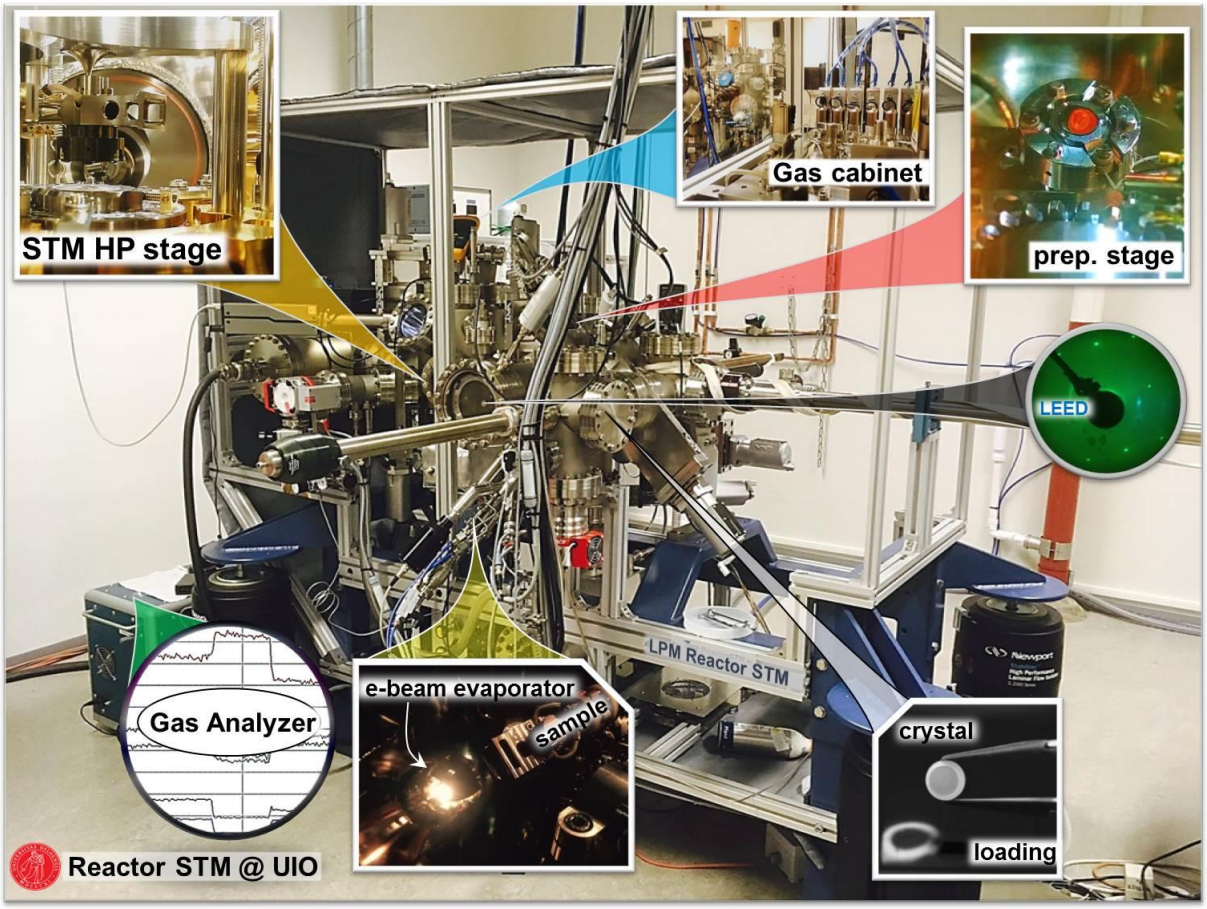

Figure 2.4: Image of the ReactorSTM at the University of Oslo, used in this master thesis. Retrieved from [59].

When the pressures are compatible, the sample can be transferred via the transfer dock to the sample parking or the other parts of the instrument using a rack-and-pinion transfer rod. The transfer arms are visibly sticking out of the instrument and are capable of moving and rotating the samples across the instrument [56, p9]. The parking is where samples which are not in use are kept. Moving the samples in and out of UHV can take one to two hours.

The next chamber is the preparation chamber. This chamber is equipped with multiple treatment and characterization instruments: an ion sputtering source, heating station, *an electron beam evaporator* (EBE), high precision gas leak valves, and characterization instruments such as *Low-Energy Electron Diffraction* (LEED) [56, p9]. Firstly, the samples are cleaned through repetitive cycles consisting of ion sputtering and annealing. Afterwards, the sample is prepared and modified by using the evaporator to deposit metals. Furthermore, the samples can be post annealed, oxidized

through the oxygen gas line, or reduced by dosing reducing gases. The reducing gases are currently not used in the ReactorSTM. To ensure high purity in the chamber, a combination of turbomolecular pump, ion pump, and titanium sublimation pump is often used, resulting in pressures of 10^{-9} to 10^{-10} mbar. Detrimentally, pressures of 10^{-7} mbar and higher can contaminate the ion pump, thus it has to be isolated during ion sputtering (10^{-5} mbar), oxidation (10^{-7} – 10^{-3} mbar), and other treatments involving higher pressures. Similarly, hot cathode pressure gauges need to be protected from oxygen or air pressures of 10^{-6} mbar and higher, and therefore should be switched off during oxidation. In addition to a contact thermocouple for temperature readout of the sample surface, an infrared camera can be used to read out the temperature of samples with known emissivity.

After preparation, the sample can be characterized in the STM chamber. The sample is scanned in a raster pattern, which implies the tip moving back and forth across the sample (left to right, and reversely, right to left), giving two different images depending on the direction the tip moves. The tip is typically made of a PtIr alloy or a W wire [56, p3]. In the STM station the sample can be heated, both for annealing, post annealing, and for keeping the desired temperature during STM scanning. For optimal pressure, this chamber is also connected to a turbomolecular pump and an ion pump, and the pressure is equal or better than in the preparation chamber. A gas system and a *Quadrupole Mass Spectrometer* (QMS) are connected to the STM chamber and used during experiments with high pressure conditions in a small reactor cell inside the STM chamber [56, p6]. This version of an STM is referred to as ReactorSTM. The STM at UiO is a ReactorSTM, and capable of operating in UHV and high pressures of up to 6 bar. This will be described further in Section 2.2.1.3.

The tunneling current relation given in Equation 2.1 points out an important component of an STM. The current is very sensitive to the distance between the tip and the sample. The nanoscopic gap can easily be perturbed by external mechanical vibrations, affecting the scanning. Therefore, vibration isolation is used for the STM both internally and externally. The internal isolation is done by suspending the scanner-sample assembly on springs and by Eddy current damping, which effectively decouples the STM stage from the whole chamber. Externally, the entire frame of the instrument is resting on pressurized air legs that additionally decouple the instrument body from the rest of the world [44, p166,56, p12].

In addition to microscopy instruments, spectroscopy instruments can be implemented in a dedicated chamber. This is commonly an XPS and/or an *Auger Electron Spectroscopy* (AES) [56, p6]. By directly having access to an XPS in the STM, samples can give both topographical and chemical information in the same instrument without exposing the sample to air. Unfortunately, the instrument used in this thesis did not feature an XPS at the time of writing.

2.2.1.3 The ReactorSTM – scanning at high pressures

When a measurement technique does not operate in realistic conditions, for instance in UHV instead of high pressures employed in industrial processes, measurement gaps such as the *temperature gap* or the *pressure gap* arise. The presence of such gaps in experiments leads to results which are not representative of real (ambient) conditions. The high pressure ReactorSTM bridged both the pressure and temperature gap in surface science, by allowing topographical information of surfaces at high pressures and elevated temperatures to be obtained. Furthermore, this proved to be valuable in industrial science at realistic reaction conditions [56, p2].

High pressure conditions are reached inside a small reactor cell, about 0.5 mL. This cell is composed of the crystal surface, a tip ceramic bed, and a seal. The polymer seal is made of a chemically resistant material, for instance Kalrez or Fluorez, which is placed around the tip mount. When the sample is brought closer to the tip, a small flow reactor volume will be created, which can withstand the pressure difference of up to 12 orders of magnitude, from elevated pressures in the cell to the UHV elsewhere in the STM chamber [56, pp8-12].

The highest possible pressure that can be reached in a STM today is approximately 6 bar, and is defined not by the seal, but by the gas system. The filament built into the sample holder allows for increasing the surface temperature to around 1000 °C, however, in a reactor cell the polymer seal material can only withstand temperatures below 300 °C. Two gas lines, an inlet and an outlet, are connected to the reactor cell and supplies gas through the gas system [56, p8]. Typical gases that can be sent in and mixed are, but not limited to, hydrogen gas (H_2), oxygen gas (O_2), ammonia (NH_3), nitrogen monoxide (NO), and carbon monoxide (CO). The Quadruple Mass Spectrometer (QMS) is used for analysis of the effluent coming from the outlet line [56, pp7-12]. Examples of

heterogeneous catalytic reactions that have been studied using a ReactorSTM are ammonia oxidation, hydrodesulfurization, CO oxidation, and Fischer-Tropsch synthesis of hydrocarbons [56].

2.2.2 XPS

The *X-ray Photoelectron Spectrometer* (XPS) is a surface sensitive technique for elemental analysis of a solid [44, p221]. XPS is often used to compliment STM topography images, giving both an image of the surface and information of what atoms or species that make up the surface. Ideally, the surface analysis instrument would be equipped with both an STM and an XPS to facilitate a comprehensive study of a surface.

2.2.2.1 Operating principle

To acquire the elemental information in an XPS, X-rays are shot at a sample, emitting electrons from the electron shells of the constituent atoms. The electrons are emitted if the atom absorbing the energy from the incoming X-rays have enough energy to overcome an energy barrier called work function, Φ. The work function describes the minimum energy an electron needs to be ejected from a solid surface and is dependent on both the surface material and the spectrometer. The electrons emitted from the atom are called photoelectrons. The work function relates the electron to the surface, but not directly to the constituent atoms. This is done through calculating the binding energy (BE) of the photoelectrons (E_B), shown in Equation 2.2:

$$E_B = h\nu - E_K - \Phi \qquad 2.2$$

The binding energy of the photoelectrons (E_B) describes the minimum energy an electron needs to be ejected from an atom or ion. Therefore, the binding energy will directly give information on which atom, and shell, an electron is emitted from, thus giving elemental information on the

surface. Additionally, the binding energy is also dependent on the chemical environment, thus giving information on the oxidation state of the atoms. This allows differentiation between the different species of an element, for instance pure metal or oxide, which is highly relevant for catalytic reactions. $h\nu$ is the energy of the X-ray and E_K is the kinetic energy of the atom after it has been emitted. In an XPS experiment the kinetic energy, E_K, is found and the number of photoelectrons is counted as a function of E_K. Through Equation 2.2, E_K is converted to E_B, and the number of electrons, i.e., intensity, is plotted as a function of the binding energy, as both $h\nu$ and Φ are known [44, pp221-222,56, pp31-32]

XPS is surface sensitive because the photoelectrons will have such low kinetic energy (20 to 2000 eV), that they can only escape the outermost atom layers [44, p221].

The surface information is divided into two different types: qualitative and quantitative. The qualitative information is the identity of the atoms or their oxidation state, partial charge of the atom, which are commonly derived from the chemical shifts of the peaks. The quantitative information is the amount of an atom or atom species [44, pp235-249].

2.2.2.2 Instrumentation

An XPS is made up of two main components: an X-ray source and an electron energy analyser, as well as a monochromator, sample stage, and a detector [44, pp225-227]. Figure 2.5 below showcases the XPS instrument used in this thesis, named Kratos Axis Ultra. It is located at Forskningsparken, UiO. The figure additionally illustrates the two main components of a XPS instrument, as well as the location of the sample, the monochromator, and the detector. The X-rays are produced in the X-ray source, pass through the monochromator, and onto the sample. The photoelectrons are emitted from the surface and pass through the analyser to arrive at the detector.

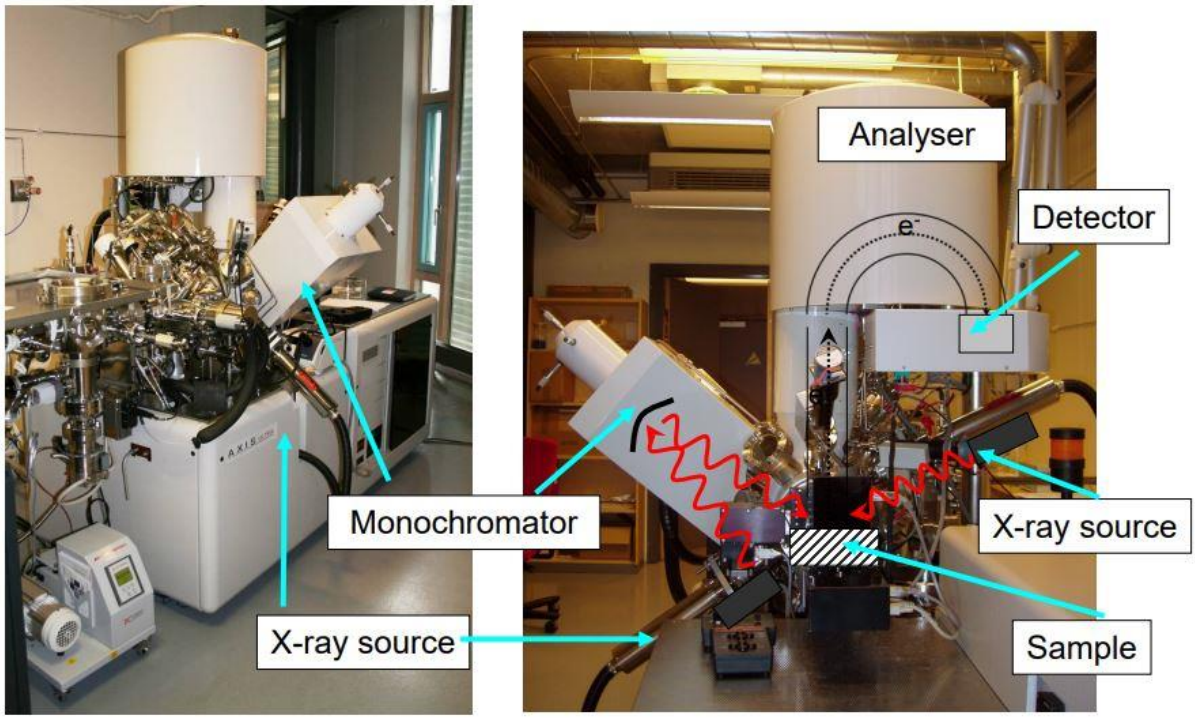

Figure 2.5: Image of the Kratos Axis Ultra used for XPS measurements in this thesis. Retrieved from [60].

The X-ray source produces X-rays excited by high-energy electrons hitting a metal anode, typically Al or Mg, which then releases characteristic X-rays attributed to the metal anode. The X-rays can be both monochromatic and non-monochromatic, whereas non-monochromatic X-rays have a wide range of energy and monochromatic only has X-rays with one specific energy value. By excluding all other X-rays than those with one specific energy, thereby having a monochromatic X-ray source, it is possible to achieve an increased energy resolution with a narrow line width, which describes the range of energy of the X-ray beams. The line width for a XPS should be lower than 1.0 eV for good resolution [44, pp227-228].

As for a STM, clean and well defined surfaces produce more meaningful and reproducible results. Therefore, an XPS is often also equipped with an ion source used to sputter the surface. See Section 2.1.2 or 2.2.1.2 for further explanation of the instrumentation and use of an ion source for sputtering [44, p229].

The state of the art energy analyser most XPS' use at the time of writing is a concentric hemispherical analyser (CHA). This analyser consists of two concentric hemispheres with different potentials, one positive and one negative, which bend the trajectories of the photoelectrons based on their kinetic energies, E_K. The position of the electrons at the detector will therefore be an indicator to their kinetic energy. The potentials create a median equipotential with the value V_0. The electrons are focused by an electrostatic lens to the small slit opening/aperture to the analyser. Furthermore, to increase the energy resolution, some of the unwanted electrons are also reduced in energy, i.e., retarded, by the lens. This is called electrostatic retarding. The electrons are retarded because they need to have a specific kinetic energy equal to the so-called pass energy, $E_0 = eV_0$, for the photoelectrons to pass through the analyser to the detector. By varying the potentials of the concentric hemispheres, the equipotential is varied, and thus the pass energy, allowing different electrons to pass than previously [44, pp229-230][56, pp31-32]

The photoelectrons are likely to scatter with the gas molecules because of their low energy, and therefore to ensure minimal background noise arising from inelastically scattered electrons, the XPS chamber is kept in ultra-high vacuum (UHV) ($<10^{-8}$ mbar). Additionally, the sample is less likely to be contaminated. The vacuum is achieved by using ion pumps and turbomolecular pumps, in a similar fashion as for the STM, see Section 2.2.1.2. The chamber can be lined with a material that promotes magnetic shielding, as the photoelectrons can easily be affected by magnetic fields, including the earth's magnetic field [44, pp225-227].

2.2.2.3 Data treatment and interpretation

A XPS spectrum is written as photoelectron intensity as a function of binding energy, E_B. There are three main types of peaks: core level peaks, valance level peaks, and Auger peaks. *Core level peaks* are emissions from inner shells of an atom. They are often more strongly bound than valance electrons. Examples of core levels are Pt *4f* and Pd *3d*. *Valance level peaks* are emissions from the outer, emptier shells resulting in low binding energies, 0 – 20 eV, and are more useful in electronic structure studies. *Auger peaks* originate from emission of Auger electrons, which are electrons emitted because an inner-shell electron was excited and replaced with an outer-shell electron, resulting in an energy difference between the two electrons that can cause emission of a third

electron, namely the Auger electron. Auger peaks are useful for thermal analysis, but may obscure the XPS spectra [44, pp230-231].

In addition, there are three types of other, smaller peaks that give some or no information: Shake up satellite peaks, plasmon loss peaks, and multiplet splitting. *Shake up satellite peaks* originate from an interaction between a photoelectron and a valence electron, where the photoelectron excites the valence electron to a higher energy level, and the photoelectron therefore loses some kinetic energy that results in a peak associated with the core level peak of the photoelectron. These peaks are relevant from chemical analysis. *Plasmon loss peaks*, however, give no significant information. The plasmon loss peak originates from interactions between photoelectrons and conduction electrons. The photoelectrons cause vibrations in the conductive electrons through excitations, which lowers the kinetic energy of the photoelectrons. Because they are associated with conductive electrons, the plasmon loss peaks appear in spectra of clean metal surfaces. Lastly, *multiplet splitting* occur because the material has unpaired electrons in the valance level. A core level peak will then appear split in the spectrum. These peaks are also useful for chemical analysis [44, pp231-232].

The background of a XPS spectrum resembles steps, that increase with higher binding energy. The steps originate from inelastic scattering of the photoelectrons, and with increasing energy the photoelectrons are more likely to scatter, resulting in higher intensity. When fitting the XPS spectrum, the background is usually removed by fitting the background itself and subtracting it from the relevant peaks. If the X-ray source is non-monochromatic, the photoelectron emissions will cause background in the low-energy region of the spectrum [44, p231].

3 Experimental

The following sections are divided into experimental information on 1) the STM experiments, and 2) the XPS experiments. Section 3.1 will address the STM and single crystal descriptions, sample preparation, and how the STM measurements were performed. Section 3.2 will similarly address the sample preparations, and finally, how the XPS measurements were performed.

3.1 STM characterization of bimetallic Pt(111) and Pd(111) surfaces

The experimental information about the performed STM characterizations on Pt(111) and Pd(111) surfaces are divided into three subsections: 1) general information about the single crystals and STM instrumentation, 2) overview of the cleaning procedures and treatment procedures of the single crystal and the employed parameters, additionally summarized in two tables, and 3) information about the STM chamber and scanning equipment used when scanning.

3.1.1 Single crystal and instrument description

Three different single crystals have been used for STM experiments in this thesis: two different Pt(111) single crystals and one Pd(111) single crystal. The crystals were purchased from Surface Preparation Laboratory (SPL). The shape used in the ReactorSTM sample holder is a hat type, with a sample diameter of 10 mm at the base, 8 mm at the top, and a thickness of 2 mm. The purity is 99.999 % (5 N) for all crystals.

The sample treatment consisted of cleaning cycles, heat treatment, meal deposition, and oxidation using O_2. The equipment used are:

- SPECS IQE 11/35 ion source for sputtering, see Table 3.1 for parameters.

- Prevac HEAT-PS3 power supply for heating the crystals, used in both manual mode and automatic mode. For lower temperatures, only resistive heating mode was used, and for higher, both resistive and e-beam heating.

- A combination of K-type thermocouple readout and Micro-Epsilon TIM 1M infra-red (IR) thermal imaging camera readout was used for reproducible heating monitoring. The emissivity value used for the IR camera is 0.8 for both Pt and Pd.

- SPECS four pocket electron beam evaporator EBE-4 for evaporation of Pt, Rh, and Pd. The acceleration high voltage used was 1.5 kV. The evaporator was used in flux control mode, with typical metal evaporation flux of 12 nA for Pt, 8 nA for Rh, and 6 or 9 nA for Pd, see Table 3.2 for further details. Pt, Pd, and Rh were evaporated from 25×2 mm rods purchased from Goodfellow (99.95% purity).

- The gases connected to the high precision metal leak valves are Ar (5.0, Westfalen) for sputtering and O_2 (5.0, Westfalen) for oxidation.

3.1.2 Sample preparation

The samples were only prepared in the ReactorSTM preparation chamber, see details about the ReactorSTM in Section 2.2.1. The chamber has a base pressure of around $1 \cdot 10^{-9}$ mbar, and is equipped with the sputtering unit, the annealing unit, an EBE, leak valves, for instance for oxidation, as described in Section 2.2.1.2. Table 3.1 below lists the various cleaning cycles performed on the three single crystals.

The Pd(111) sample was new and therefore needed more than 30 cleaning cycles before first characterization attempt. Additionally, a Pd sample has not been used at the ReactorSTM lab previously, thus the reliable cleaning procedure needed to be found through experimenting. The cleaning cycles performed in this thesis are based on numerous references [61–68]. In total, 5 different cleaning procedures have been used. The two most used, highlighted in blue in the table below, are procedures 2 and 4.

The Pt(111) crystals were subjected to 10 different cleaning cycles, summarized in Table 3.1. The cleaning procedure for Pt(111) single crystals is well known both in literature and has previously yielded reproducible results on the ReactorSTM lab of the University of Oslo [24,26,27]. Cleaning procedure 2 was followed in most of the experiments. Notably, slightly more aggressive cleaning, longer sputtering duration and ion energy, higher annealing temperature were performed after the sample was serviced or after longer depositions of ad metals, for instance cleaning procedure 5 and 10 performed on Pt in Table 3.1. After annealing, the samples were sometimes cooled in an O_2 back pressure around 10^{-7} mbar to oxidize possible carbon contaminations over.

To avoid extensive deposition of sputtered material onto the sample holder ceramics, the e-beam high voltage bias was decreased from 1000 to 850 V at the beginning of 2022. Consequently, this value was used for all three samples.

Table 3.1: Overview of the conditions used in the cleaning procedures performed on the three single crystals: one Pd(111) and two Pt(111). The rows highlighted in blue are the cleaning procedures most frequently performed. The "Sample" column corresponds to the single crystal the cleaning procedures were performed on, either Pd(111) or Pt(111).

	Ion sputtering (Ar^+)						**Annealing**			
Sample	Time [min]	Temp [K]	Ar Pressure [mbar]	Beam Energy [eV]	Sample current [µA]	Ion emission current [mA]	Time [min]	Temp. acc. to TC [K]	Pressure [mbar]	E-beam bias voltage [V]
Pd 1	10	<500	$2\cdot10^{-5}$	750	7	10	8	1000	$<1\cdot10^{-8}$	1000
Pd 2	10	<500	$2\cdot10^{-5}$	750	7	10	8	1100	$<1\cdot10^{-8}$	1000
Pd 3	10	<500	$2\cdot10^{-5}$	750	7	10	20-30	1100	$<1\cdot10^{-8}$	1000

Pd 4	10	<500	$2 \cdot 10^{-5}$	750	7	10	8	1100	$<1 \cdot 10^{-8}$	850
Pd 5	10	<500	$1.5 \cdot 10^{-5}$	1000	7	10	8	1150	$<1 \cdot 10^{-8}$	850
Pt 1	10	<500	$1.5 \cdot 10^{-5}$	1000	6	10	10	1100	$<1 \cdot 10^{-8}$	1000
Pt 2	15	<500	$1.2 \cdot 10^{-5}$	1000	6	10	10	1100	$<1 \cdot 10^{-8}$	850
Pt 3	20	<500	$1.5 \cdot 10^{-5}$	1000	6-7	10	10	1100	$<1 \cdot 10^{-8}$	850
Pt 4	15	<500	$1.5 \cdot 10^{-5}$	1000	7	10	15	1100	$<1 \cdot 10^{-8}$	850
Pt 5	25	<500	$1.5 \cdot 10^{-5}$	1500	7-8	10	10	1100	$<1 \cdot 10^{-8}$	850
Pt 6	15	<500	$1.2 \cdot 10^{-5}$	1500	6	10	10	1100	$<1 \cdot 10^{-8}$	850
Pt 7	15	<500	$1.2 \cdot 10^{-5}$	1500	6	10	10	1100	$<1 \cdot 10^{-8}$	850
Pt 8	20	<500	$1.5 \cdot 10^{-5}$	1250	7-8	10	8	1100	$<1 \cdot 10^{-8}$	850
Pt 9	20	<500	$1.5 \cdot 10^{-5}$	1500	7	10	6	1100	$<1 \cdot 10^{-8}$	850
Pt 10	20	<500	$1.5 \cdot 10^{-5}$	1500	7	10	10	1100	$<1 \cdot 10^{-8}$	850

Table 3.2 below lists the metal evaporation conditions, as prepared (AP), post annealing (PA), and oxidation (OX), used for preparing the Rh/Pt(111), Pd/Pd(111), Pt/Pd(111), and Pd/Pt(111) surfaces imaged and reported in Sections 4.1 and 4.2, respectively. Three of the Pd/Pt(111) surfaces were not post annealed. The surfaces were prepared with an electron beam evaporator (EBE) for deposition.

Table 3.2: Overview of metal deposition, post annealing, and oxidation treatments for the Pd/Pd(111), Pt/Pd(111), Pd/Pt(111), and Rh/Pt(111) surfaces. The abbreviations are; as prepared (AP), post annealing (PA), and oxidation (OX). The flux is shortened from nA/min to nA.

Sample	AP flux [nA]	AP time [min]	AP temp [K]	PA time [min]	PA temp [K]	OX time [min]	OX temp [K]	OX pressure [mbar]
Pd/Pd(111)	5	10	460	-	-	-	-	-
Pt/Pd(111)	12	5	410	-	-	-	-	-
Pt/Pd(111)	12	15	450	-	-	-	-	-
Pt/Pd(111)	12	15	475	-	-	-	-	-
Pd/Pt(111)	6	6	500	30	700	-	-	-
Pd/Pt(111)	6	6	400	30	700	-	-	-
Pd/Pt(111)[5]	6	6	450	-	-	30	700	10^{-7}
Pd/Pt(111)	9	15	400	-	-	30	700	10^{-5}
Pd/Pt(111)[6]	9	60	400	-	-	30	700	10^{-5}
Rh/Pt(111)	8	24	380	20	600	20	600	10^{-3}
Rh/Pt(111)	8	24	450	20	600	20	600	10^{-3}

[5] Scanned STM twice, two days apart. After the second STM scan, the surface was oxidized.

[6] Images of oxidized surfaces were bad, both by dirt and by interference and noise.

Rh/Pt(111)	8	24	350	20	700	-	-	-
Rh/Pt(111)	8	24	350	20	700	-	-	-
Rh/Pt(111)	8	24	350	20	700	20	600	10^{-3}
Rh/Pt(111)	8	32	350	20	600	20	600	10^{-3}

3.1.3 STM measurements

The STM used in this thesis is the ReactorSTM at the University of Oslo. For information about an STM, see Section 2.2.1. The prepared surfaces, see Table 3.2, were scanned at room temperature (RT) and at the base pressure of the STM chamber of approximately $5 \cdot 10^{-9}$ mbar. The turbomolecular pumps (HiPace80) connected to the load lock and the STM chamber interfere with scanning and were therefore turned off during scanning. During scanning, both ion pumps (Starcell 150 and 300) and the turbomolecular pump (HiPace300), connected to the preparation chamber, were pumping with the gate valve between the chambers open to maintain a good base pressure. Additionally, to facilitate the cleanest UHV environment during scanning, the preparation and STM chambers were normally connected, however, closed when ion sputtering and oxidizing, as mentioned in Section 2.2.1.2.

The tips used for scanning were cut manually from a 0.25 mm $Pt_{80}Ir_{20}$ alloy wire, supplied by Goodfellow. For data recording, the CAMERA 4.3 software package developed at the University of Leiden was used. All images were taken in constant current mode with bias ranging from -0.5 to -1 V and tunneling current of 0.1 – 0.3 nA.

The resulting STM images were processed in the SPM scan image software WSxM [69].

3.2 XPS characterization of PtPd bulk alloys

This section will cover the experimental information on the PtPd bulk alloys used for the XPS characterization, the treatments the samples were subjected to, as well as the instrumental and measurement information used when analysing.

3.2.1 Sample composition and treatment prior to XPS analysis

Six PtPd samples (Pt_xPd_{100-x}, $x = \{0.5, 10, 27, 50, 90, 100\}$), which are shortened to Pt_x or Pt*x*, were provided for the XPS measurements. The five alloys were the most important samples and Pt100 was used as a reference sample. The samples, and accompanying producer, are as followed:

- 0.5 at% Pt - produced by SPL
- 10 at% Pt - produced by MaTeck
- 27 at% Pt - producer unknown
- 50 at% Pt - produced by MaTeck
- 90 at% Pt - produced by MaTeck
- 100 at% Pt - polycrystalline foil, SINTEF

The six Pt_xPd_{100-x}, $x = \{0.5, 10, 27, 50, 90, 100\}$ samples are drawn in the bimetallic PtPd phase diagram, taken from Figure 1.3, to visualize the sample compositions, see Figure 3.1 below. The coloured lines represent the six compositions.

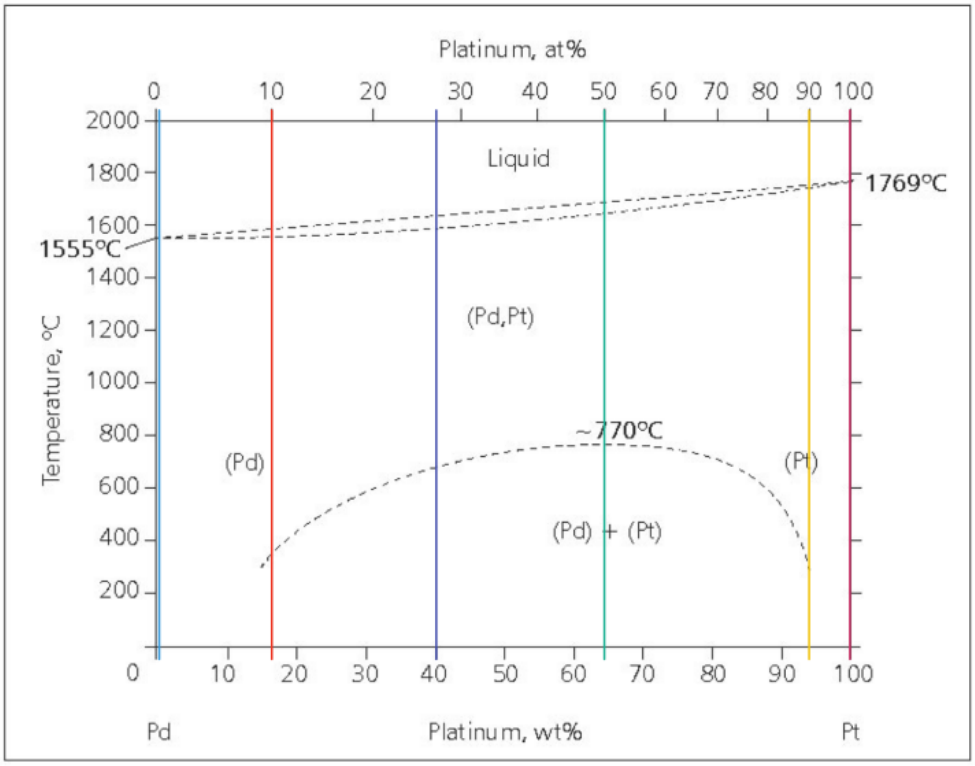

Figure 3.1: The binary phase diagram of Pd-Pt, with six differently coloured, vertical lines representing the six Pt_xPd_{100-x} , $x = \{0.5, 10, 27, 50, 90, 100\}$ samples studied in this thesis using XPS.

The sample preparation by means of sputtering/annealing, oxidation treatment at ambient pressure in the chemistry cell and the collection of the XPS spectra were carried out on the SINTEF-UiO Kratos instrument. This imply that the sample was not brought out in air between sample treatment and XPS data acquisition.

The treatment for the six crystals was comprised of four cleaning and oxidation steps: a) cleaning 1; b) oxidation at 900 ℃; c) cleaning 2; d) oxidation at 500 ℃. A schematic overview of the experimental flow is shown in Figure 3.2. The XPS spectra were collected between each treatment step for all the six samples. The samples were oxidized at 500 ℃ last, because according to the binary phase diagram in Figure 1.3 at this temperature the samples are expected to undergo a phase transition from a solid solution to two segregated phases. To revert to the pristine surface

conditions, such a composition may require extensive surface cleaning by sputtering and annealing.

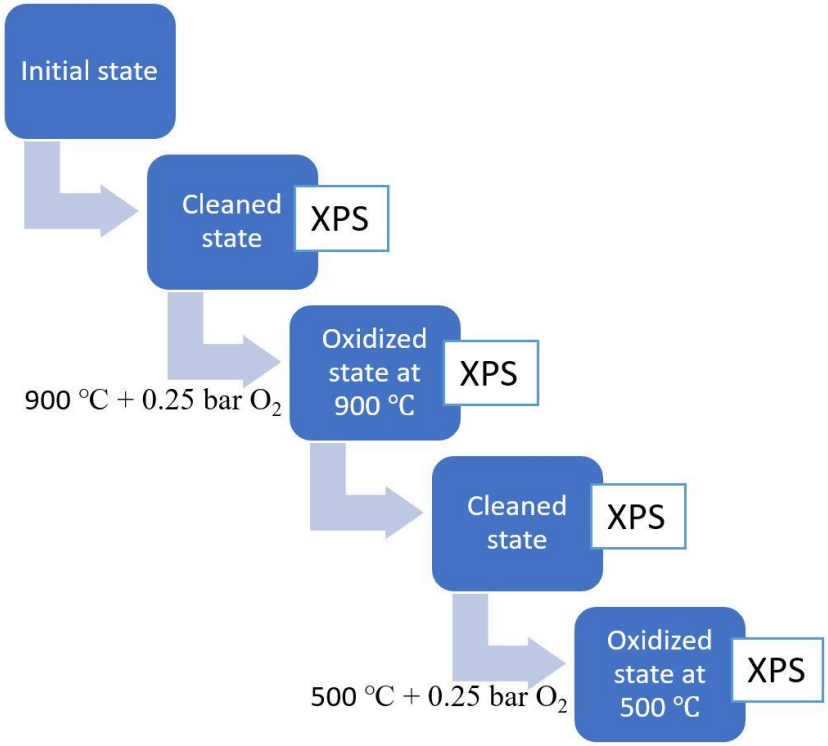

Figure 3.2: The four step experimental flow performed on the six Pt_xPd_{100-x}, $x = \{0.5, 10, 27, 50, 90, 100\}$ samples. The XPS spectra were collected between each treatment step. The first cleaned state is referred to as cleaned 1 and the second state is referred to as cleaned 2.

3.2.1.1 Cleaned 1 and 2

Before acquisition of XPS spectra and between the two oxidation treatments (900 and 500 °C), the alloyed crystals were cleaned with one cycle, consisting of Ar^+ sputtering for 20 min at room temperature with sample current of 7.5 µA and annealing in 1.2 bar Ar at 900 °C for 30 min.

3.2.1.2 Oxidation at 900 °C and 500 °C

Both oxidation treatments were performed in a chemistry cell in 1 bar synthetic air (purity 5.0; 21% O_2, 79% N_2), at 900 °C and 500 °C for 30 min. The partial pressure of O_2 was 0.21 bar. The oxidation was conducted with gas flow of 10 ml/min. After oxidation at 900 °C the sample was cooled to 500 °C in 1 bar of Ar. Cooling below 500 °C was done in an evacuated chamber (1 bar Ar → 10^{-6} mbar).

3.2.2 XPS measurements

X-ray photoelectron spectroscopy was performed using a Kratos Axis Ultra with monochromatized Al Kα source at MiNa lab, Gaustad campus, UiO. The core level spectra were acquired with an analyser pass energy of 20 eV, a dwell time of 0.5 – 1 s, and a step of 0.1 eV. The binding energy was calibrated to Cu $2p_{3/2}$ peak and are reported with an uncertainty ±0.1 eV. Two or three distinct spots per sample were probed and averaged. The fitting of the spectra was performed using the least square curve fitting software WinSpec XP, developed by University of Namur, Belgium [70]. The XPS spectra were made into figures in the data analysis software Origin [71].

4 Results

The two sets of bimetallic surfaces are divided into three sections. Firstly, the PtRh surfaces investigated in an STM, secondly, the PtPd films investigated in an STM, and lastly, the PtPd bulk samples investigated using an XPS are presented separately in the Sections 4.1, 4.2, and 4.3, respectively.

4.1 Rh/Pt(111) surfaces in STM

PtRh surfaces are commonly used as catalysts, for instance in the ammonia oxidation process. High coverage Rh/Pt(111) surfaces was chosen to be studied for this purpose, as well as to further explore and build upon the Pt/Rh(111) and Rh/Pt(111) surfaces previously studied at UiO; see references [24–27] and Section 1.6 in the introduction.

4.1.1 Comparison between two Pt(111) crystals

Two different Pt(111) single crystals were studied in this thesis, see Section 3.1.2. Therefore, it was important to examine if these crystals, which should be identical, would produce the same results. The preparation route chosen to evaluate the two Pt(111) samples was to evaporate Rh at 350 K with a flux rate of 8 nA for 24 min, followed by post annealing at 700 K for 20 min. In Figure 4.1 are some selected STM images of the two obtained surfaces after the aforementioned preparation. The key finding is that the same hexagonal mesh/ honeycomb pattern appears on both crystals. This structure has not been reported before and is described in more detail in Sections 4.1.4 and 4.1.5. However, at this stage the conclusion is that the surface reconstruction is independent of the Pt(111) crystal, and the two crystals are considered to be identical and have a similar cleanliness.

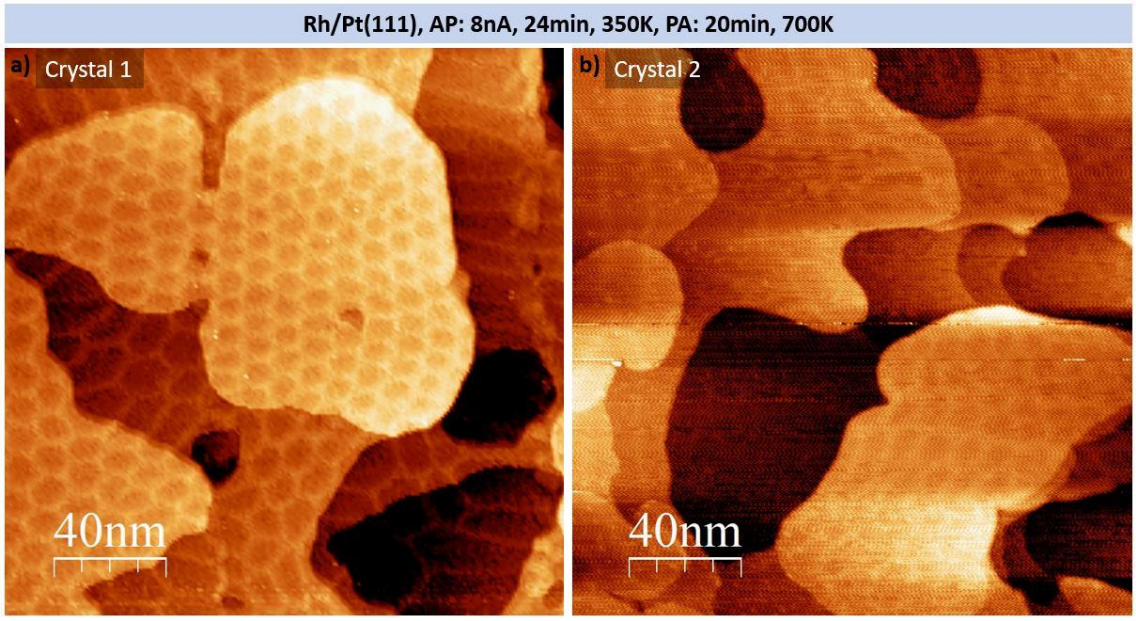

Figure 4.1: Comparison between two Pt(111) single crystals with Rh evaporated at 350 K with 8 nA for 24 min, then followed by post annealing (PA) at 700 K for 20 min. Image **a)** is denoted crystal 1 and image **b)** is crystal 2. The scale is 40 nm for both images.

4.1.2 Role of deposition time for Rh coverage

Previous work of the Pt/Rh(111) and Rh/Pt(111) systems at UiO, [24–27], usually employed a lower deposition time (15 min and shorter). To compliment those results, a deposition time of 24 min at 350 K using a flux of 8 nA was mostly used in this thesis. Eventually, 32 min was also used with the purpose of comparing how the coverage would differ. The STM images from these experiments are reported in Figure 4.2. By comparing images **a)** and **b**) in Figure 4.2, the surfaces seem qualitatively indistinguishable after preparation at 24 and 32 min, respectively. Both STM images show highly uniform triangular islands covering the large terraces and steps. A minor increase in deposition time from 24 to 32 min apparently does not increase the coverage of the surface. The conclusion is therefore that images with a deposition time in the range of 24 min to 32 min can be treated as having comparable coverages. Because this thesis employed a higher deposition time than all the previous work, [24–27], none of the STM images and results were directly comparable. Fortunately, Zheng *et al.* [24] presents lower coverage STM images at similar

deposition temperature. Figure 6 in the paper shows multiple 0.20 ML coverage Rh/Pt(111) surfaces prepared in the temperature range 300 – 700 K. The two images prepared at 300 K and 400 K displays numerous, small, layered islands, formed as triangles or a mix of hexagons and triangles, respectively. When Rh is deposited at 350 K, an intermediate surface between these two are expected to appear, which is an accurate description of the STM images in Figure 4.2. Pettersen *et al.* presented no high coverage Rh/Pt(111) surfaces in neither the article nor the supporting information (SI) [27], however, the lower coverage surfaces (approximately 0.2 – 0.5 ML) have only been reported at small scales. For the purpose of comparison, this makes it difficult to accurately compare the wider scale features, such as coverage, steps, and terraces. Similarly, Ivashenko *et al.* [26] only reports low-scale STM images of Rh/Pt(111). Lastly, Pettersen [25] reports exclusively Pt/Rh(111) STM surfaces. See Section 1.6 for more information on the papers and the thesis.

Based on coverage estimations from experimental data by Pettersen *et al.* [27], the surfaces prepared at 24 and 32 min are expected to have a coverage of 1.5 and 2 ML, respectively. Further details on how the coverage was estimated is found in Section A.1.

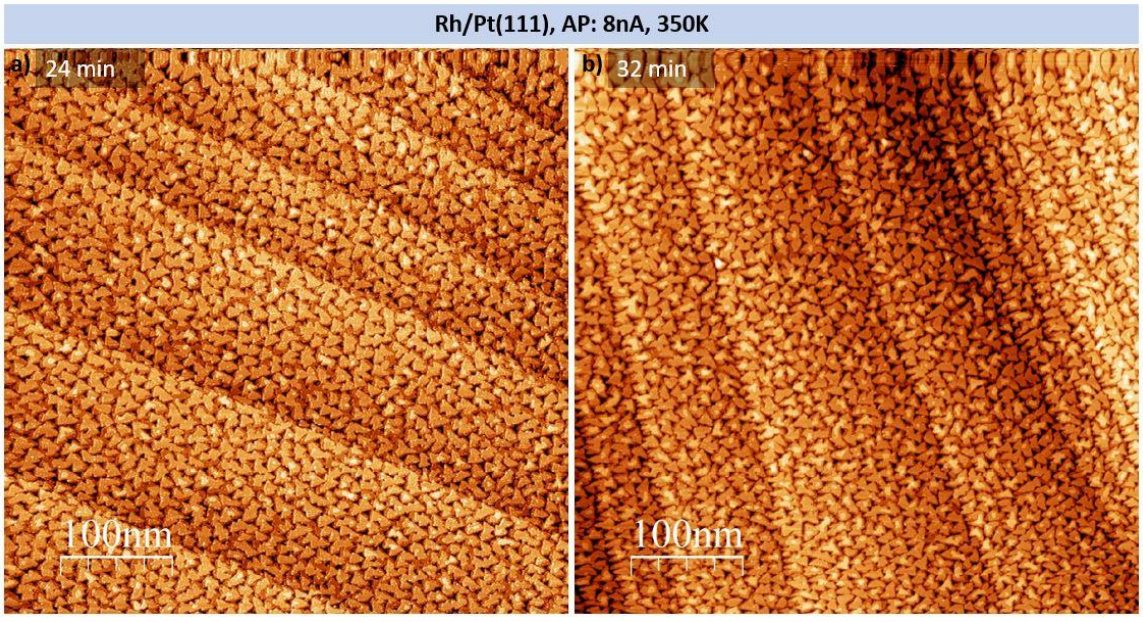

Figure 4.2: STM images of two Rh/Pt(111) surfaces comparing deposition time, when prepared at 8 nA and 350 K. Image **a)** has a deposition time of 24 min and **b)** a time of 32 min. Both images have a scale of 100 nm.

4.1.3 Role of deposition temperature

The Rh/Pt(111) and Pt/Rh(111) surfaces demonstrate a wide range of morphologies and reconstructions over a deposition temperature range of 300 – 700 K, as reported previously at UiO [24–27], especially the roadmap written by Pettersen *et al.* [27] shown in Section 1.6. Based on this, three different Rh/Pt(111) surfaces with varying deposition temperature were prepared: 350 K, 380 K, and 450 K, see Figure 4.3. The flux and time were kept constant at 8 nA and 24 min. With increasing temperature, the triangular islands become larger and starshaped, with elongated edges. Furthermore, between 350 K and 380 K, the surface change to seemingly only one larger terrace-layer. New layers at higher temperatures grow on the existing triangular islands. The surface coverage is quite high for all three temperatures. As for the previous section, Zheng *et al.* [24] can be used to compare the Rh/Pt(111) surfaces deposited at higher temperature with Figure 6. The surfaces at 300 K and 400 K were found to contain small, layered triangles or a mix of the triangles and small, layered hexagons, respectively. Image **a)** prepared at 350 K is a mix between the two temperatures, while image **b)** prepared at 380 K has a surface similar to the surface prepared at 400 K, including the enlargement of the islands. However, Zheng *et al.* reports a surface prepared at 450 K that exhibit little similarities to the surface prepared at 450 K in image **c)**. The surface presented in Zheng *et al.* has few large, uniform, one-layered triangular islands with small nuclei formed in between the islands. Image **c)**, on the other hand, consists of similar triangular islands with elongated arms and multiple layers, also elongated. The shape of the islands therefore more closely resembles stars. Additionally, the small nuclei are not found. Zheng *et al.*'s surface has visible steps and terraces, while the surface in this thesis appears to only have one large terrace.

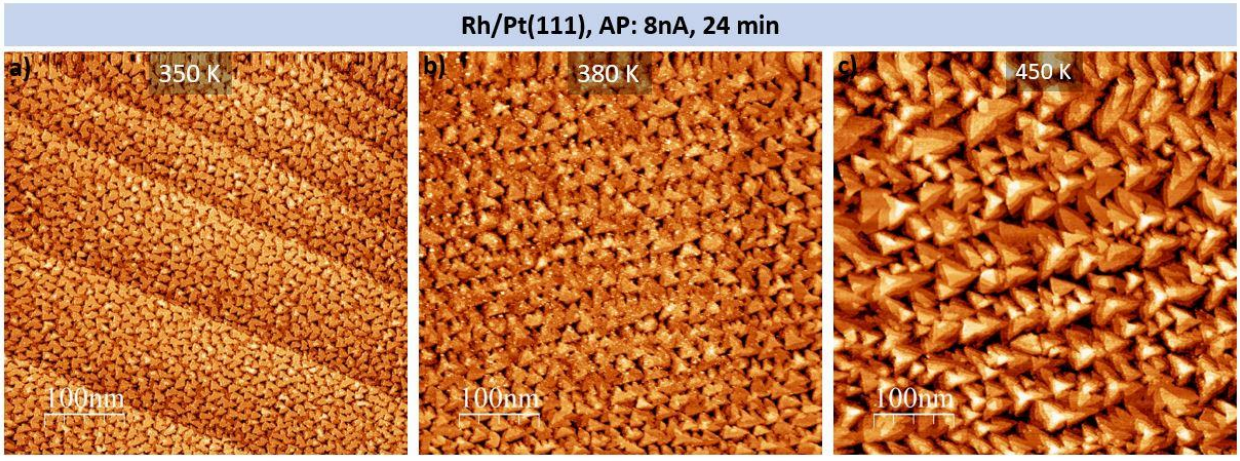

Figure 4.3: STM image of Rh/Pt(111) as prepared at 8 nA and 24 min, with varying temperatures of **a)** 350 K, **b)** 380 K, and **c)** 450 K. All images have a scale of 100 nm.

4.1.4 Role of post annealing of as prepared Rh/Pt(111) surfaces

In Section 4.1.2 it was concluded that Rh/Pt(111) surfaces prepared using Rh deposition time of either 24 or 32 min appear visually identical. Therefore, three surfaces using deposition temperatures of 350, 380, and 450 K with a Rh deposition time of 24 or 32 min were post annealed at 600 K for 20 min to evaluate the effect of post annealing. STM images of the obtained post annealed surfaces are presented in Figure 4.4. By carefully comparing the images reported in Figure 4.3 and Figure 4.4 it can be seen that the post annealing at 600 K removes the for clear step edges for the surface prepared at 380 K and 450 K. In addition, the islands become rounder and larger, with several defects/holes. At 450 K, there are very few islands and a low coverage. Some islands have growth of a few additional layers; however, this is not enough to have compensated for the significant loss of coverage. The most prominent network surface reconstruction is the newly discovered honeycomb pattern or hexagonal mesh, which forms on islands, terraces, and the deeper layers at all three temperatures. This reconstruction additionally continues over the step edges and islands. The hexagons in the honeycomb pattern are highly uniform in size. Around the step edges, the hexagons are mostly elongated in the direction normal to the step edges. Additionally, for the deepest layer of the surface at 450 K, small lines formed between the islands, particularly visible in the top zoomed in image of **c)**. As mentioned in Section 4.1.3, this growth

has been found in Pettersen *et al.* and Zheng *et al.* [24,27], resulting in the expectation that these lines are small nuclei composed of a few atoms.

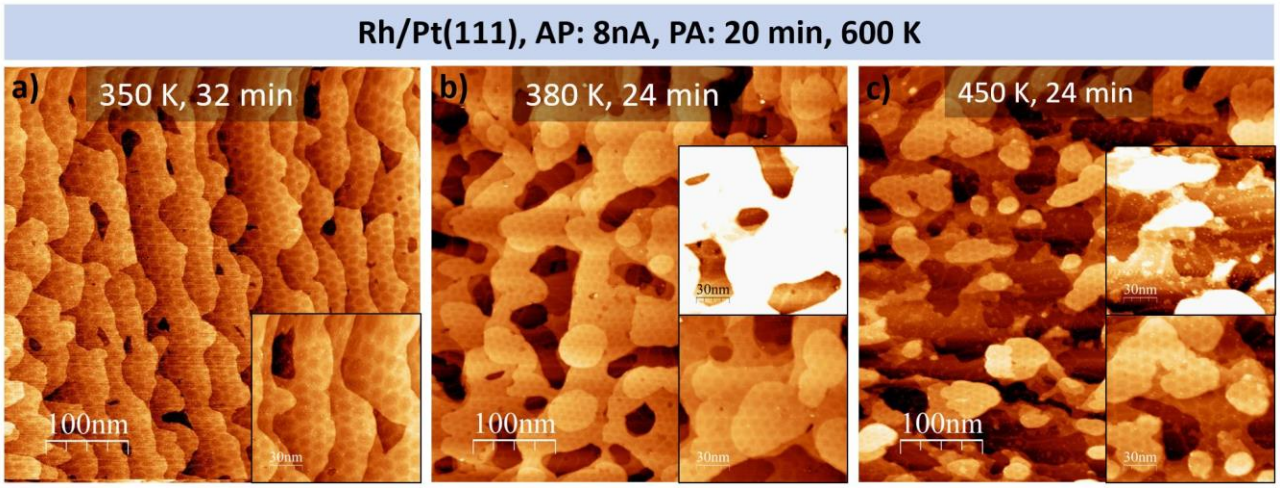

Figure 4.4: Comparison of STM images of Rh/Pt(111) surfaces after post annealing (PA) at 600 K for 20 min. Surface **a)** has been prepared at 350 K for 32 min, surface **b)** at 380 K for 24 min, and surface **c)** at 450 K for 24 min. The larger images have a scale of 100 nm, and the smaller, zoomed in images have a scale of 30 nm.

4.1.5 Comparison of structures formed at various post annealing temperatures

The Rh/Pt(111) surface reconstruction appears at multiple different deposition temperatures using the same post annealing temperature, as concluded above in Section 4.1.4. Varying the post annealing temperature is the next natural step to further understand the reconstruction. Figure 4.5 compares two surfaces prepared at 350 K having similar Rh coverage, but with post annealing temperature of 600 K or 700 K for 20 min. Image **a)** is the same sample as image **a)** from Figure 4.4 and **b)** is a larger scale image of image **a)** from Figure 4.1. Rh was deposited at 32 min and 24 min, respectively, but in Section 4.1.2 it was concluded that the coverage was very similar or identical. The honeycomb pattern appears on both the islands and the terraces in both images, with

continuation over the islands and the steps. The terraces are expanded and larger when annealing at 700 K. There is also formation of larger islands, with larger and deeper vacancies. The vacancies are mostly formed around the steps, not on the terrace Additionally, there appears to be a formation of middle steps with vacancies in the bottom right of image **b)**, Figure 4.6 particularly visualizes these steps.

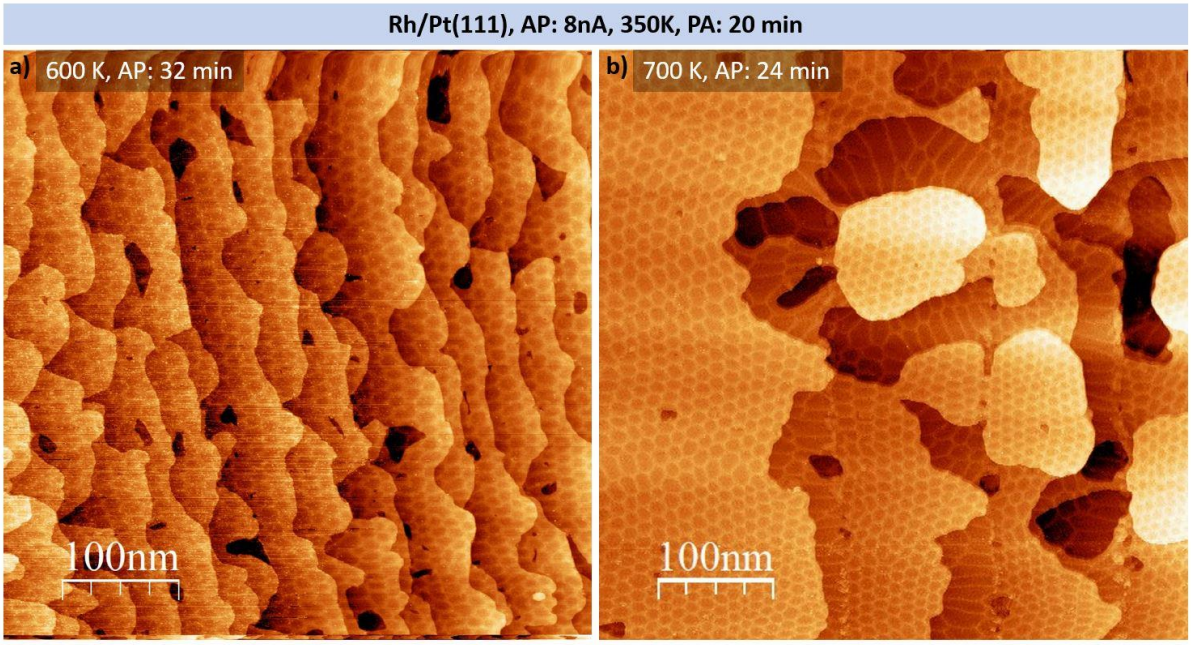

Figure 4.5: Two Rh/Pt(111) surfaces post annealed (PA) at different temperatures and scanned in STM. Image **a)** has been prepared at 350 K for 32 min, followed by post annealing at 600 K for 20 min, and image **b)** has been prepared at 350 K for 24 min, then post annealed at 700 K for 20 min. Both images have a scale of 100 nm.

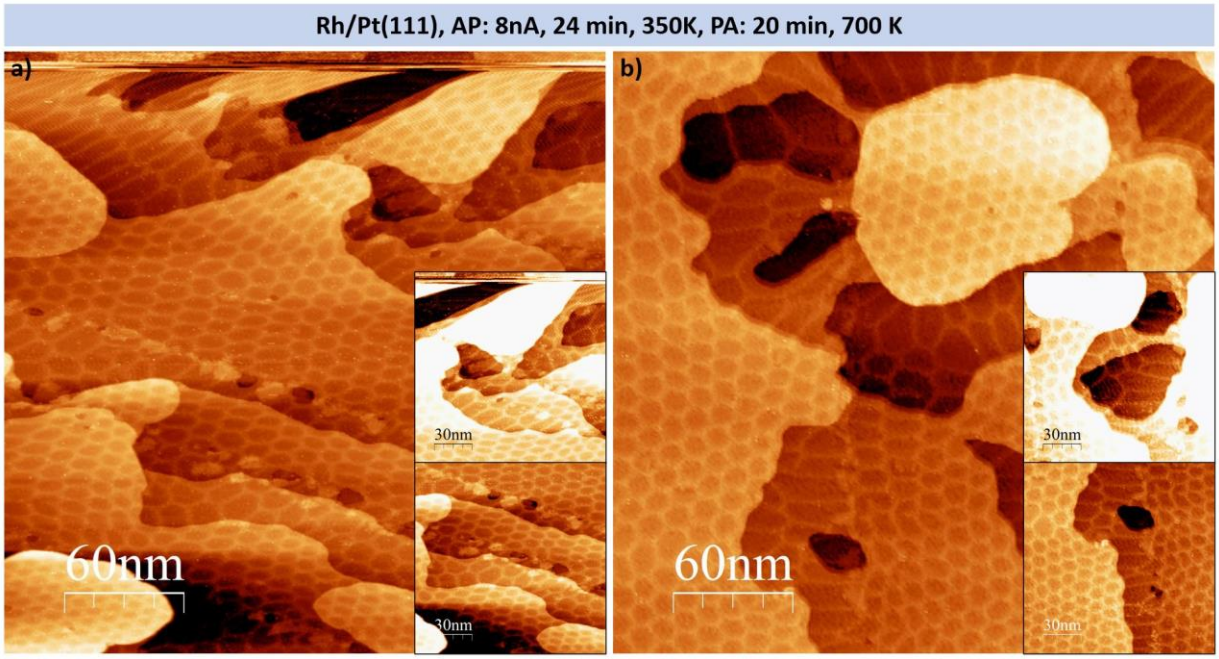

Figure 4.6: Additional STM images to Figure 4.5 of a Rh/Pt(111) surface prepared at 350 K for 24 min and post annealed to 700 K for 20 min, taken during the same scan. The larger images have a scale of 60 nm, and the smaller, zoomed in images have a scale of 30 nm.

4.1.6 Oxidation of Rh/Pt(111) surfaces

Finally, the surfaces are oxidized to examine if the reconstruction is retained. Figure 4.7 displays multiple different surfaces prepared at different temperatures, both with respect to Rh deposition temperature and time, as well as post annealing prior to the oxidation step. At lower deposition temperature, 350 K, with post annealing at 600 K, there are clear honeycomb features, especially seen in image **b)** and **c)**. The prepared surface shown in these images, especially **c)**, indicate formation of Moiré pattern. Compared with Figure 4.26 in the MSc thesis by Pettersen [25], the dots are comparable in size, thus strongly indicating a Moiré pattern. Pettersen further explained that the Moiré pattern originates from oxidation of the surface. Increasing the deposition temperature to 450 K, see images **d)**, **e)**, and **f)**, leads to formation of islands with retained honeycomb pattern, and no visible steps. The deepest layer of the surface has lost the honeycomb pattern, as seen in image **f)**. The small dots seem present for this surface as well. Post annealing at

700 K leads to, in comparison with **a)** and **b)**, a completely different surface. The steps are visible, but irregular because of the multiple rounded, adhered islands. Most interestingly, the honeycomb pattern is destroyed and replaced by a new irregular reconstruction with small islands on top of the terraces. The defects have increased in number and in size. None of the previous works at the ReactorSTM lab at UiO has reported oxidation of Rh/Pt(111) after post annealing [24–27].

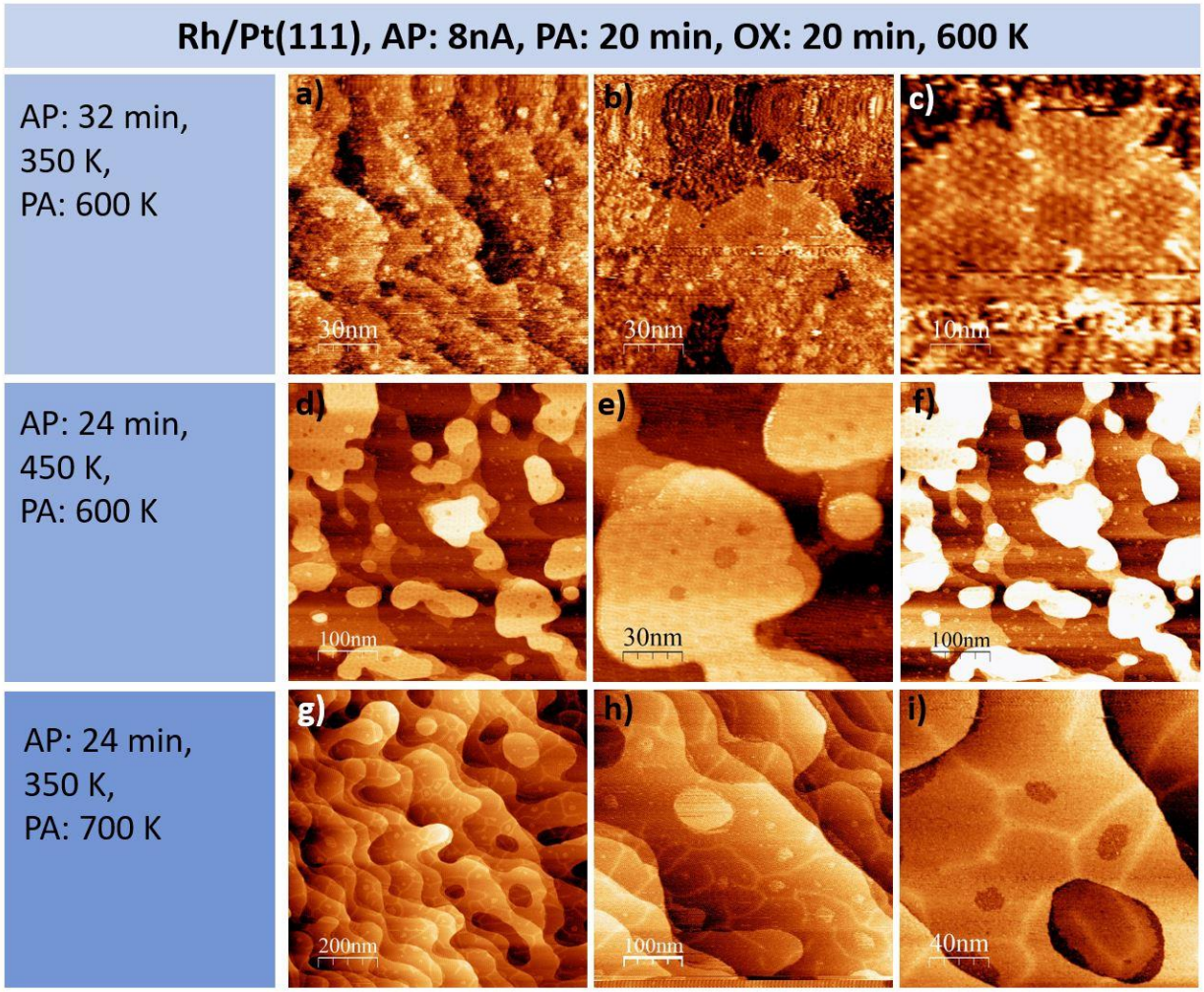

Figure 4.7: STM images of oxidation of various Rh/Pt(111) surfaces. Every surface has been oxidized at 600 K for 20 min after Rh deposition and post annealing at variable conditions. Image **a), b)** and **c)** has both been prepared at 350 K for 32 min with a Rh flux of 8 nA, with subsequent post annealing at 600 K for 20 min, and finally the oxidation described earlier. Image **d), e)** and **f)** has been prepared at 450 K for 24 min with a Rh flux of 8 nA, post annealing at 600 K for 20 min, and oxidation at 600 K for 20 min. Images **g)**, **h)** and **i)** has also been prepared at 350 K for 24 min, with post annealing at 700 K for 20 min, followed by oxidation at 600 K for 20 min. The scale varies between 30 nm and 200 nm for the images.

4.2 Pd/Pd(111), Pt/Pd(111), and Pd/Pt(111) surfaces in STM

Surfaces containing both Pt and Pd can for instance be obtained in two ways: 1) depositing Pd on a Pt single crystal, and 2) depositing Pt on a Pd single crystal. In this study, surfaces of both Pt/Pd(111) and Pd/Pt(111) have been prepared as well as Pd/Pd(111), by evaporating Pt or Pd using electron beam evaporation (EBE) onto a Pt(111) or Pd(111) surface followed by various post annealing treatments and oxidation steps (see details in Section 3.1.3). Surface morphologies are subsequently visualized by means of STM imaging. The results obtained for the three surfaces Pd/Pd(111), Pt/Pd(111), and Pd/Pt(111) are presented in Sections 4.2.1, 4.2.2, and 4.2.3 respectively.

4.2.1 Pd/Pd(111) surfaces

Pd/Pd(111) surfaces were prepared by depositing Pd with an evaporation rate of 5 nA for 10 minutes on a Pd(111) crystal kept at 460 K. In Figure 4.8, three representative STM Pd/Pd(111) images are presented. The obtained Pd/Pd(111) surface shows very uniform and periodic steps. Multiple islands have grown very close to the steps, though they seem to not be fully connected. Small holes continuously separate the steps from the islands. The islands seem to have some facets with no easily recognisable shapes, except that they grow significantly more in the normal direction to the steps. These islands grow to become almost as large as the terraces themselves. Overall, the STM images show a preferential growth along the Pd(111) steps rather than terraces. At the time of writing, there was not found any literature where a Pd/Pd(111) surface was studied with an STM.

It should finally be noted that the Pd(111) single crystal proved difficult to work with during scanning. This is because of a substantial amount of noise and interference, as visible in the top of image **c)** in Figure 4.8.

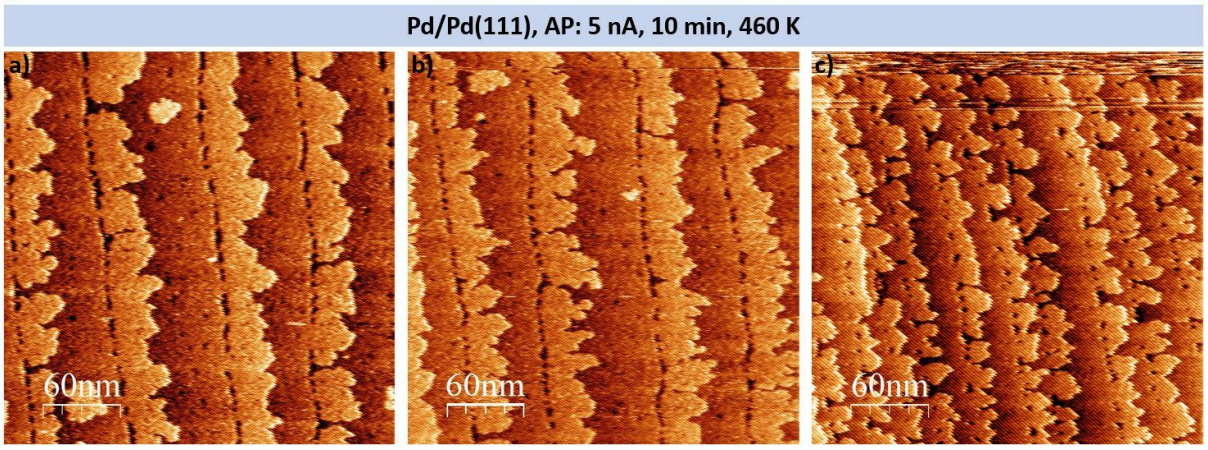

Figure 4.8: Representative STM images of a Pd(111) single crystal with Pd deposited with a 5 nA deposition rate for 10 min at 460 K. The three images **a)**, **b)**, and **c)** are taken on different areas of the same sample during a scan. The scale is 60 nm for all three images

4.2.2 Pt/Pd(111) surfaces

The next focus was to examine the morphology and topography of the same Pd(111) single crystal as used in Section 4.2.1, now with Pt deposited on top. The purpose of the experiments was to evaluate the role of Pt deposition time and deposition temperature on the morphology, while using a constant Pt deposition rate. Only some few experiments were successfully carried out as the Pd(111) single crystal became increasingly difficult to work with during Pt deposition than Pd deposition, as seen in Section 4.2.1. Preliminary STM measurements of Pd/Pd(111) and Pt/Pd(111) showed rough surfaces with high density of corrugated steps, which suggested that the annealing temperature should be increased to 1100 K. Additionally, the applied cleaning procedures did not bring sufficiently cleaned surfaces possibly due to too mild sputtering and need for more cleaning cycles to get rid of contaminations segregating from the Pd(111) bulk onto the surface, as is especially visible by the large mountain like features, which are dirt, present in the STM images **a)** and **b)** in Figure 4.9. From the large scale used in the images, the amount of dirt is clearly substantial, thereby causing problems with scanning. Despite over 30 cleaning cycles, as described in Section 3.1.2, the Pd crystal surface was still not clean enough to get good, reliable results. However, some representative STM images were taken, which are displayed in Figure 4.9.

The three surfaces obtained and presented in Figure 4.9 were prepared with a Pt deposition rate of 12 nA and deposition temperatures of 410, 450, and 475 K for 5, 15, and 15 minutes respectively. Images **a)** and **b)** depict the surface prepared at 410 K for 4 min. The surfaces prepared at 450 K for 15 min, see images **c)**, **d)**, **e)**, and prepared at 475 K for 15 min, see images **f)**, **g)**, **h)**, look very similar. Both has clear formation of uniform steps and smaller flower-like shapes islands over both terraces and steps. The main difference is the formation of islands which are somewhat connected to the step edges. The Pt/Pd(111) sample prepared at 475 K has a higher resemblance to the Pd/Pd(111) surface shown in Figure 4.8, which was prepared at 460 K, because of the smaller holes separating the islands from the step edge. The Pt/Pd(111) sample prepared at 450 K has some of these holes, but the islands are generally more connected to the step edges. Therefore, it seems as when increasing the temperature, the islands will be more disconnected and form separate islands. In addition, the Pt/Pd(111) sample prepared at 450 K has more of the flower-like shaped islands decorating the terraces and steps. Contradictorily, the opposite is expected to happen. With increasing temperature, such islands normally form larger and smoother facets, and often becomes indistinguishable from the steps.

At the time of writing, there was additionally not found any literature on Pt/Pd(111) surfaces studied with an STM.

Some additional Pt/Pd(111) images are presented in the appendix, see Figure A.8.1.

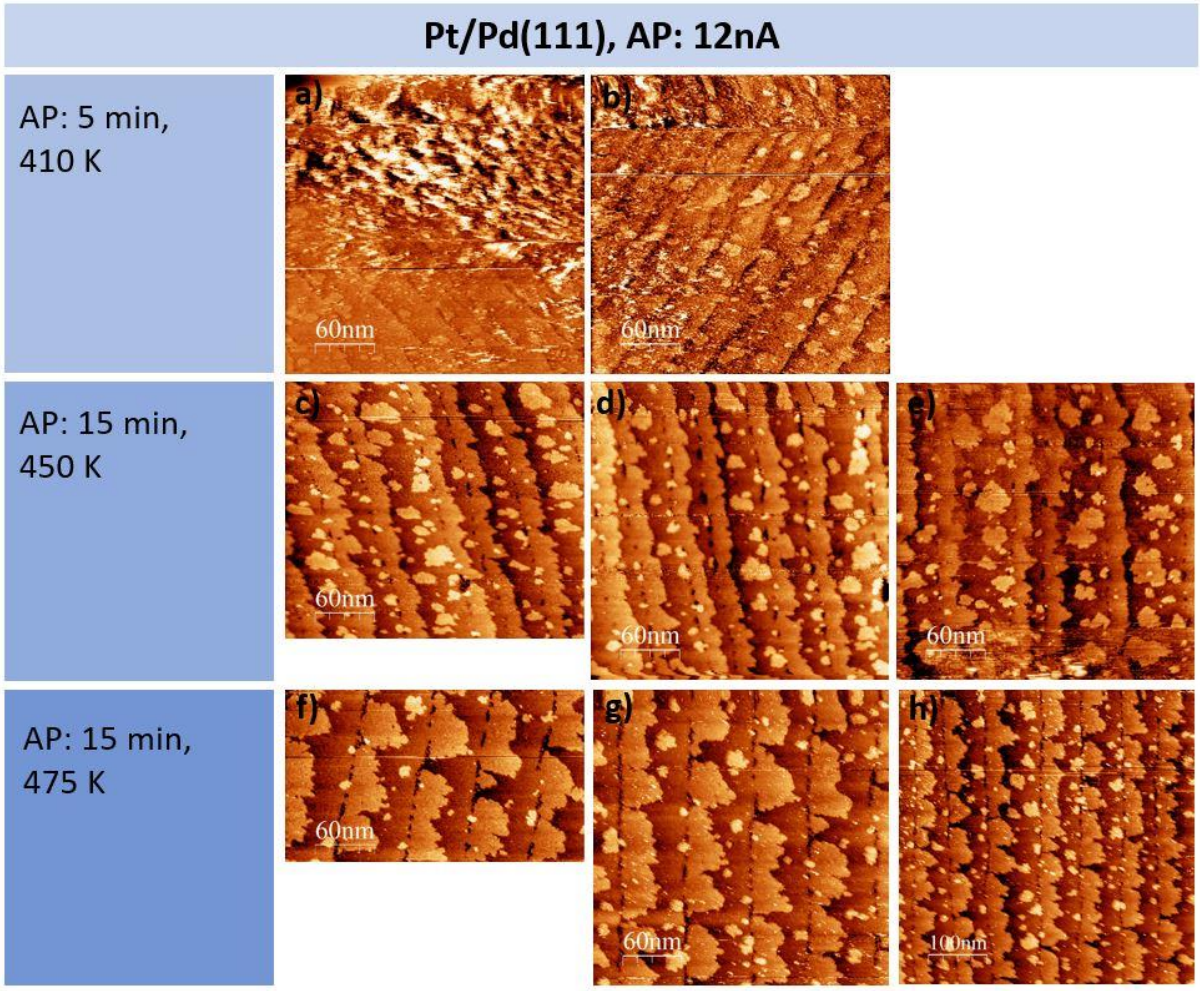

Figure 4.9: STM images of Pt/Pd(111) surfaces prepared by depositing Pt at three different substrate temperatures and deposition time. Images **a)** and **b)** had Pt deposited at a rate of 12 nA for 5 min at 410 K. Images **c)**, **d)**, and **e)** had Pt deposited at a rate of 12 nA for15 min at 450 K. Images **f)**, **g)**, and **h)** had Pt deposited at a rate of 12 nA for 15 min at 475 K. All images have a 60 nm scale, except **f)** which has 100 nm.

Finally, it should be noted that after these experiments, the Pd(111) single crystal was not used anymore. The sample proved too difficult to work with, both in the sense that the surface had quite a lot of dirt and that the images were heavily impacted by a significant amount of interference.

4.2.3 Pd/Pt(111) surfaces

In this section, Pd/Pt(111) surfaces are presented as a function of deposition time (coverage) and deposition temperature. Additionally, some Pd/Pt(111) surfaces were post annealed (PA) at 700 K for 30 min and studied as a function of deposition temperature. Finally, two Pd/Pt(111) surfaces were oxidized at 700 K for 30 min in a p(O_2) of both 10^{-7} and 10^{-5} mbar and compared. The Pt(111) single crystal has been used for a couple of years and yielded good results. The possibility to compliment the Pt/Pd(111) results was high.

The first focus is to examine the coverage of the surface. Two Pd/Pt(111) surfaces were prepared by depositing Pd at a deposition rate of 9 nA for either 15 or 60 min, while keeping the substrate temperature at 400 K. The obtained STM images of the surface are presented in Figure 4.10. Image **a)** had Pd deposited for 15 min, and **b)** and **c)** for 60 min. Comparing the images shows a significant increase in coverage with a longer deposition time. Image **a)** depicts clear steps and terraces with some islands adhered to the step-edges. Additionally, other small islands can be seen as small white dots. In contrast, the terraces and edges are completely covered with multiple monolayers, seen in image **b)** and **c)**. Unfortunately, intermediate deposition times were not performed to visualize the transitions.

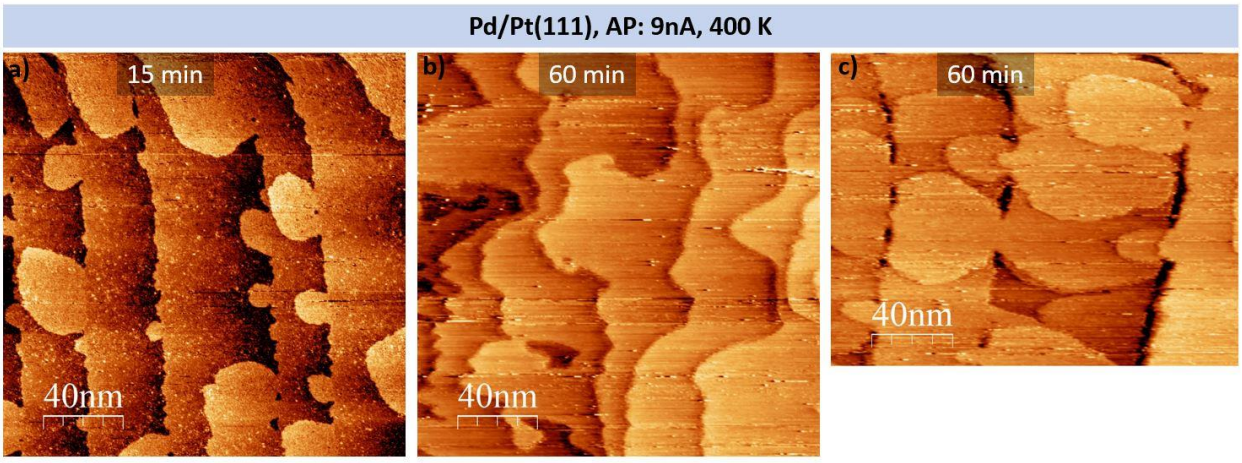

Figure 4.10: STM images of two Pd/Pt(111) samples prepared with a deposition flux of 9 nA at a substrate temperature of 400 K, but the deposition time for image **a)** was 15 min, and image **b)** and **c)** was 60 min. All images have a scale of 40 nm.

The effect of different deposition temperatures on the morphology is evaluated next. In Figure 4.11, two samples prepared at two different temperatures are presented. Image **a)** and **b)** show the same surface scanned two days apart. This sample had an as prepared (AP) temperature of 450 K, while the surface presented in STM image **c)** was prepared at 500 K. Both surfaces were prepared for 6 min with a deposition flux of 6 nA. Preparing the Pd/Pt(111) surface at 450 K results in clear step edges and terraces, with some larger islands decorating the step edges and smaller islands decorating the terraces. The sample prepared at 500 K has multiple islands decorating the step edges, resulting in less defined step edges. These islands appear in multiple different sizes. The smaller islands decorating the terraces in the other images, appear now at a higher frequency. Dirt is present in all images, as well as interference. The dirt is more likely stemming from lack of cleaning cycles when the Pt(111) single crystal was prepared. Nevertheless, good quality areas are visible of all three images.

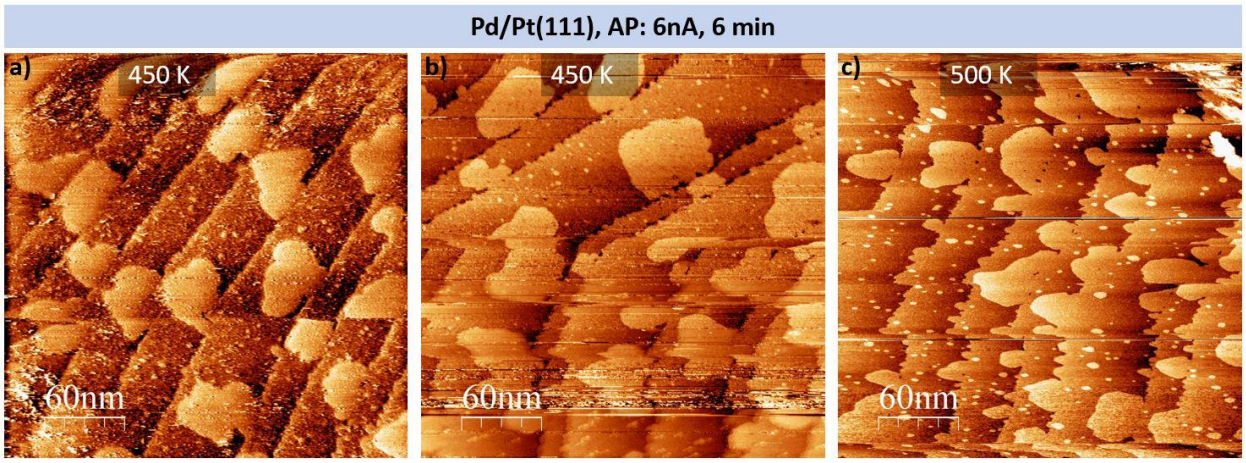

Figure 4.11: STM images of two Pd/Pt(111) samples prepared with a flux of 6 nA for 6 min with different deposition (AP) temperatures. The temperature for the surface in image **a)** and **b)** was 450 K, and for the surface in image **c)** was 500 K. Image **a)** and **b)** are the same surface scanned two days apart. All images have a scale of 60 nm.

It is well known that post annealing (PA) will change the surface significantly, as illustrated in Section 1.6.1 for literature on Rh/Pt(111) [24] and the obtained results in this thesis for Rh/Pt(111)

in Section 4.1. Based on this, it was decided to evaluate the effect of PA on the Pd/Pt(111) surface as a function of deposition temperature. The two obtained surface are presented in Figure 4.12 after PA at 700 K for 30 min. Image **a)** depicts a surface with Pd deposited on a Pt(111) single crystal with a flux of 6 nA for 6 min with a temperature of 400 K, while image **b)** was prepared at 500 K, with the same flux for equally long. The surface prepared at 400 K has multiple larger islands covering the terraces, some smaller islands on the terraces too, and some islands adhered to the step edges, resulting in the irregularity of the step edges. The surface prepared at 500 K also has these smaller islands, but the larger islands are adsorbed into the surface, making the step edges look more irregular. Some of the larger islands are retained, as seen to the lower left of image **b)**. Interference is visible in both images, particularly image **a)**.

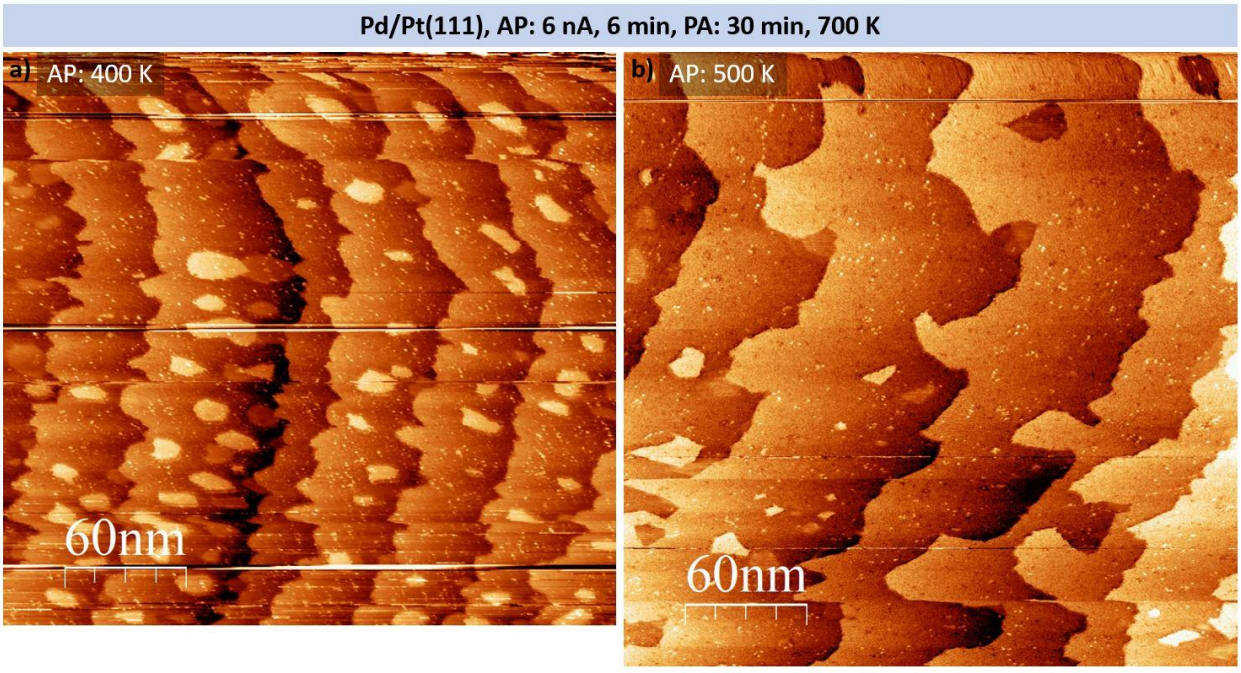

Figure 4.12: STM images of two Pd/Pt(111) samples prepared with different deposition (AP) temperatures, imaged after subsequent post annealing (PA). The samples have been prepared with a Pd deposition rate of 6 nA and 6 min, and post annealed at 700 K for 30 min, but the AP temperature for image **a)** was 400 K, and image **b)** was 500 K. All images have a scale of 60 nm.

Lastly, oxidation of the Pd/Pt(111) surfaces were performed. Figure 4.13 below depicts two surfaces prepared differently in the as prepared step, but identically for the subsequent oxidation step. The oxidation was performed at 700 K for 30 min. The surface in image **a)** was prepared with a Pd deposition rate of 6 nA for 6 min at 450 K, while **b)** and **c)** was prepared with a Pd deposition rate of 9 nA for 15 min at 400 K. The two surfaces were prepared at considerably different conditions, nevertheless, interesting features are depicted. For instance, the surface in image **a)** has multiple islands adhered to the step edges which are elongated in the normal direction to the step edge. Some smaller islands are decorating both these adhered islands and the terraces. Meanwhile, image **b)** and **c)** depicts a surface with holes in these adhered islands, as well as more clear and uniform step edges. Some of the smaller islands are formed, but they are somewhat larger.

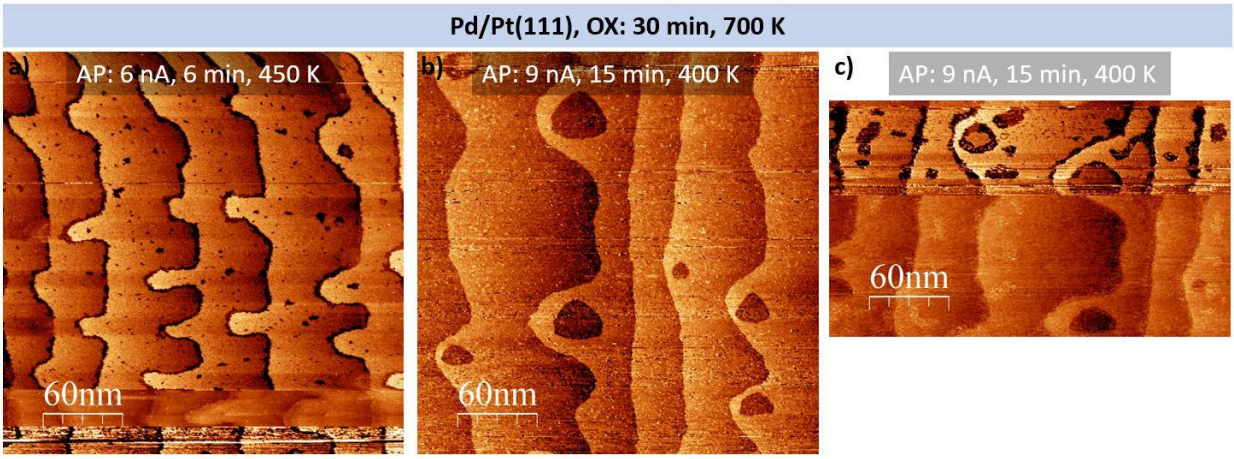

Figure 4.13: Two Pd/Pt(111) samples prepared with different Pd deposition (AP) conditions, imaged with an STM after subsequent oxidation (OX). The AP conditions for image **a)** was Pd deposition rate of 6 nA for 6 min at 450 K, and image **b)** and **c)** was Pd deposition rate of 9 nA for 15 min at 400 K. The samples have been oxidized at 700 K for 30 min in an oxygen pressure of **a)** 10^{-7} mbar, and **b)** and **c)** 10^{-5} mbar. All images have a scale of 60 nm.

Two papers on as prepared Pd/Pt(111) surfaces, see Sections 1.7.1 and 1.7.2, were found [28,29]. Narihiro *et al.* [28] prepared Pd/Pt(111) surfaces with a deposition of Pd at RT, with coverage between 0.043 and 0.73 ML, and scanned in an STM at RT. Umezawa *et al.* [29] prepared their Pd/Pt(111) identically, but obtained surface at other coverages (0.13 and 0.9 ML). When comparing the AP surfaces prepared at 400 K for 15 and 60 min obtained in this thesis, see Figure

4.10, with the surfaces obtained by Narihiro *et al.* and Umezawa *et al.*, see Figure 1.11 and Figure 1.12, respectively, our surfaces are not similar to the reported surfaces. Our obtained surfaces have islands that are more uniform in the morphology, as well as only a few defects in the surface. In contrast, the AP surfaces prepared at 450 and 500 K for 6 min, see Figure 4.11, are much more similar to the reported surfaces. Our surfaces and the reported surfaces are featured with irregular shaped islands, defects, and smaller ad-islands. Both Narihiro *et al.* and Umezawa *et al.* do not report PA surfaces and oxidized surfaces. At the time of writing, there was not found any papers studying the effect of PA and oxidation on Pd/Pt(111) surfaces.

4.3 XPS analysis of Pt_xPd_{100-x} samples

In this section the results of the XPS analysis of the Pt_xPd_{100-x} ($x = \{0.5, 10, 27, 50, 90, 100\}$) samples, which are shortened to Pt_x or Pt*x*, are reported. The samples used in the study are described in Section 3.2.1, and the experimental flow with respect to chemical treatment is described in Figure 3.2. The initial state of the alloyed samples is defined to be after the first cleaning and is denoted "cleaned 1". The second cleaning, here denoted "cleaned 2", was performed in between the two oxidation steps at 900 ℃ (1173 K) and at 500 ℃ (773 K). XPS spectra of all the samples were collected after each of the four mentioned treatments. The oxidations of the samples were carried out in $p(O_2)$ = 0.21 bar (157.5 Torr).

In Section 4.3.1 the XPS results for the samples at the conditions described for cleaned 1 and cleaned 2 are presented, whereas in Sections 4.3.2 and 4.3.3, are the corresponding data for the samples oxidized at 900 ℃ and 500 ℃ reported, respectively. An overview of the findings is presented in Section 4.3.4, with a table summarizing the found binding energies and their assigned species, see Table 4.1. In addition, the sample treatments will be compared in the aforementioned section.

As per the writing of this thesis, there were no publications found which have done a systematic study of samples, such as done in this thesis.

4.3.1 Pt_xPd_{100-x} samples after cleaned 1 and cleaned 2

The XPS spectra of cleaned 1 and cleaned 2 of the Pt_xPd_{100-x} ($x = \{0.5, 10, 27, 50, 90, 100\}$) samples were considered to be comparable and are therefore presented together in this section. In the following sections, XPS spectra of the Pt 4*f*, Pd 3*d*, and O 1*s* are presented individually.

4.3.1.1 Pt 4f

A doublet peak was found for the XPS spectra of both cleaned 1 and cleaned 2, as seen in Figure 4.14. The main doublet component, Pt $4f_{7/2}$, was located at 70.8 ± 0.2 eV, with a doublet separation of 3.33 eV, see Table 4.1. Both of these values are in very good agreement with literary values for the spectrum of Pt metal, specifically when combining the separated surface and bulk values found by Puglia *et al.* [30] and Miller *et al.* [31] at 70.7 eV. However, Parkinson *et al.* [32] reports this binding energy at 71.2 eV. This value is 0.5 – 0.6 eV higher than what is found in this thesis, as well as what Puglia *et al.* and Miller *et al.* have reported. As expected, the amount of Pt $4f_{7/2}$ metal increases with increasing Pt amount in the samples.

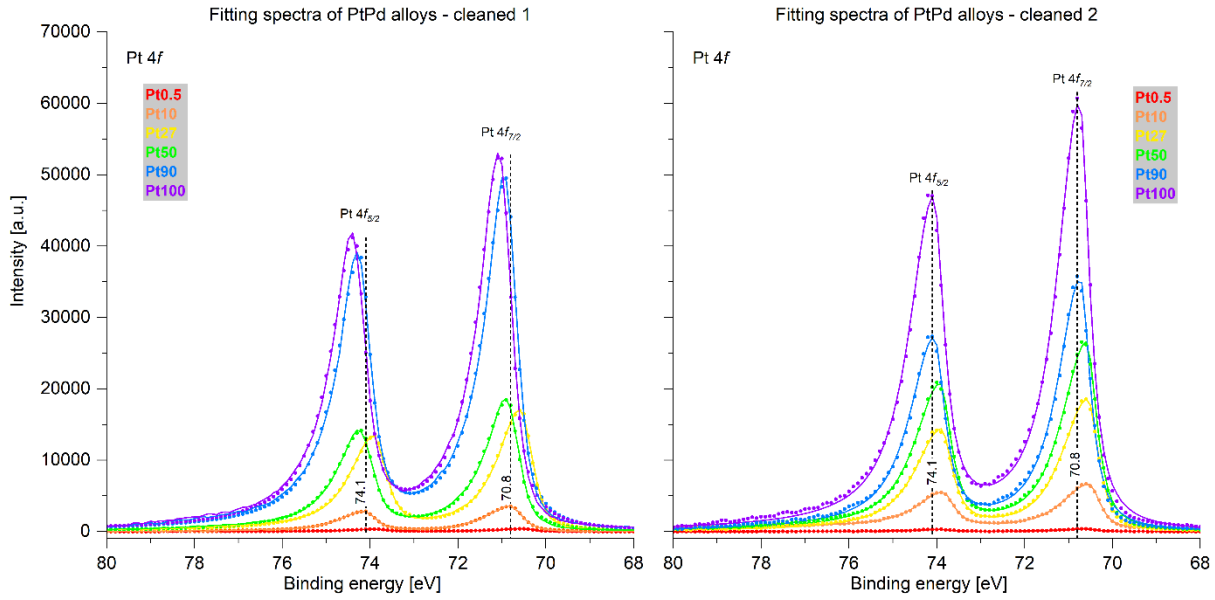

Figure 4.14: Pt 4*f* XPS spectra of cleaned 1 (left) and cleaned 2 (right), for all six Pt_xPd_{100-x} ($x = \{0.5, 10, 27, 50, 90, 100\}$) samples. The intensity scale is identical for the two plots. The scattered plots labelled "r" in the legend represents the raw data, and the line plots labelled "t" represents the total fit.

4.3.1.2 Pd 3d

The XPS spectra for the five Pt_xPd_{100-x} ($x = \{0.5, 10, 27, 50, 90\}$) alloys for the Pd 3*d* core level after the treatments cleaned 1 and cleaned 2 are presented in Figure 4.15 below. Pt100 is not included because it is a pure Pt sample, thus no peaks associated with Pd species will be found. In total, five contributions were found. The two most intense contributions have a binding energy of 334.9 ± 0.2 eV and 340.3 ± 0.2 eV and are attributed to Pd $3d_{5/2}$ and Pd $3d_{3/2}$ metal species, respectively. According to Zemlyanov *et al.* [34] the Pd $3d_{5/2}$ metal peak is expected at 334.9 eV and Pd $3d_{3/2}$ metal peak at 340.3 eV, which is in perfect agreement with the binding energies found in this thesis. The third most intense peak is located at 331.2 ± 0.1 eV and originates from Pt $4d_{3/2}$ metal. Shyu *et al.* [33] found this species at 331.2 eV, again in prefect agreement with our value.

Additionally, two smaller peaks are visible at 341.5 ± 0.5 eV and 346.7 ± 0.4 eV. These are assigned to plasmon loss peak Pd $3d_{5/2}$ and plasmon loss peak Pd $3d_{3/2}$, respectively. Militello *et al.* [40] found the plasmon peaks at 342.1 eV and 346.6 eV for Pd $3d_{5/2}$ and Pd $3d_{3/2}$, respectively. Our range for Pd $3d_{5/2}$ is just narrow enough to not include the value found by Militello *et al.*, but the Pd $3d_{3/2}$ value is in very good agreement. For Pt90, the plasmon loss peaks are harder to distinguish due to lower proportion of Pd in the sample. All samples, except Pt0.5, have a clear Pt $4d_{3/2}$ metal component, which grows with increasing Pt content. Oxide peaks, expected at higher binding energies, are not present in the spectra of either cleaned 1 or 2. All the species with their binding energies are presented in Table 4.1.

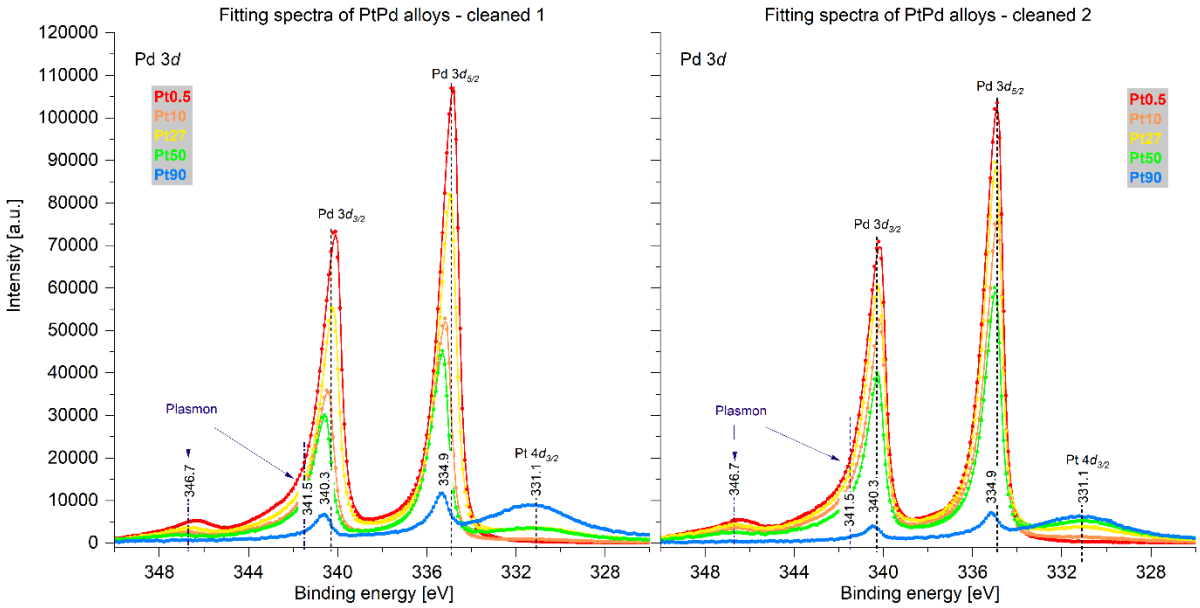

Figure 4.15: Pd 3*d* XPS spectra of cleaned 1 (left) and cleaned 2 (right), for the five Pt_xPd_{100-x} ($x = \{0.5, 10, 27, 50, 90\}$) alloys, as they contain Pd. The intensities are identical between the spectra. The scattered plots labelled "r" in the legend represents the raw data, and the line plots labelled "t" represents the total fit.

4.3.1.3 O 1s

In Figure 4.16 below the XPS spectra of O 1*s* for cleaned 1 and cleaned 2, in the range 510 eV to 545 eV, are presented. Some Pt and Pd contributions are cut out because the O 1*s* species in this region, which are the main focus, have significant overlap, therefore a smaller energy range allows for a better energy resolution in the spectra. All peaks, and the peaks that have been excluded from the spectra, are presented in Table 4.1. The most intense peak is located at 532.0 ± 0.2 eV and is attributed to Pd $3p_{3/2}$ metal. This value is not in agreement with Militello *et al.* [40], which is 534.3 eV, however, Smirnov *et al.* [43] reports Pd $3p_{3/2}$ bulk at 532.2 eV, which is in good agreement. The Pd $3p_{1/2}$ metal peak of this doublet is located outside of this chosen area, see Table 4.1 for the binding energy. The second most intense peak is found at 519.2 ± 0.5 eV and assigned to Pt $4p_{3/2}$ metal. This species was found by Nyholm *et al.* [41] to be at 519.5 eV, which is in good agreement with our value. The third peak found in this area is located at 538.0 ± 0.6 eV. It is assigned as plasmon loss peak Pd $3p_{3/2}$. The other plasmon loss peak is located beyond the selected area, see summary in Table 4.1. Militello *et al.* [40] found the plasmon loss peaks at 537.8 eV for Pd $3p_{3/2}$ and 565.6 eV for $3p_{1/2}$. The plasmon loss peak for Pd $3p_{3/2}$ is in good agreement, but the peak for $3p_{1/2}$ is just out of our range.

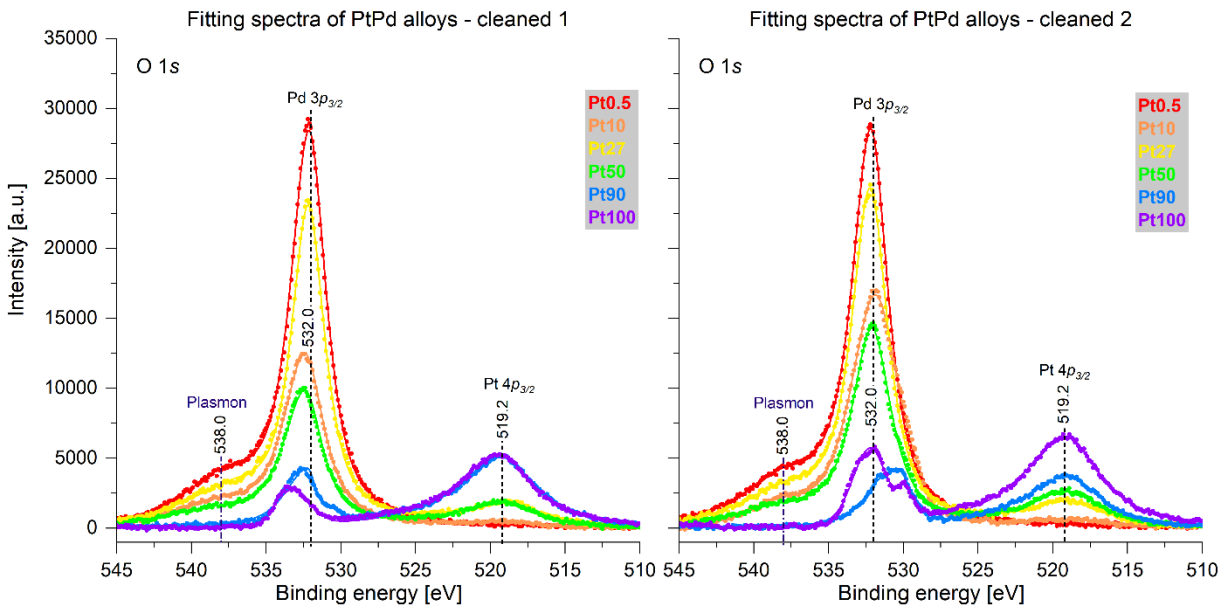

Figure 4.16: O 1*s* XPS spectra of the six Pt_xPd_{100-x} ($x = \{0.5, 10, 27, 50, 90, 100\}$) samples cleaned 1 (left) and cleaned 2 (right). The relative intensity is comparable between the spectra. The scattered plots represent the raw data, and the line plots represent the total fit.

4.3.1.4 Conclusion

In sum it can be concluded that XPS analysis only give contributions from the two metal components, and the identified binding energies are mostly, however only with small deviations, in line with reported literature. Additionally, there was no indication of any oxygen species observed.

4.3.2 Pt_xPd_{100-x} samples after oxidation at 900 °C

The second sample treatment performed on the Pt_xPd_{100-x} ($x = \{0.5, 10, 27, 50, 90, 100\}$) samples was oxidation at 900 °C, see Figure 3.2 in Section 3.2.1 for information about the experimental flow. This oxidation treatment is performed to evaluate the Pt catchment material used during the Ostwald process, which is carried out at this temperature. See Section 1.3 and Section 1.4 for more

information about the Ostwald process and Pt catchment materials, respectively. In the following sections the Pt 4*f*, Pd 3*d*, and O 1*s* core levels are presented individually.

4.3.2.1 Pt 4f

Two peaks were found for the Pt 4*f* XPS spectra of the six samples after oxidation at 900 °C, see Figure 4.17. As for the corresponding spectra cleaned 1 and cleaned 2, shown in Figure 4.14, the peaks are located at the same binding energies, 70.8 ± 0.2 eV and 74.1 ± 0.3 eV, and therefore also assigned to Pt $4f_{7/2}$ and Pt $4f_{5/2}$ metal peaks, respectively. Additionally, they are in good agreement with literature [30,31].

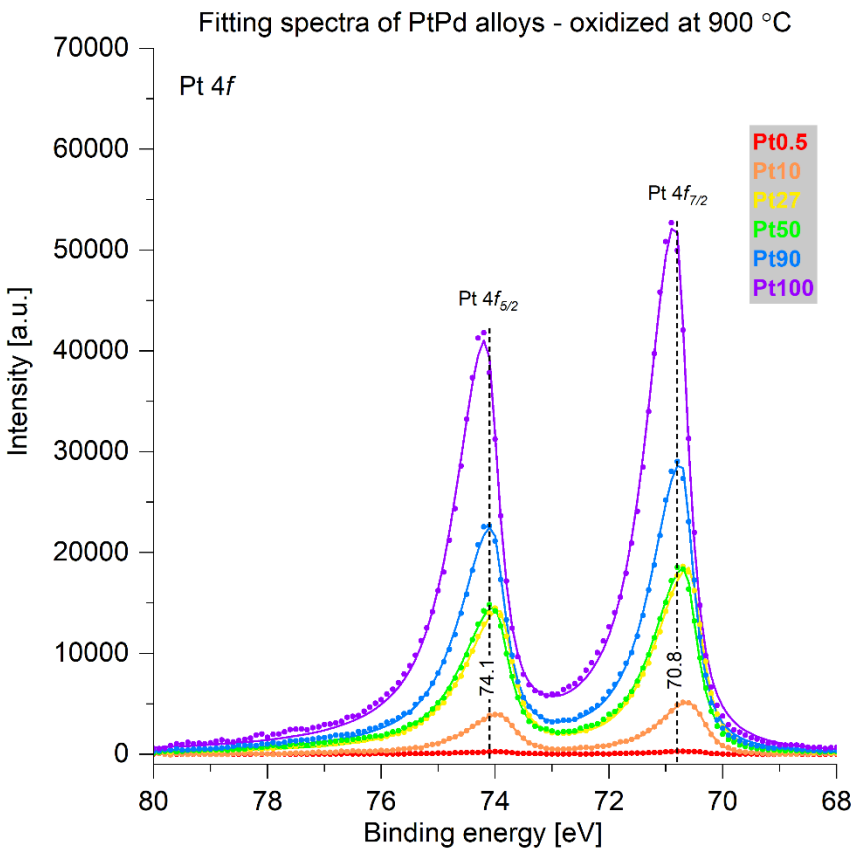

Figure 4.17: XPS spectra of Pt 4*f* for the six Pt_xPd_{100-x} ($x = \{0.5, 10, 27, 50, 90, 100\}$) samples oxidized at 900 °C. The scattered plots labelled "r" in the legend represents the raw data, and the line plots labelled "t" represents the total fit.

4.3.2.2 Pd 3d

In total, nine peaks were found for the Pd 3*d* core level spectra for the five Pt_xPd_{100-x} ($x = \{0.5, 10, 27, 50, 90\}$) alloys oxidized at 900 °C, as shown in Figure 4.18 below. As for cleaned 1 and cleaned 2, see Figure 4.15, the two most intense peaks have binding energies of 334.9 ± 0.2 eV and 340.3 ± 0.2 eV and are attributed to Pd $3d_{5/2}$ and Pd $3d_{3/2}$ metal peaks, respectively. They are in good agreement with literature [34]. The third most intense peak is located at 331.2 ± 0.1 eV and is assigned to Pt $4d_{3/2}$ metal, in perfect agreement with [33] as shown for cleaned 1 and cleaned 2 in Section 4.3.1.2. Additionally, two smaller peaks are visible at 341.5 ± 0.5 eV and 346.7 ± 0.4 eV. These are assigned to plasmon loss peak Pd $3d_{5/2}$ and plasmon loss peak Pd $3d_{3/2}$,

respectively. Section 4.3.1.2 showed that these values are either almost in agreement or in good agreement with literature [40], further described in Section 4.3.1.2. The plasmon loss peaks are too small compared to noise level at Pt90, thus difficult to fit.

Interestingly, four new peaks appear in the XPS spectra for the alloys oxidized at 900 ℃ compared to the spectra for cleaned 1 and cleaned 2. Their binding energies are 336.7 ± 0.2 eV, 342.1 ± 0.1 eV, 339.4 ± 0.5 eV, and 344.9 ± 0.6 eV. The two first binding energies are attributed to PdO $3d_{5/2}$ and PdO $3d_{3/2}$, respectively. According to Otto *et al.* [38], which found the PdO $3d_{5/2}$ value at 336.7 eV, this value is in perfect agreement with literature. However, PdO $3d_{3/2}$ was found at 342.5 eV by Militello *et al.* [39], which is almost in good agreement with our value. They only appear for Pt0.5, the most Pd rich alloy. The two last binding energies are attributed to shake-up satellite peaks originating from PdO $3d_{5/2}$ and PdO $3d_{3/2}$, respectively, thus they also only appear for Pt0.5. Militello *et al.* [39] found the satellites at 339.8 eV and 345.5 eV, which is in good agreement with our values.

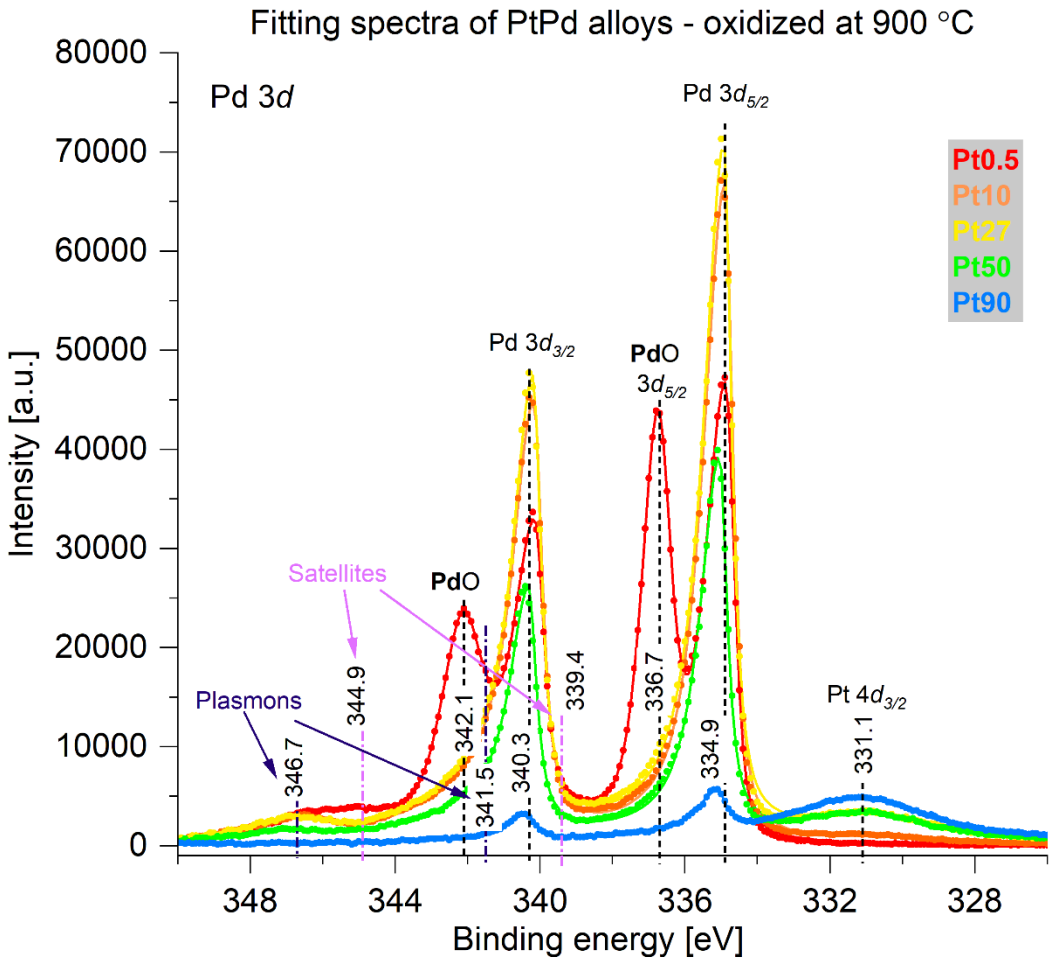

Figure 4.18: XPS spectra of Pd 3*d* for the five Pt_xPd_{100-x} ($x = \{0.5, 10, 27, 50, 90\}$) alloys oxidized at 900 °C. The scattered plots labelled "r" in the legend represents the raw data, and the line plots labelled "t" represents the total fit.

4.3.2.3 O 1s

The O 1*s* spectra of the Pt_xPd_{100-x} ($x = \{0.5, 10, 27, 50, 90, 100\}$) samples oxidized at 900 °C are shown in Figure 4.19 below, using the binding energy range from 510 and 545 eV. In total, seven peaks are identified in this selected area. The most intense peak is located at 532.0 ± 0.2 eV and is attributed to Pd $3p_{3/2}$ metal, see Section 4.3.1.2 for literature reference. Notably, the Pd $3p_{1/2}$ metal peak of this doublet is located outside of the chosen binding energy range, however, the value is given in Table 4.1. The second most intense peak is new and found at 530.1 ± 0.1 eV. It is assigned

to the O 1*s* species of PdO oxide. According to Kibis *et al.* [37] and Banse *et al.* [42], our value is exactly in between their values, found to be 529.9 eV and 530.3 eV, respectively. Generally, the O species for PdO and PtO may overlap in energy, however according to Parkinson *et al.* [32], the binding energy for PtO is at least 0.2 eV larger, see Table 1.1, and Figure 4.17 has no indication of a PtO peak formed at 900 ℃ for all six samples. Therefore, the O species peak is most likely solely originating from formation of PdO.

A third and new peak is located very closely to the O 1*s* species PdO peak, with a binding energy of 529.8 ± 0.4 eV. It is assigned to chemisorbed oxygen, O_{chem}, on Pt and appears for Pt27 and higher Pt content samples. Miller *et al.* [31] reports chemisorbed O on Pt at 529.7 eV, which is in good agreement with our value. However, there was not found any peak at the expected literary binding energy of the Pt $4f_{7/2}$ contribution to O on Pt [31,32] and neither for the Pd $3d_{5/2}$ contribution for O on Pd [36]. On the other hand, the chemisorbed oxygen peak can overlap with Pt $4f_{7/2}$ metal or Pd $3d_{5/2}$ metal or the Pd $3d_{5/2}$ contribution of the surface oxide Pd_5O_4. According to Table 1.1, the species could be fitted to the surface 2D Pd oxide, Pd_5O_4, however, there was no indication of this species in the Pd 3*d* core level spectra. The energy difference between Pd metal and O on Pd is around 0.8 eV according to literature [34,36]. Thus, it is most likely that the oxygen is chemisorbed to Pt, which is furthermore likely due to the energy difference between Pt metal and O on Pt is 0.4 – 0.0 eV.

The fourth peak is located at 533.9 ± 0.1 eV and is attributed to the Pd $3p_{3/2}$ species of PdO. Smirnov *et al.* [43] reports this species at 533.8 eV, which is in good agreement with our literature. The Pd $3p_{1/2}$ contribution is located outside of the chosen binding energy range, see Table 4.1 for found value. The oxide peak decreases with decreasing Pd content in the samples. The fifth peak is found at 519.2 ± 0.5 eV and assigned to Pt $4p_{3/2}$ metal, in good agreement with literature [41]. The sixth peak found in this area is located at 538.0 ± 0.6 eV and assigned as plasmon loss peak Pd $3p_{3/2}$. This peak only forms for higher Pd content samples. The other plasmon loss peak originating from Pd $3p_{1/2}$ is located beyond the selected area, see Table 4.1. They are relatively in good agreement with literature, as seen in Section 4.3.1.3. Lastly, the seventh peak was found at 530.8 ± 0.1 eV. Interestingly, it only appears for Pt90 and Pt100. It is hypothesized to originate from metal-OH, specifically Pt, as it appears for only the highest Pt content samples. This peak

has a shoulder on the lower binding energy side that is within the margin for chemisorbed oxygen, even if it looks like a different species.

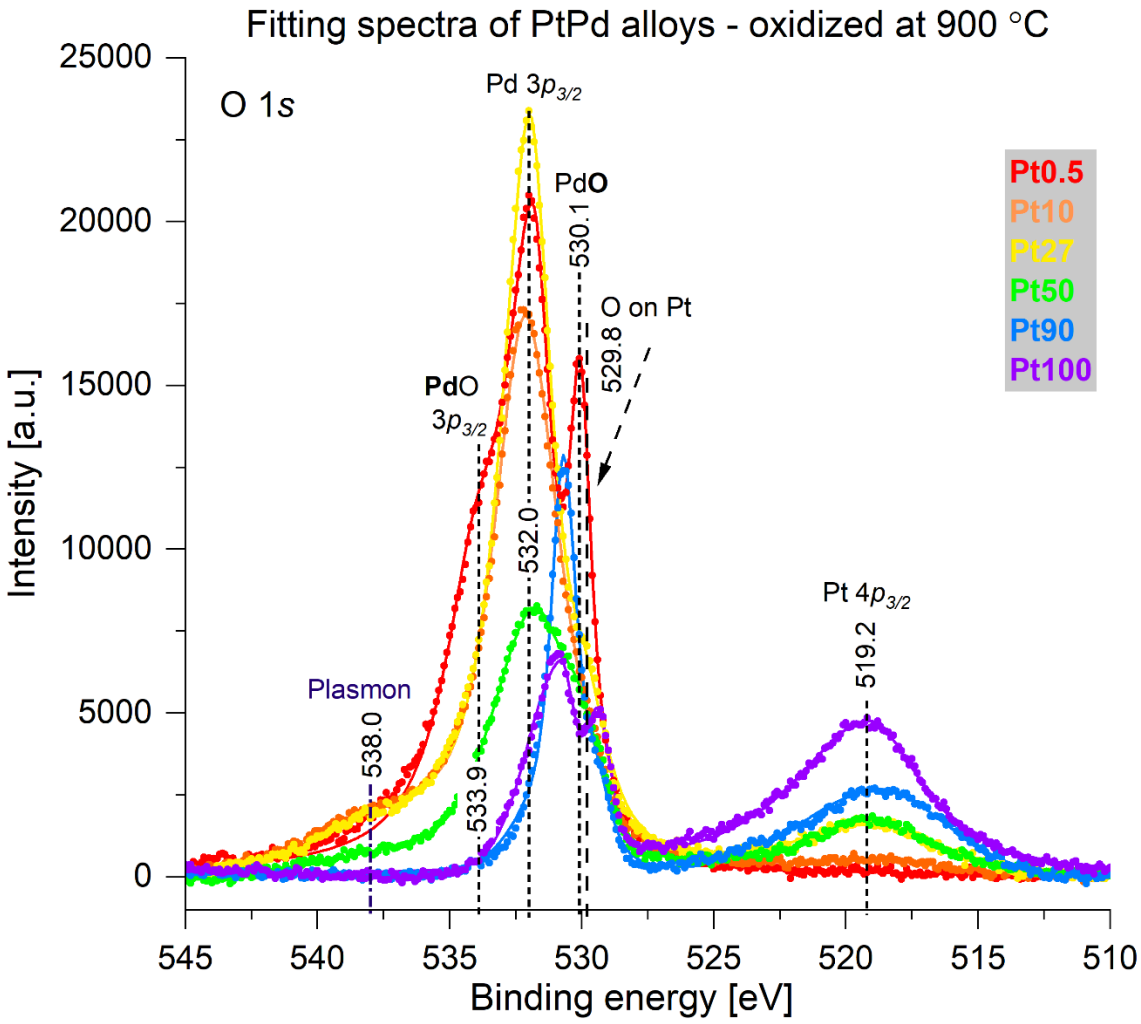

Figure 4.19: XPS spectra of O 1*s* for the Pt_xPd_{100-x} ($x = \{0.5, 10, 27, 50, 90, 100\}$) samples oxidized at 900 °C. The scattered plots labelled "r" in the legend represents the raw data, and the line plots labelled "t" represents the total fit.

4.3.2.4 Conclusion

After oxidation at 900 °C, only Pt0.5 forms any oxide, specifically PdO. Additionally, Pt0.5 forms almost the same amount of PdO as the amount Pd metal is retained. All other samples, Pt_xPd_{100-x}

($x = \{10, 27, 50, 90, 100\}$), do not form any oxides, however, O_{chem} on Pt is formed for Pt27 and higher Pt content samples.

4.3.3 Pt_xPd_{100-x} samples after oxidation at 500 °C

The last sample treatment step of the six Pt_xPd_{100-x} ($x = \{0.5, 10, 27, 50, 90, 100\}$) samples was oxidation at 500 °C. This treatment was chosen as it has more relevance to temperature conditions applicable to our STM equipment and experiments our research group have done at synchrotron beamlines dedicated to NAP XPS. Furthermore, the treatment was also chosen to understand the effect of oxidation of a PtPd catalyst for the Pt catchment process.

In the following sections the Pt 4*f*, Pd 3*d*, and O 1*s* core levels are presented individually.

4.3.3.1 Pt 4f

Figure 4.20 shows the raw Pt 4*f* spectra of the six Pt_xPd_{100-x} ($x = \{0.5, 10, 27, 50, 90, 100\}$) samples, with their corresponding total fits after oxidation at 500 °C. Three Pt $4f_{7/2}$ core level peaks were identified: at 70.8 ± 0.2 eV, 71.8 ± 0.1 eV, and 73.7 ± 0.1 eV. In line with Parkinson *et al.* [32], the two new species at higher binding energies are attributed to PtO and PtO_2, respectively. However, Parkinson *et al.* reports these binding energies at 72.3 eV and 74.1 eV, respectively. Similarly as in Section 4.3.1.1, the values are roughly 0.5 eV higher than what is found in this thesis, thus the consistent shifts in binding energies for the species suggests that our values are in good agreement with literature. By inspecting Figure 4.20 carefully, PtO_2 is better visible in the Pt $4f_{5/2}$ component of the doublet, where it is not obscured by other contributions. Only higher Pt content samples, Pt50 and Pt90, form PtO_2 during oxidation at this temperature. The fit shows that with higher Pt content samples, less PtO is formed. In fact, only Pt100 does not form any oxide, neither PtO nor PtO_2. Therefore, less of either oxide is formed relative to amount of Pt metal retained for higher Pt content alloys. A simple inspection of Figure 4.20 suggests that the quantity of oxide formed relies on the alloy composition, with the Pt27 alloy having the highest amount of oxide formed.

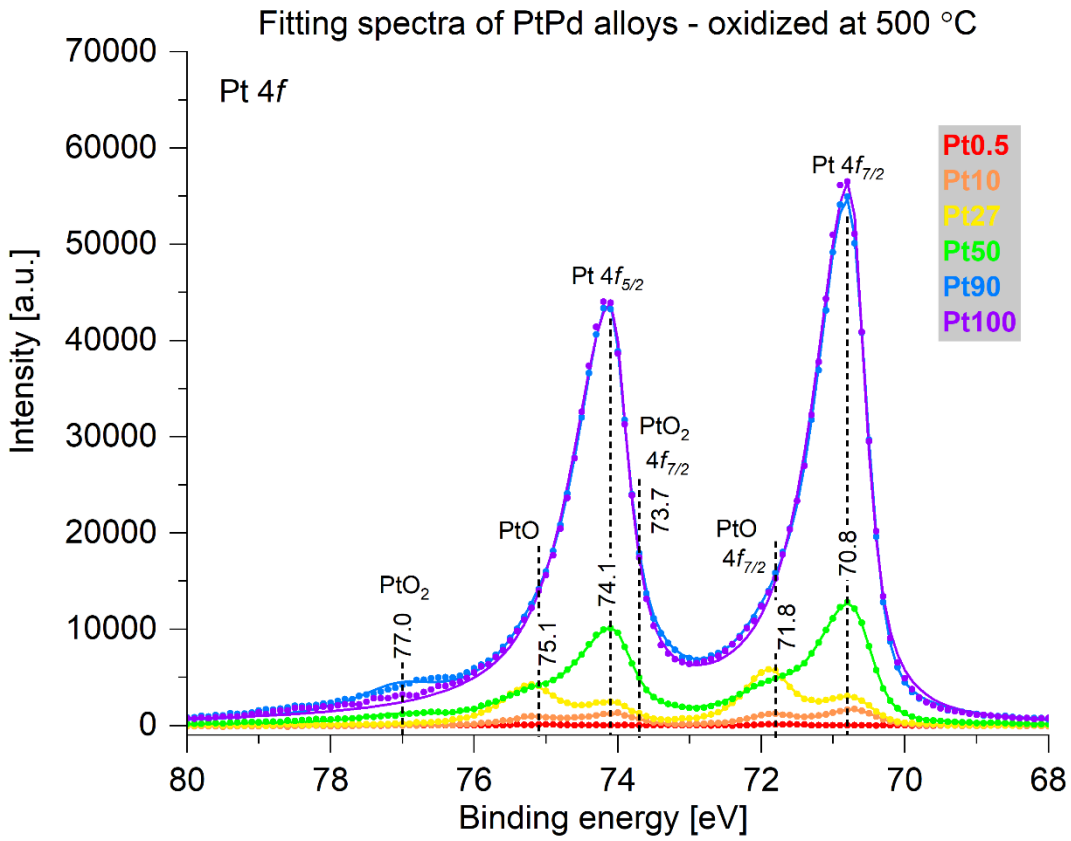

Figure 4.20: XPS spectra of the Pt 4f core level for the six Pt_xPd_{100-x} ($x = \{0.5, 10, 27, 50, 90, 100\}$) samples after oxidation at 500 °C. The scattered plots labelled "r" in the legend represents the raw data, and the line plots labelled "t" represents the total fit.

In order to elaborate on the quantity of oxide formed on the various alloy surfaces in comparison with the metal components, all alloys, except Pt0.5, were normalized. Normalizing a XPS spectrum entails to choose a point in the middle between a chosen metal and oxide component and normalize all the spectra through this point. For instance, for Figure 4.21 this point was chosen to be the middle of Pt $4f_{7/2}$ metal and oxide component for Pt27. The normalized spectra for all samples, except Pt0.5, are shown in Figure 4.21. The Pt0.5 sample is not included because Pt0.5 has a low signal to noise ratio, which obscures the other spectrum when scaled. In comparison with Figure 4.20, the normalized spectra better visualize the increased PtO proportion compared to Pt metal in the samples. Through careful inspection of the spectra, it becomes clear that Pt27 sample forms the most oxide relative to Pt metal. The spectrum for Pt10 also show that this sample

has a significantly higher PtO proportion relative to Pt metal than most samples, though not as large as for Pt27.

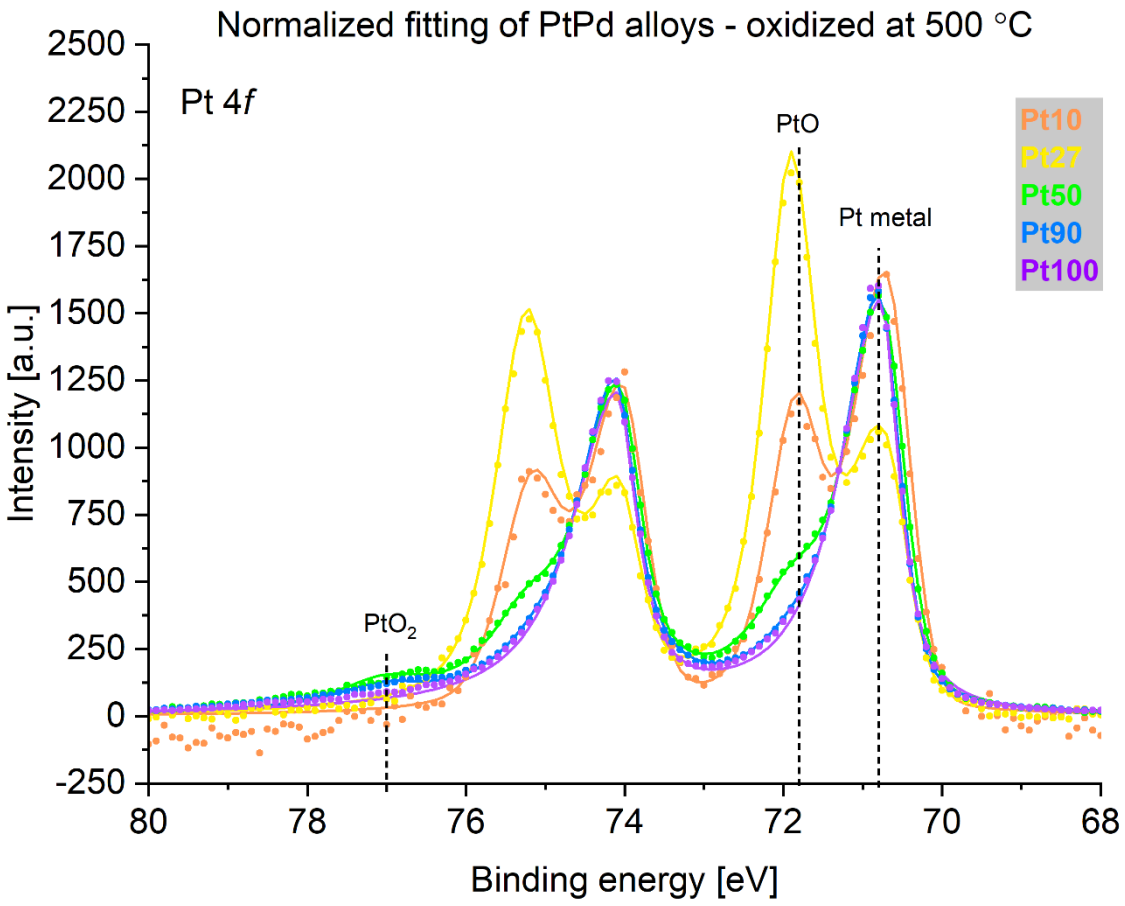

Figure 4.21: XPS spectra of the normalized raw data and corresponding fitting of the spectra shown in Figure 4.20 for the five Pt_xPd_{100-x} ($x = \{10, 27, 50, 90, 100\}$) samples after oxidation at 500 °C. The normalization procedure is explained above. The Pt0.5 spectrum is excluded because it has a too high noise to signal ratio, and therefore muffles the other spectra. The scattered plots labelled "r" in the legend represents the raw data, and the line plots labelled "t" represents the total fit.

Figure 4.22 below includes the deconvoluted fits for all found species in the Pt 4*f* core level for the five Pt_xPd_{100-x} ($x = \{0.5, 27, 50, 90, 100\}$) samples. They were chosen as they show the range

of observed fitted components observed after the oxidation. Based on the only Pt component in the spectrum at 71.7 eV, assigned to PtO, all Pt in the alloy forms PtO. The sample Pt0.5 was found to only have one contribution, namely PtO. Therefore, Pt0.5 converts all Pt metal to PtO after the oxidation. Pt100, on the other hand, does not form any oxide at all and only consists of Pt metal. All the five other samples form PtO in varying degrees. Pt27 and Pt50 form both PtO and Pt metal, although Pt27 forms more PtO compared to Pt metal, whereas Pt50 forms more Pt metal relative to the oxides. Lastly, as mentioned earlier, Pt50 and Pt90 are the only two samples that form PtO_2.

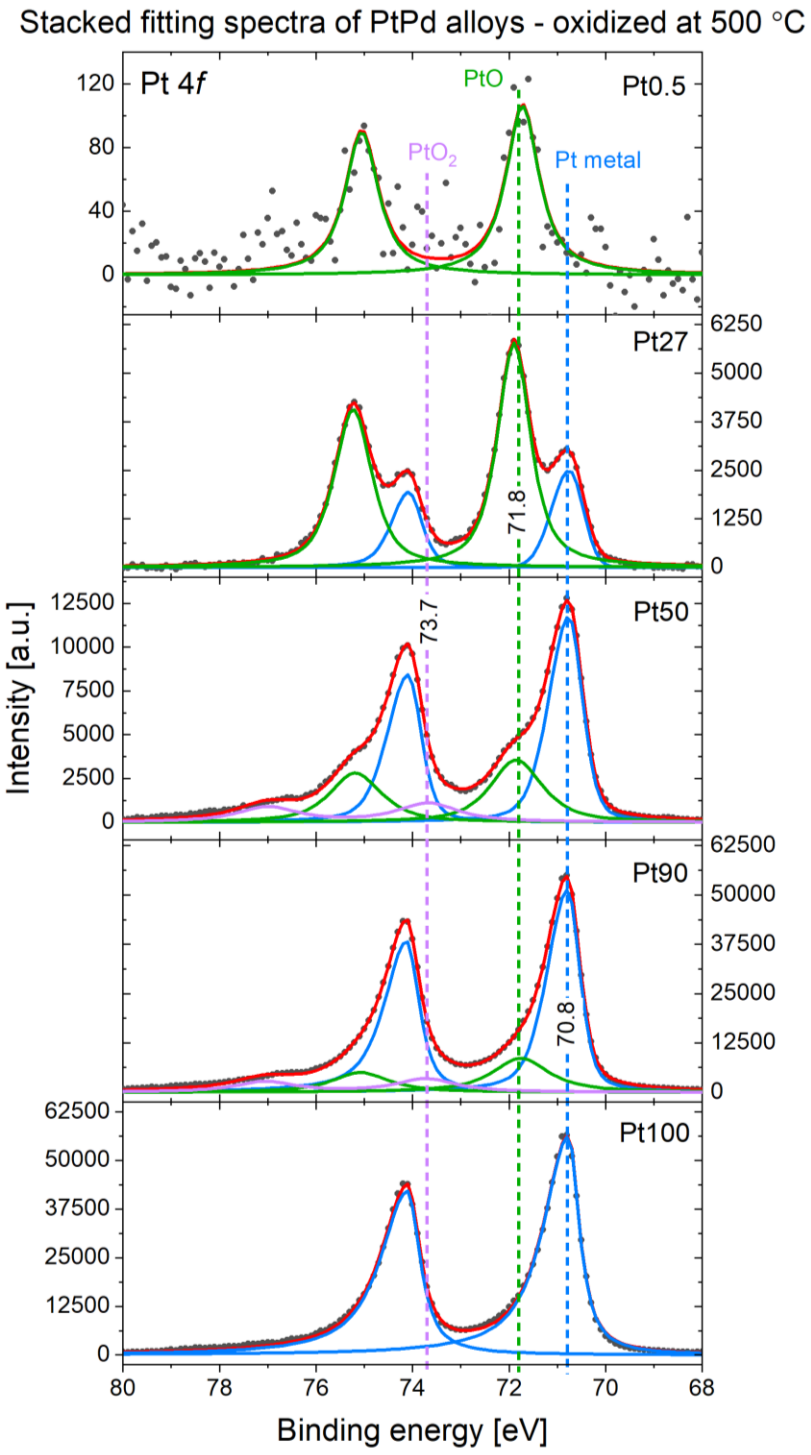

Figure 4.22: XPS spectra of the deconvoluted fits for the Pt 4*f* core level for the five Pt_xPd_{100-x} ($x = \{0.5, 27, 50, 90, 100\}$) samples after oxidation at 500 °C. Dashed lines indicate the binding energy for Pt $4f_{7/2}$ for three species: Pt metal (blue), PtO (green), and PtO_2 (pink). Dark grey dots are the raw data and red lines are the total fits. The intensities are not comparable between the spectra.

4.3.3.2 Pd 3d

The XPS spectra of raw data and fitted curves of the Pd 3*d* core level for the five Pt_xPd_{100-x} ($x = \{0.5, 10, 27, 50, 90\}$) alloys after oxidation at 500 °C are shown in Figure 4.23 below. The two most intense peaks were found for the Pd $3d_{5/2}$ core level at; 334.9 ± 0.2 eV, and 336.7 ± 0.2 eV, attributed to Pd metal and PdO, respectively. In Section 4.3.1.2, it was found that according to literature [34,38] these values are in perfect agreement with our values. PdO is formed for all five alloys. In addition, three other binding energies were found at 331.2 ± 0.1 eV, 339.4 ± 0.5 eV, and 344.9 ± 0.6 eV. The first binding energy is attributed to Pt $4d_{3/2}$ metal, which shown in Section 4.3.1.2 is in perfect agreement with literature [33]. The two last are attributed to shake-up satellites formed because of the oxidation, more accurately for Pd $3d_{5/2}$ and Pd $3d_{3/2}$, respectively. These values were found to be in good agreement with literature [39] in Section 4.3.2.2. Neither binding energies corresponding to plasmon peaks, nor PdO_2 peaks were found.

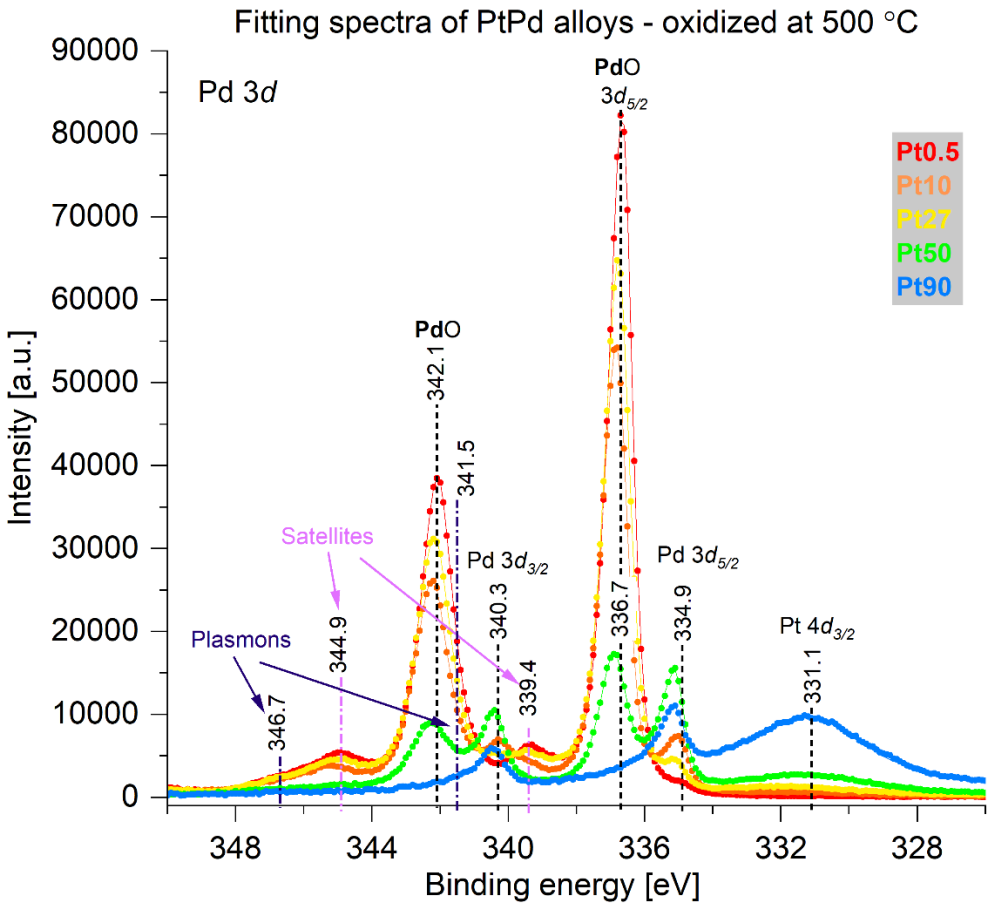

Figure 4.23: XPS spectra of raw data and fitted curves for the Pd 3*d* core level of the five Pt_xPd_{100-x} ($x = \{0.5, 10, 27, 50, 90\}$) alloys after oxidation at 500 °C. The scattered plots labelled "r" in the legend represents the raw data, and the line plots labelled "t" represents the total fit.

The three samples with highest Pd content, namely Pt0.5, Pt10, and Pt27, forms almost solely PdO, as seen by Figure 4.23. This is supported by normalizing the data, illustrated in Figure 4.24. The normalization procedure is further explained in Section 4.3.3.1. These three samples form almost the same amount of PdO relative to Pd metal. As a result of this, the shake-up satellite peaks for PdO mostly forms for these higher Pd content samples. PdO is formed for all five alloys. Only very small amounts of the satellites are formed on the three other samples. As expected, the Pt 4*d* peak increase with Pt content in the alloys.

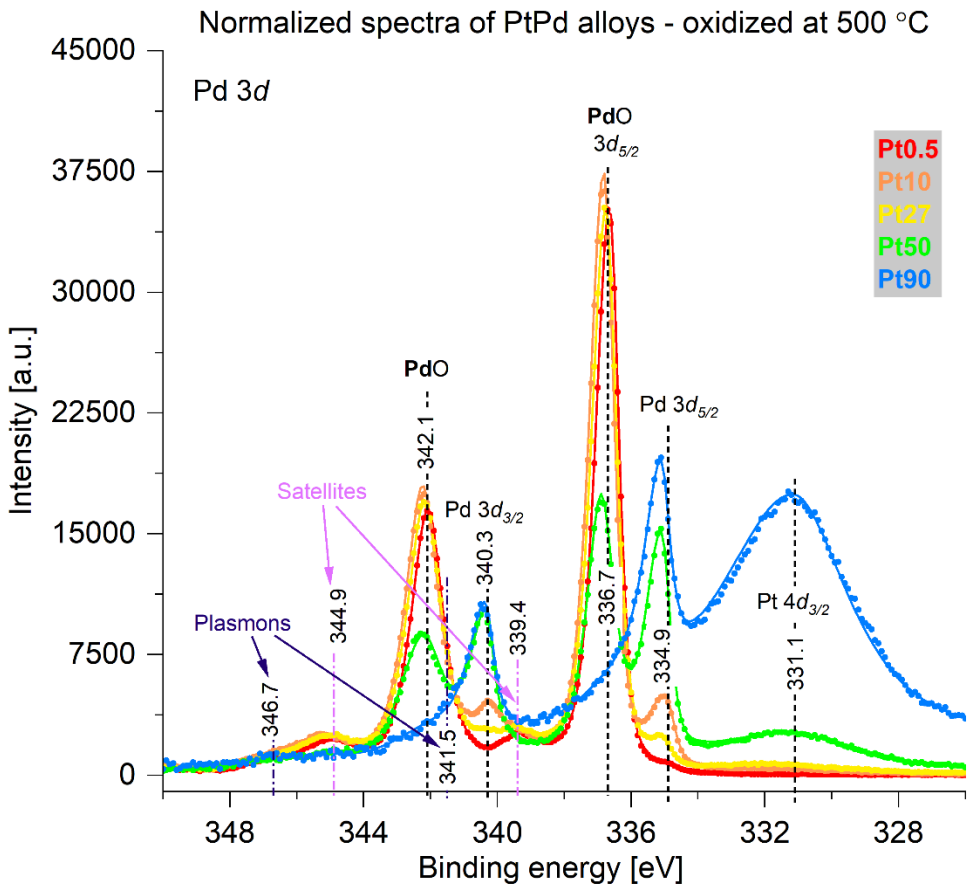

Figure 4.24: XPS spectra of the normalized fit of the raw data and fitted curves shown in Figure 4.23 for the five Pt_xPd_{100-x} ($x = \{0.5, 10, 27, 50, 90\}$) alloys after oxidation at 500 °C. The normalization procedure is further explained in section 4.3.3.1. The data was normalized to easily facilitate the comparison of the relative contributions of Pd oxides more easily for the Pt0.5 to Pt100 alloys. The scattered plots labelled "r" in the legend represents the raw data, and the line plots labelled "t" represents the total fit.

Figure 4.25 is a stacked image showing all fits of the three Pt_xPd_{100-x} ($x = \{0.5, 27, 90\}$) alloys. From this image, the sample Pt0.5 is observed to form exclusively PdO, in addition to satellites stemming from the oxide. As for Pt 4*f*, this is therefore also an extreme of the samples. Pt27 also form a lot of oxide, but a little amount of Pd metal remains unoxidized. The satellites are formed in a similar relative amount. Pt27 additionally form Pt 4*d* metal, though only a very small amount. Pt90 is the sample with the highest Pd content. As shown in both previous spectra, this sample has the least formation of PdO and the most Pd metal remained after oxidation. As a result of small oxide content, the satellite peaks are scarcely formed.

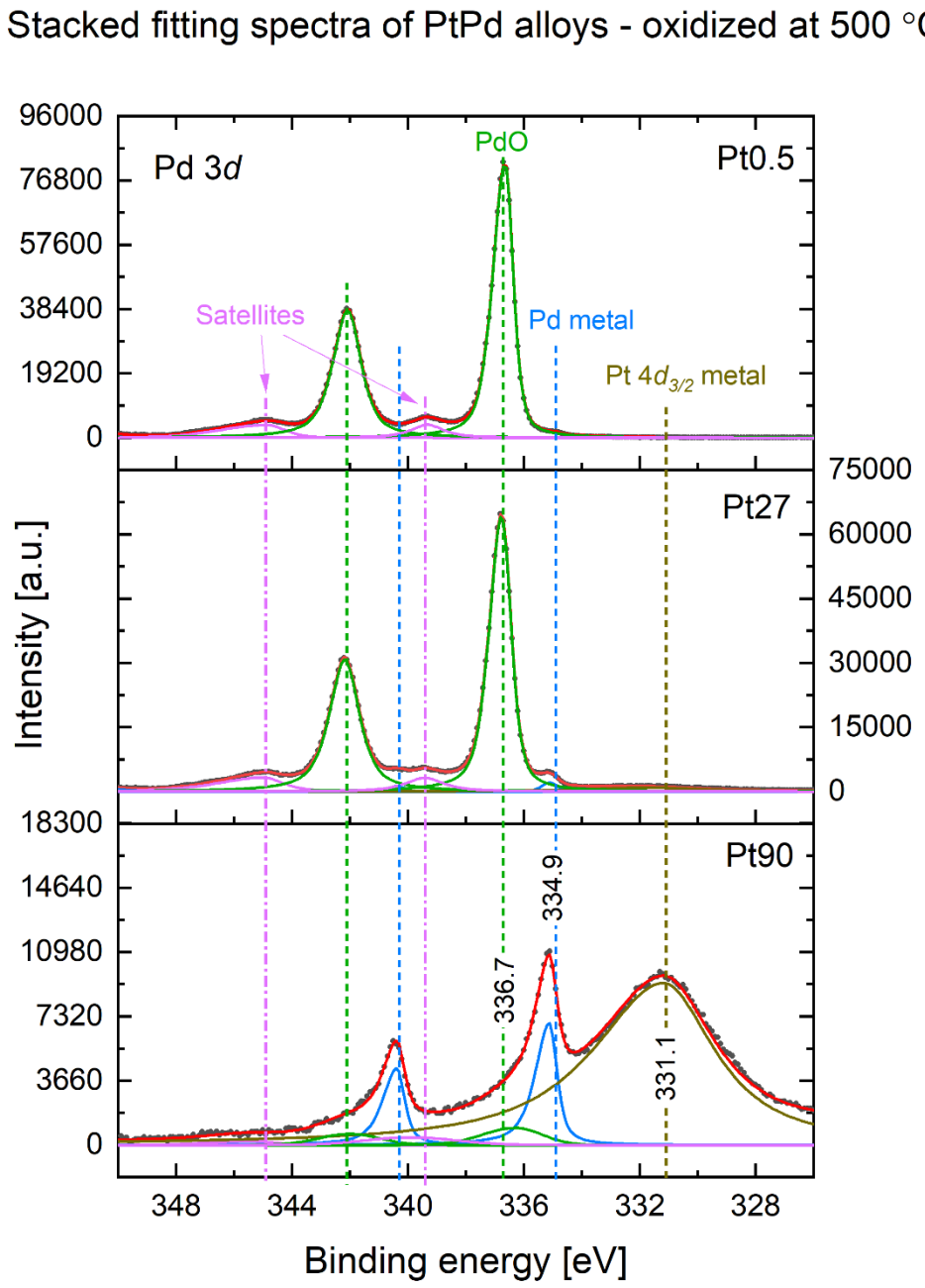

Figure 4.25: The XPS spectra of the deconvoluted Pd 3*d* core level fits for the three Pt_xPd_{100-x} ($x = \{0.5, 27, 90\}$) alloys after oxidation at 500 °C. Dashed lines represent the binding energy for Pd $3d_{5/2}$ for two species: Pt metal (blue), and PtO (green), and additionally for Pt $4d_{3/2}$ metal (dark yellow) and shake-up satellites for PdO (pink). Dark grey spheres are the raw data and red lines are the total fits. The intensities are not comparable between the spectra.

4.3.3.3 O 1s

Fitting of the Pt_xPd_{100-x} ($x = \{0.5, 10, 27, 50, 90, 100\}$) samples showed six distinguishable contributions between 512 eV and 545 eV after oxidation at 500 °C, shown in Figure 4.26 below. The two most intense peaks are located at 530.1 ± 0.1 eV and 529.8 ± 0.4 eV, which are attributed to the oxygen species of PdO/PtO oxides and chemisorbed O on Pt, respectively. In Section 4.3.2.3, these were found to be in good agreement with literature [31,37,42]. Contrary to the samples after oxidation at 900 °C, see Section 4.3.2.3, both PtO and PdO are formed after oxidation at 500 °C. Thus, the O species resulting from oxide formation is now a combination of the O species from both PdO and PtO. This may explain the apparent shifts in binding energy for the peak in Figure 4.26, especially visible for Pt50. The close proximity of the peaks poses a little challenge, however, the difference in their full width at half maximum (FWHM) aids during the fitting, namely because the oxide peak is very narrow, about 1 eV, while the chemisorbed O peak is broader at around 2 eV. The peak for the O species of PdO/PtO only forms at samples with higher Pd content, namely Pt50 and below, while the chemisorbed peak forms at lower Pd content, from Pt50 and above. The third and fourth peaks in this region were found at 532.0 ± 0.2 eV and 533.9 ± 0.1 eV and were attributed to Pd $3p_{3/2}$ metal and the Pd $3p_{3/2}$ species of PdO. Both peaks are in good agreement with literature [43], as explained further in Sections 4.3.1.3 and 4.3.2.3. The fifth peak at 543.8 ± 0.2 eV is due to a shake-up satellite peak originating from PdO Pd $3p_{3/2}$, see Section 4.3.2.3 for literature reference. The sixth peak at 519.2 ± 0.5 eV originates from Pt $4p_{3/2}$ metal, see Section 4.3.1.3 for literature reference.

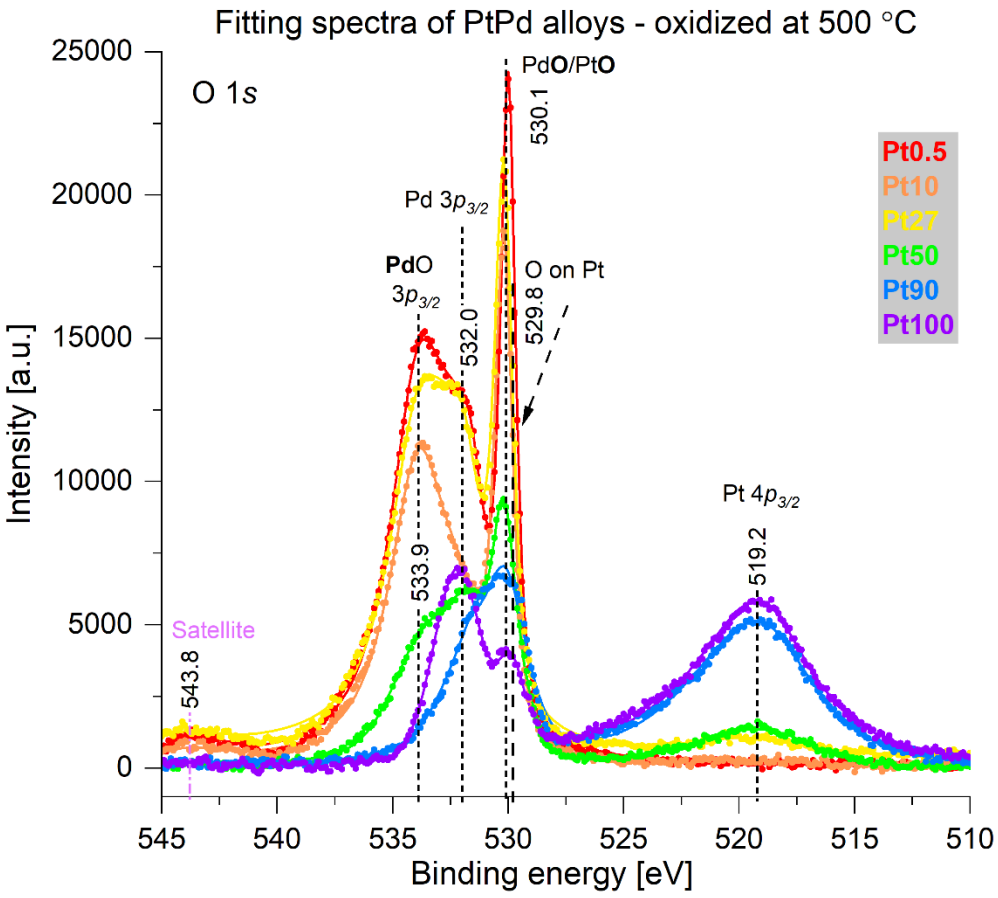

Figure 4.26: XPS spectra of O 1s core level of the Pt_xPd_{100-x} ($x = \{0.5, 10, 27, 50, 90, 100\}$) samples after oxidation at 500 °C. The scattered plots labelled "r" in the legend represents the raw data, and the line plots labelled "t" represents the total fit.

A comparison of the O 1*s* core level deconvoluted fit of the four Pt_xPd_{100-x} ($x = \{0.5, 27, 90, 100\}$) samples after oxidization at 500 °C is shown in Figure 4.27 below. With decreasing Pd content, PdO is formed less. Most interestingly, as noted above, with decreasing Pd content (i.e., enrichment with Pt), the PtO and PdO oxide contribution diminishes in favour of chemisorbed O on Pt. For the Pt100 sample, all Pd-related peaks are absent, and instead the seventh peak at 532.2 ± 0.1 eV appears, as noted above. This peak is not present in the spectra of other alloyed samples.

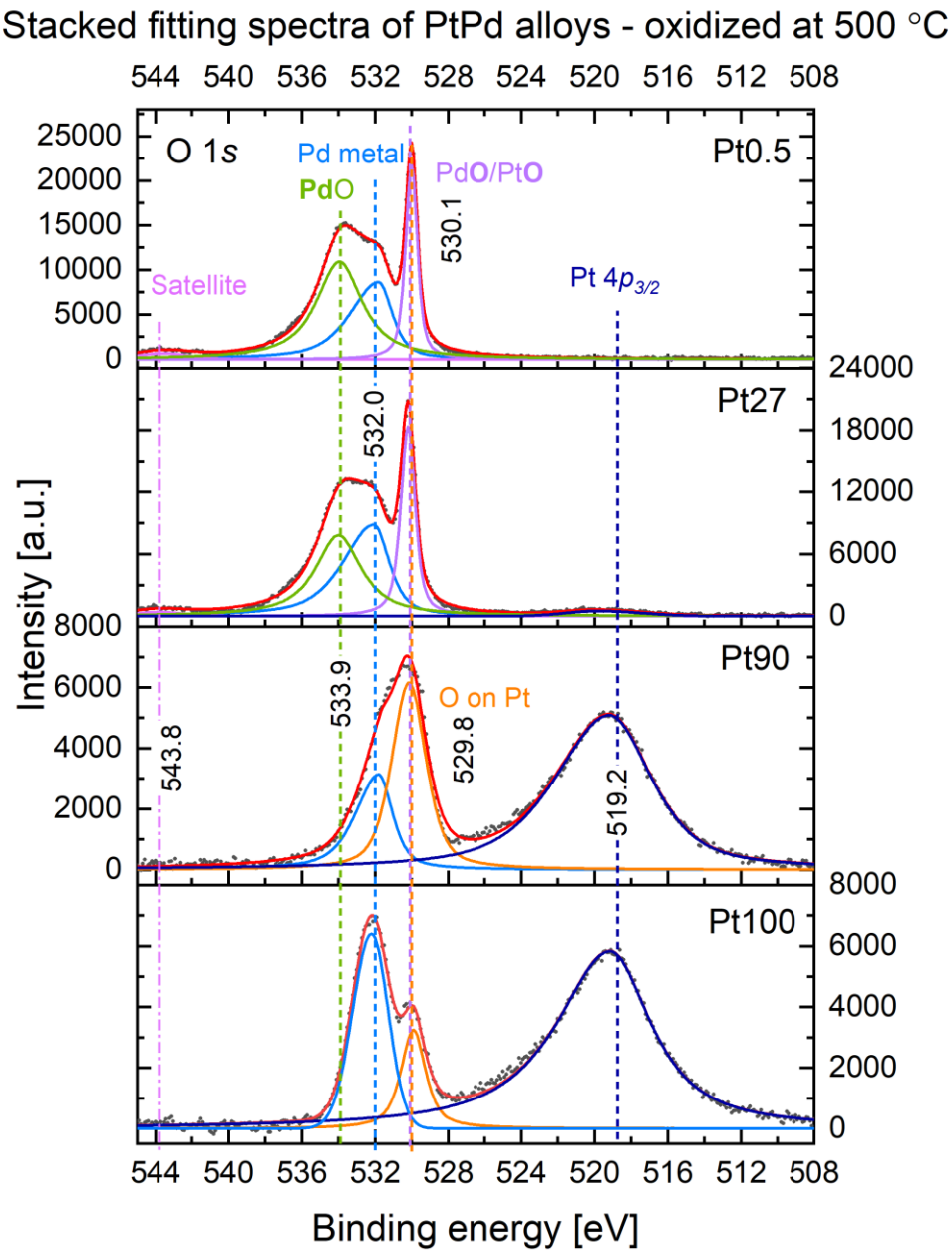

Figure 4.27: XPS spectra of O 1*s* core level of raw data and fitted curves after oxidation at 500 °C for the four Pt_xPd_{100-x} ($x = \{0.5, 27, 90, 100\}$) samples. Dashed lines represent the binding energy for Pd $3p_{3/2}$ for two species: Pd metal (blue) and PdO (green). Two dashed lines represent O 1*s* for the species PdO/PtO (purple) and chemisorbed O (orange). Additional dashed lines represent Pt $4p_{3/2}$ metal (dark blue) and shake-up satellite for PdO (pink). Dark grey spheres are the raw data and red lines are the total fits. The intensities are not comparable between the spectra.

4.3.3.4 Conclusion

The samples were expected to be vastly different after oxidation at 500 ℃ compared to oxidation at 900 ℃. From the phase diagram of the binary Pd-Pt in Figure 1.3, the samples were expected to undergo phase segregation to (Pd) + (Pt). Furthermore, the temperature used for oxidation which results in oxide formation, is commonly around 500 ℃ and below, as can be seen in Table 1.1, thus expecting oxides to form at a much larger extent. One of the most notable discoveries is that oxidation at 500 ℃ lead to formation of both PtO and PtO_2, whereas oxidation at 900 ℃ resulted in zero Pt-oxides formed. Additionally, oxidation at 500 ℃ lead to a high amount of PdO formed, both in comparison with amount of Pd metal and the amount formed after oxidation at 900 ℃, where only PdO was formed, and was furthermore only formed for Pt0.5. PdO is formed for all five alloys. Overall, oxidation at 500 ℃ results in formation of three types of oxides: PtO, PtO_2, and PdO, as well as formation of chemisorbed oxygen on Pt, O_{chem}, for Pt50 and higher Pt content samples.

4.3.4 Overview of the XPS analysis of Pt_xPd_{100-x} samples

The overview of found binding energies and their attributed species is presented in Table 4.1 below. Additionally, all literature references used to appropriately assign the species is written in an accompanying column.

Table 4.1: Overview of species identified in the XPS spectra of bare and oxidized Pt_xPd_{100-x} ($x = \{0.5, 10, 27, 50, 90, 100\}$). The overview is based on the findings described in Sections 4.3.1, 4.3.2, and 4.3.3.

Core level	*Binding energy [eV]*	*Assignment*	*Comments*	*Reference*
Pt 4*f*	70.8 ± 0.2	Pt $4f_{7/2}$ metal	Surface and bulk combined	[30,31]
	71.8 ± 0.1	PtO	Parkinson *et al.* [32] reports it around 0.5 eV higher, but all our relevant species are roughly 0.5 eV lower than their respective species	[32]
	73.7 ± 0.1	PtO_2	Parkinson *et al.* [32] reports it around 0.5 eV higher, but all our relevant species are roughly 0.5 eV lower than their respective species	[32]
	74.1 ± 0.3	Pt $4f_{5/2}$ metal	Surface and bulk combined	[30,31]
	75.1 ± 0.1	PtO $4f_{5/2}$		[72]
	77.0 ± 0.25	PtO_2 $4f_{5/2}$		[72]
Pt 4*d*	314.1 ± 1.0	Pt $4d_{5/2}$ metal and oxidized		[33]
	331.1 ± 1.0	Pt $4d_{3/2}$ metal and oxidized		[33]
Pd 3*d*	334.9 ± 0.2	Pd $3d_{5/2}$ metal	Surface and bulk combined	[34]
	336.7 ± 0.2	PdO $3d_{5/2}$		[38]
	339.4 ± 0.5	Shake-up satellite peak Pd $3d_{5/2}$	Result of PdO formation, thus appears for samples with oxides	[39]
	340.3 ± 0.2	Pd $3d_{3/2}$ metal	Surface and bulk combined	[34]

	341.5 ± 0.5	Plasmon loss peak Pd 3$d_{5/2}$	Result of Pd metal, thus appears for high Pd metal content samples	[40]
	342.1 ± 0.1	PdO 3$d_{3/2}$		[38,39]
	344.9 ± 0.6	Shake-up satellite peak Pd 3$d_{3/2}$	Result of PdO formation, thus appears for samples with oxides	[39]
	346.7 ± 0.4	Plasmon loss peak Pd 3$d_{3/2}$	Result of Pd metal, thus appears for high Pd metal content samples	[40]
Pt 4*p*	519.2 ± 0.5	Pt 4$p_{3/2}$ metal	Surface and bulk combined	[41]
O 1*s*	529.8 ± 0.4	O_{chem}	On Pt	[31]
	530.1 ± 0.1	PdO/PtO	After oxidation at 900 ℃, PdO is the only contribution. After oxidation at 500 ℃, both PdO and PtO appear and contribute.	[32,37,42]
Pd 3*p*	532.0 ± 0.2	Pd 3$p_{3/2}$ metal	Surface and bulk combined	[43]
	533.9 ± 0.1	PdO 3$p_{3/2}$		[43]
	538.0 ± 0.6	Plasmon loss peak Pd 3$p_{3/2}$	Result of Pd metal, thus appears for high Pd metal content samples	[40]
	543.8 ± 0.1	Shake-up satellite peak Pd 3$p_{3/2}$	Result of PdO formation, thus appears for samples with oxides	[39]
	559.8 ± 0.2	Pd 3$p_{1/2}$ metal	Surface and bulk combined	[40]
	561.6 ± 0.2	PdO 3$p_{1/2}$	Reported at 562.1 eV, slightly out of the found range for our value	[39]

	565.5 ± 0.8	Plasmon loss peak Pd $3p_{1/2}$	Result of Pd metal, thus appears for high Pd metal content samples	[40]
	571.4 ± 0.3	Shake-up satellite peak Pd $3p_{1/2}$	Result of PdO formation, thus appears for samples with oxides	[39]

5 Discussion

In this thesis, a focus was placed on surface science studies of PtRh samples with relevance to the ammonia oxidation reaction, as described in Section 1.3, and PtPd samples used in the Pt catchment process, as described in Section 1.4.

5.1 Expansion of the PtRh roadmap to high coverage surfaces

For better understanding of PtRh alloying, the previous roadmap provided by Pettersen *et al.* [27] needed to be expanded for surfaces with high coverage, see Figure 1.9. Pettersen [25] explored only high coverage surfaces for the Pt/Rh(111) system, see Figure 1.7, which inspired us to compliment, compare, and contrast the roadmap with behaviour of high coverage Rh/Pt(111) surfaces.

5.1.1 Previous reported PtRh surfaces at UiO

Three roadmaps describe preparation and oxidation of PtRh samples on either a Pt(111) surface or Rh(111), see Figure 1.5, Figure 1.6, and Figure 1.9 in the Introduction [24–27]. In short, we recap key features from these studies.

The morphology and mixing vary substantially depending on two main parameters: surface temperature and coverage. In line with first principles modelling, Pettersen *et al.* [27] found through experiments using an STM, that when mixing Pt and Rh, Pt prefers surface location and Rh tends to go subsurface at UHV conditions. To promote good mixing of a surface or near-surface alloy (NSA), high temperature is necessary, either during the metal deposition or during subsequent post annealing (PA).

Pettersen *et al.* presents two reconstructions found on Pt/Rh(111) and Rh/Pt(111), as seen in Figure 1.9, in the temperature range of around 400 – 600 K. The reconstruction formed in the Pt/Rh(111) surface is called *island* reconstruction, because it only forms on Pt islands. On Rh/Pt(111) another reconstruction is formed in the temperature range of 425 K and above, called *network* reconstruction. The network reconstruction is formed on Pt terraces and surrounds the Rh islands, in a seemingly hexagonal mesh, as seen in Figure 1.10 in the Introduction. This figure depicts the network reconstruction as a function of increasing deposition temperature. No discernible periodicity of the structure is observed because the double lines appear as straight lines with rotors (Rc and Rcc), stars (S), and elbows (E), see Figure 1.10.

As mentioned earlier, both the morphology and the mixing are controlled by the coverage. All surfaces reviewed above are low coverage surfaces. The effect of high Rh coverage on a surface morphology and reconstruction of Pt(111) single crystal are explored in the next section.

5.1.2 High coverage Rh/Pt(111) surfaces and the honeycomb structure

The as prepared (AP) high coverage surfaces studied in the current work are presented in Figure 4.2 and Figure 4.3. In comparison with the most recent roadmap presented in Figure 1.9, by Pettersen *et al.* [27], the expected island morphology for the preparation conditions used is triangles. Figure 4.3 show a clear preference for triangle morphology, especially with increasing temperature, in agreement with results by Pettersen *et al.* [27].

Another expected result from previous work, is formation of a network reconstruction in the temperature range of 400 – 500 K, as described by Pettersen *et al.* Interestingly, no indication of this is visible in the surfaces prepared in the current work. The most likely explanation of the absence of the network reconstruction is in the mechanism of which the reconstruction forms. Diffusion of Rh subsurface induces Pt surfaces to reconstruct; and if the coverage of Rh on the surface is too high, the surface will likely be Rh-terminated, thereby preventing the formation.

Zheng *et al.* [24] describes that for Rh/Pt(111) in the *low* coverage regime, some atoms may nucleate on the surface creating small strings in between the islands. If supplied with sufficient thermal energy, the strings of nuclei produce network reconstruction, as seen in Figure 1.9, reported by Pettersen *et al.* [27]. Interestingly, in the case of *high* coverage Rh/Pt(111) a new surface reconstruction was discovered instead, labelled honeycomb reconstruction or honeycomb pattern, due to its striking resemblance to a honeycomb. The reconstruction exhibits high temperature stability and is obtained in a broad range of preparation (AP) and post annealing (PA) conditions, see Figure 4.4 and Figure 4.5. In comparison with the previous found reconstructions on the Rh/Pt(111) surface, the network reconstruction, some resemblance is found. However, the new pattern is highly uniform and periodic, most notably with closed hexagons in a mesh. After comparing the honeycomb pattern with the island reconstruction found on Pt/Rh(111), we note that the latter features periodic rows arranged in domains, oriented along the three crystallographic axes. It exhibits clear short-range periodicity and lacks well-defined long-range order, and thus has no resemblance to the honeycomb pattern. Most interestingly, the new pattern on Rh/Pt(111) forms continuously across both the islands and steps, thereby covering the entire surface.

Some interesting observations about the continuity of the honeycomb pattern were made. For lower AP temperature, the ad-islands are connected to the steps, resulting in a clear continuity of the pattern. At higher AP temperatures, 380 K and higher, the islands become separated from the steps, which results in the surface losing the clear formation of steps and exposing the lower layers of the surface. While the islands have retained the honeycomb pattern, the lower surface layers appear to either form a different reconstruction, bearing some resemblance to the network reconstruction, or form a distorted version of the honeycomb pattern. The reconstruction features long lines in a random pattern and possible line-bending features such as rotors, stars, and elbows, which are further explained and visualized in Section 4.1.4 and Figure 4.4, and appear for the network reconstruction. Considering the lower surface layers appear to have a low coverage of Rh, it is possible that the reconstruction actually is the network reconstruction. Further investigation is essential to confirm the mechanism of this reconstruction. The surface prepared at 450 K, see image **c)** in Figure 4.4, clearly show the reconstruction of the lower surface layers, with the retained honeycomb pattern on the islands, and show no indication of a connection.

The lines formed by nuclei, as shown by Zheng *et al.* in Section 1.6.1, are clearly observable when zooming in Figure 4.4 **c)**. As further presented by Pettersen *et al.* [27], the honeycomb pattern could, similarly to the network reconstruction, be formed due to small nuclei formed along the strain lines of the surface.

In order to understand the nature of the honeycomb structure better, fruitful topics for further studied would be to get better insight into the formation mechanism and the composition of the honeycomb reconstruction. Previous work, [24–27], have shown that higher temperatures promote mixing of Pt and Rh to create PtRh surface and near-surface alloys. The roadmap by Zheng *et al.*, see Figure 1.5, suggests that the preparation temperature range used in this thesis, 350 – 450 K, is not enough to properly mix the two constituent metals as prepared. However, post treatment such as PA to 600 – 700 K promoted elemental mixing. Therefore, it is speculated that the honeycomb pattern appears as a result of well mixing of the metals. It is relevant to mention that in contrast to Pt(111), for which literature and our own results describe the appearance of reconstructions, there is no evidence on how bare Rh surface should reconstruct, neither if such reconstruction has been observed. Our own studies with Rh(111) showed no evidence of surface reconstructions [25].

Furthermore, because the preparation temperature range used in this thesis has been explored previously by Zheng *et al.* after PA at 700 K with low coverage surfaces, it is hypothesized that the high surface coverage is essential to form the honeycomb pattern. Additionally, the AP temperature has seemingly no significant effect on the formation of the honeycomb pattern within 350 – 450 K, as long as the PA temperature is high enough (≥ 600K).

As for the composition of the honeycomb pattern, it is hypothesized that the reconstruction is formed on the exposed Rh layers, both upper and lower, when the Rh coverage is high enough (at least roughly 1.5 ML). The high coverage is essential to have continuity of the pattern across the islands, terraces and steps, as well as to compensate for the Rh that naturally goes subsurface. In order to fully determine the constituents of the honeycomb pattern, an XPS study of the surfaces is highly necessary.

The roadmap presented in Figure 5.1 illustrates the morphology of islands as prepared and the reconstruction covering the surface after post annealing at higher temperatures (600 and 700K). The illustrations are given as a function of as prepared and post annealed temperature (K). the

honeycomb illustrations are based on the surfaces prepared at 350 K and subsequently post annealed at either 600 or 700 K, see Figure 4.5. It is important to note that the roadmap is based on a limited set of experimental data. Experimental information is described in Section 3.1.2. Further experiments are necessary to complete the roadmap and to determine the conditions at which the honeycomb pattern appears and vanishes.

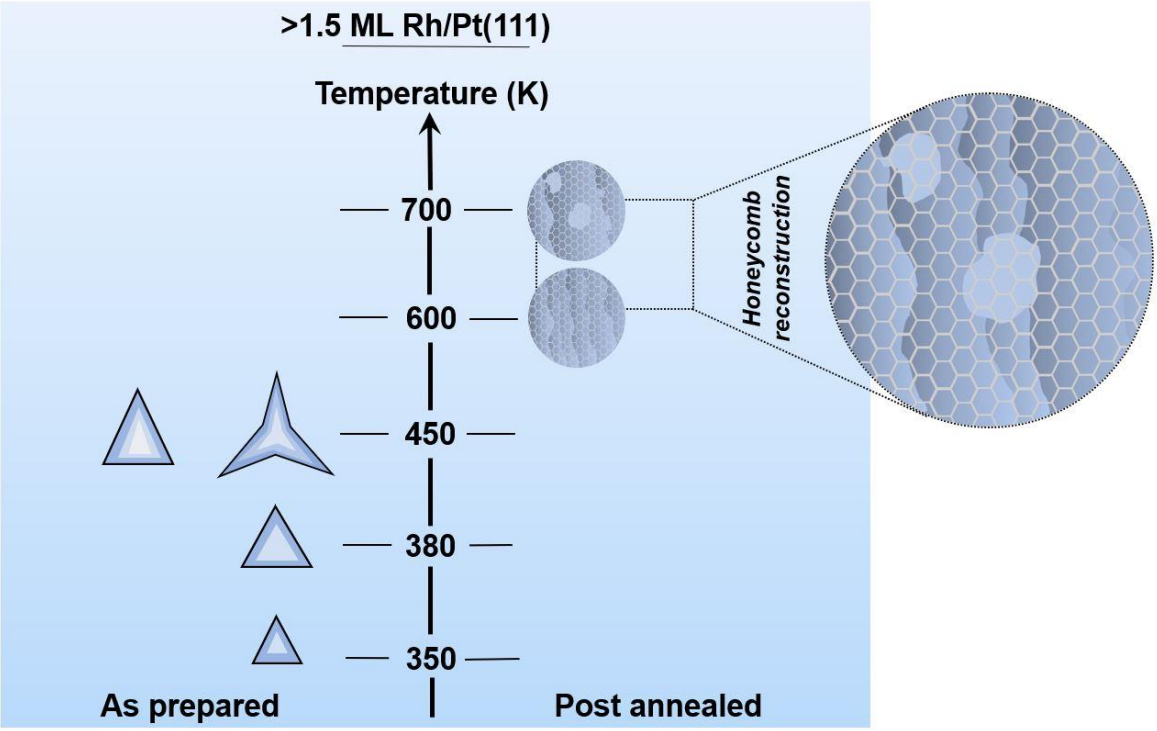

Figure 5.1: Roadmap of morphology as a function of temperature of high coverage as prepared and post annealed Rh/Pt(111) surfaces. The illustrations of the honeycomb reconstruction formed after post annealing at either 600 or 700 K are based on surfaces prepared at 350 K, seen in Figure 4.5.

5.1.3 Oxidation of Rh/Pt(111) surfaces presence of and Moiré pattern

The stability of the reconstructed Rh/Pt(111) surfaces were additionally assessed in relatively mild oxidative conditions, $p(O_2) = 10^{-3}$ mbar at 600 K for 20 min, with the purpose to explore the effects of oxidation on the honeycomb pattern, see Figure 4.7. For the surface prepared at 450 K

and PA at 600 K, the honeycomb pattern remains, however, solely on the islands, as seen in image **f)**. Interestingly, the surface prepared at 350 K and PA at 700 K, images **g)** – **i)**, have lost the honeycomb pattern and instead forms a new pattern, resembling the network reconstruction shown by Pettersen *et al.* [27], see Figure 1.10, complete with stars, rotors and elbows. None of these features are indicating formation of surface oxides, in contrast to the low coverage surfaces reported by Pettersen [25], seen in Figure 1.6.

Contrastingly, the high coverage surface prepared at 350 K and PA at 600 K has indication of a Moiré pattern. This is particularly visible in Figure 4.7 **c)**. Pettersen [25] found that Moiré patterns are an indicative of formation of oxides and appears mainly with higher Rh content surfaces. When increasing the Pt content, less of the surface will oxidize, as seen by a decrease in visible Moiré pattern. Therefore, our oxidized surfaces where a Moiré pattern is visible, indicates two possibilities: 1) that there are likely high amounts of Rh on the surface, in turn indicating less alloying of Pt and Rh, 2) Rh have remained on the surface and does not go subsurface. In contrast, the Rh/Pt(111) surface shown in images **g)** – **i)** have no formation of a Moiré pattern. Pettersen found that increased alloying with Pt will hinder surface oxide formation, which is a possible explanation as to why the surface PA at 700 K the surface has not formed a Moiré pattern. Additionally, Pettersen found that higher PA temperatures (>700 K) increases the subsurface diffusion of Rh, which may explain why the honeycomb pattern have not formed for the surface in images **g)** – **i)**, as the increased alloying resulted in a lower Rh coverage at the surface than what is necessary for the honeycomb pattern to form (estimated at roughly 1.5 ML in Section A.1). This raises an interesting question: why have the honeycomb pattern retained after PA at higher temperatures, but before oxidation? Further investigation into the effect of oxidation on the honeycomb reconstruction is necessary. The surface prepared at 450 K and PA at 600 K, see images **d)**, **e)**, and **f)**, does also not form any Moiré pattern, despite the same PA temperature used as for the surface prepared at 350 K. Thus, it is theorized that the AP temperature is the determining factor for oxide formation: a lower temperature will hinder a large extent of alloying, allowing oxides to form. A higher AP temperature will induce alloying, therefore preventing oxidation. Further investigation into the oxidized surfaces is necessary to determine when Moiré patterns form, and what hinders and promotes oxide formation.

5.2 Morphology of PtPd surfaces studied in an STM

From our literature search we have experienced that only two studies are reporting on the morphology and mixing of Pd/Pt(111) using the STM, see sections 1.7.1 and 1.7.2. Narihiro *et al.* [28] and Umezawa *et al.* [29] discovered that low coverage Pd/Pt(111) surfaces are dominated by Pd layer formation in a 2D or 3D growth mode, demonstrated by formation of new layers without completion of the former, as opposed to the homo epitaxial 1D layer-by-layer growth that was expected because of the very small lattice mismatch between Pt and Pd (>1.0 %). The cause of the 3D growth is defects in the terraces, which Pd use to nucleate and grow new layers. Both Figure 1.11 and Figure 1.12 clearly show such defects as holes in the terraces for the higher coverage surfaces.

The scarce literature studies investigating the morphology and mixing of Pt/Pd(111) and Pd/Pt(111) using the STM, motivated us to enter this research field, as PtPd alloys are highly relevant as Pt catchment materials in the ammonia oxidation process, see Section 1.4. PtPd surfaces are therefore examined to understand the morphology and Pt/Pd mixing as functions of temperature and coverage for two purposes: 1) to get a better understanding of the surfaces, and 2) examine the ability to be a Pt catchment material.

5.2.1 Pd/Pd(111), Pt/Pd(111), and Pd/Pt(111) surfaces as prepared and post annealed

The Pd(111) single crystal used in this MSc thesis had not been used before at the ReactorSTM lab at UiO. Therefore, a good cleaning procedure had to be developed through experimentation based on cleaning procedures reported in literature [61–68]. Five different cleaning procedures were tested, as seen in Table 3.1. In total, over 30 cleaning cycles were performed before first evaporation on the crystal, namely Pd. Unfortunately, the surface proved to still be unclean, which is especially seen in the STM images in Figure 4.9 image **a)** and **b)**. The cause can be multiple different reasons: 1) too few cleaning cycles, 2) too mild ion sputtering (time, temperature, energy, etc.), 3) too mild annealing (time, temperature, etc.), or a combination. It is most likely too few

cleaning cycles, because new crystals need multiple cleaning cycles before they are considered clean enough to work with. For instance, it would have been helpful to analyse the surface by means of XPS between the cleaning cycles to evaluate cleanliness of the surface with respect to impurity elements. Unfortunately, in our work this step was not possible to carry out as the ReactorSTM was not yet equipped with such a tool when these experiments were carried out. In order to produce good, reliable results, the optimal cleaning procedure with respect to both sputtering- and annealing conditions must be found through experiments, and hopefully in tandem with chemical analysis by means of XPS. Nevertheless, despite not achieving full success in establishing a robust cleaning procedure or a clean crystal, the results gathered from surfaces prepared on Pd(111) will still be used, as some images depicted good, reliable surfaces.

Results obtained from the Pd/Pd(111), Pt/Pd(111), and Pd/Pt(111) surfaces are presented in Sections 4.2.1, 4.2.2, and 4.2.3, respectively. Most interestingly, all three surfaces indicate that islands have grown on top of the defects between the steps and the adhered islands. This highly resembles the 3D growth of Pd/Pt(111) from literature [28,29], because the defects on the terraces induces layer growth of Pd on top of the defects. Preparation of higher coverage Pt/Pd(111) surfaces can determine if this 3D growth mode trend also appears for Pt/Pd(111). The Pt/Pd(111) surface prepared at 475 K shows that at higher AP temperature the islands grow in size and the number of defects increases. In order to determine the trends of morphology and mixing for the Pd/Pd(111) and Pt/Pd(111) surfaces, a meticulous study of the surfaces must be performed. An XPS study of surfaces at similar conditions can be done to determine the surface composition and cleanliness.

Multiple Pd/Pt(111) surfaces have been prepared. The experimental conditions are summarized in Table 3.2, and the results are in Section 4.2.3. In comparison with the Pd/Pd(111) and Pt/Pd(111) surfaces, highly similar topographies are observed. Image **a)** in Figure 4.10 and **b)** and **c)** in Figure 4.11 have the same features as for Pd/Pd(111) and Pt/Pd(111): ad-islands with irregular shapes adhered to the steps, defects on the terraces, but mainly between the steps and the ad-islands. Additionally, some island growth appears on top of defects, and the number of such islands increase with the temperature. The obtained Pd/Pt(111) surfaces are in comparison with the literature on Pd/Pt(111) surfaces [28,29] also highly similar. Our Pd/Pt(111) surfaces may in fact further support the 3D growth observed by Narihiro *et al.* and Umezawa *et al.* In comparison with

Rh/Pt(111) and Pt/Rh(111) surfaces obtained in this thesis (Section 4.1) and in literature ([24,26,27] and [25,27], respectively), no similarities were found. To conclude, all three AP surfaces are highly similar, and additionally highly similar to the found literature [28,29].

In comparison with the straight facets of the triangle and hexagon islands formed for PtRh alloys, no such facets are observed for the PtPd alloys islands. This is accurate for both Pd islands on Pt(111) or Pd(111) and Pt islands on Pd(111). All the islands observed have irregular, rounded morphology.

Two surfaces were subsequently post annealed, see Figure 4.12. Unfortunately, no literature was found to compare our results with. The PA surfaces depicts that the Pd ad-islands either have merged with or separated from the steps in comparison with the AP surfaces. Multiple single islands can be observed on the terraces, as well as multiple smaller islands seemingly randomly scattered on the terraces. Most interestingly, some of the defects have disappeared simultaneously as some defects have grown larger. The larger defects are especially visible at the top of image **b)**. These defects are expected to heal when PA. It is thus hypothesized that the PA temperature may be too low to properly heal the surface. Further investigation is necessary.

5.2.2 Morphology of oxidized Pd/Pt(111) surfaces

The Pd/Pt(111) surfaces after oxidation at 10^{-7} – 10^{-5} mbar surfaces are depicted in Figure 4.13 in Section 4.2.3. All surfaces after oxidation still have defects and the size of the defects depend on the oxidation pressure. The ad-islands connected to the steps have been rounded out, most likely due to the high oxidation temperature, 700 K. From the surface phase diagram for Pd(111) interaction with O_2 in Figure 1.4, a surface oxide ($\sqrt{6}\times\sqrt{6}$) is expected to form during oxidation in a pressure of 10^{-5} Torr = $1.33\cdot10^{-5}$ mbar at a temperature of 700 K, which are the same conditions used for oxidation of the second surface depicted in the figure. However, there are no signs of oxides formed. Likewise, the first depicted surface oxidized at 700 K in a pressure of 10^{-7} mbar is more difficult to compare with the surface phase diagram, because the x-axis stops at around 10^{-5} mbar. However, from a simple crude extrapolation, either chemisorbed oxygen on Pd (O(2×2)) or no oxygen species are expected to form under these conditions. This surface, like the secondly

depicted surface, depicts no features resembling formation of any oxygen species. Despite the surface phase diagram describing oxidation of Pd(111) in an oxygen-gas environment, the diagram can still give some information about the interaction of Pd/Pt(111) with oxygen-gas. However, it is important to be reasonably sceptic to the comparison.

Two papers describing the oxidation of Pd(111) were found [73,74]. The paper published by Rose *et al.* [73] presents low coverage O/Pd(111) surfaces oxidized at low temperatures, between 25 and 60 K, and scanned at temperatures between 30 and 210 K. They discovered chemisorbed oxygen in a (2×2) pattern, which is difficult to compare with the surface phase diagram and is not relevant to the oxidation performed in this paper. The other paper is published by Lundgren *et al.* [74] and presents three Pd(111) surfaces oxidized with an O_2 pressure of $5 \cdot 10^{-6}$ mbar at 573 K for 10 min, which are slightly more relevant conditions. They report formation of a two-dimensional surface oxide, Pd_5O_4. This result agrees with the surface phase diagram, but unfortunately is not comparable to the oxidations in this thesis, particularly as our surfaces have no indication of a surface oxide. No literature was found with oxidation conditions that are directly comparable to the conditions used in this MSc thesis. Thus, the oxidations lead to completely new results which are in conflict with the previously published surface phase diagram, see Figure 1.4. To determine the cause of the discrepancy, further investigation into oxidized Pd(111) and Pd/Pt(111) surfaces using STM are necessary, as well as XPS to determine the composition.

5.3 Chemical state of PtPd surfaces studied with XPS

For the purpose of investigating the properties of PtPd bulk samples as Pt catchment materials, a series of six Pt_xPd_{100-x}, $x = \{0.5, 10, 27, 50, 90, 100\}$ samples, which are shortened to Pt_x or Pt*x*, were analysed in an XPS in UHV conditions, both after cleaning and oxidizing treatments. The experimental information is described in Section 3.2. The following sections will give a quick overview of the six samples and compare the resulting surfaces after the four step treatment.

5.3.1 Overview of the Pt_xPd_{100-x} samples

The oxidation behaviour of six Pt_xPd_{100-x}, $x = \{0.5, 10, 27, 50, 90, 100\}$ samples were studied in four consecutive steps, as presented in Figure 3.2, in the order: 1) cleaning 1, 2) oxidation at 900 °C = 1173 K, 3) cleaning 2, and 4) oxidation at 500 °C = 773 K. The oxidations were performed in 0.21 bar of O_2 for 30 min. The bulk PtPd samples studied in this section differed from the surface films prepared for morphological studies in the STM. However, because both XPS and STM are surface sensitive techniques, some comparisons can still be drawn.

It is important to note that this is a unique study, with respect to investigation into a full series of PtPd alloys by means of XPS analysis in UHV conditions, as well as use of a chemistry cell for chemical treatment at ambient pressure.

5.3.2 Comparing the samples and the treatments

The metallic state of the PtPd samples obtained after cleaning (1 and 2) are in good agreement with the metallic state expected from the surface phase diagram in Figure 1.4. Additionally, the XPS spectra were easy to fit because the Pd metal and Pt metal peaks were in very good agreement with literature.

The samples were slightly different after oxidation at 900 °C = 1173 K. The Pd-O surface phase diagram, see Figure 1.4, describes possible formation of chemisorbed oxygen in a (2×2) pattern, and more improbably formation of a surface oxide. The surface phase diagram does not include the conditions used for XPS in this thesis, therefore, to conclude on the expected surface structures, rough extrapolation of the diagram is necessary. Interestingly, only the Pt0.5 alloy forms a bulk oxide, namely PdO, at these conditions. This is a rather surprising result, as it is relatively little expectation of oxide formation, and only the highest Pd content alloy formed oxide. A hypothesis is therefore that the increased amount of Pd compared to Pt allows for the formation of PdO oxide. No indication of PtO was found. Another interesting observation is that Pt content samples of Pt27 and higher forms chemisorbed oxygen. The surface phase diagram of Pd-O predicts that oxygen can chemisorb to Pd, however this is not observed. Instead, the chemisorbed O is more likely

adsorbed to Pt. The peak for Pt contribution to the chemisorbed O on Pt was, however, not identified. It is hypothesized that the peak is overlapping with the Pt $4f_{7/2}$ metal peak, as described in Section 4.3.2.3. There was not found any indication of formation of the 2D surface oxide Pd_5O_4. A more thorough investigation into the oxidation at 1173 K is essential to determine the cause of the oxide formation and why chemisorbed oxygen appears on Pt and not Pd.

After oxidation at 500 °C = 773 K, all alloys formed oxides, namely Pt0.5, Pt10, Pt27, Pt50, and Pt90. The oxides observed were PdO, PtO, and PtO_2. Additionally, chemisorbed oxygen is formed. The surface phase diagram presented in Figure 1.4 describes that at the conditions used for this oxidation, 773 K in $p(O_2) = 0.21$ bar ≈ 157.5 Torr, bulk oxides are expected to form. In agreement with the expectation, PdO is formed for all five alloys. This is a significant contrast to the alloyed samples after oxidation at 1173 K, where, as mentioned, only Pt0.5 formed any oxide. To fully determine if all PtPd alloys form PdO, an interesting study would be to oxidize the complementary Pt99Pd1 alloy at 773 K to verify whether increased proportion of Pt, higher than the alloy Pt90Pd10 studied in this thesis, will prevent formation of PdO. Absence of PdO in such case would be consistent with the result obtained from the pure Pt reference sample, Pt100, which did not form any oxide. Based on the experimental results, it is concluded that Pd content is a prerequisite for the alloys to oxidize under these conditions.

Surface engineering could benefit from the knowledge on how to tune the amount of the oxides present at the surface. For instance, the two mirror alloys, Pt10 and Pt90, can guide us on how to prepare the alloys depending on whether the objective is to form or not form oxides. For instance, the highest Pt-content alloy, Pt90, forms the highest amount of PtO compared to all other samples. This is logical, because if there is more Pt available, more Pt can be oxidized. Another species formed on the alloys are PtO_2, which only forms for the Pt50 and Pt90 alloys. More interestingly, Pt90 forms the highest amount of PtO_2 compared to Pt50. It is therefore concluded that only higher Pt content alloys can form PtO_2. Additionally, in the temperatures examined in this thesis, PtO_2 is found to be volatile and may evaporate, according to Li *et al.* [75]. Pt should thus not form bulk PtO_2, nevertheless, PtO_2 is observed to increase with higher Pt coverage. It is hypothesized that in order for bulk PtO_2 to be formed, some Pd-oxides have to be present at the surface, additionally proven since the pure Pt100 reference sample had no indication of PtO_2. Furthermore, chemisorbed O formed on Pt may indicate formation of volatile PtO_2 molecules. Further investigation into alloys

with higher Pt-content, for instance Pt99Pd1 and possibly other Pt or Pd alloys, is essential to determine if the trend observed in this study can be generalized to the other bimetallic surfaces, as well as to understand the mechanism for PtO_2 formation. For instance, a similar trend is observed for PtRh oxidized at lower pressures [26].

5.4 Correlations between the surface morphology and the chemical state of PtPd surfaces and bulk

Application of surface sensitive techniques such as STM and XPS to study surface morphology and composition and chemical state, respectively, required a well-defined set of PtPd samples. Unfortunately, the planned extensive study of PtPd alloys in the STM became difficult because of two reasons: 1) the Pd(111) surface was not clean enough, as discussed in Section 5.2.1, and 2) there was a lot of noise during scanning, especially for the Pd/Pt(111) surfaces, also discussed in Section 5.2.1. Furthermore, scanning oxidized surfaces is often difficult, which occurred in this experimental work, however, some good parts of images were obtained for the Pd/Pt(111) and Rh/Pt(111) surfaces, as seen in Figure 4.13 and Figure 4.7. As a result of these difficulties, we were not able to replicate the XPS surfaces to the STM.

Nevertheless, the surface phase diagram in Figure 1.4 allows for some comparison between the surfaces obtained in the XPS and the STM. The diagram gives the expectation that the surface prepared for STM should oxidize, because PtPd surfaces treated in the employed conditions (700 K in $p(O_2) \approx 10^{-5} - 10^{-7}$ Torr)) should result in formation of either a surface oxide or PdO bulk oxide. However, neither of these are formed. The XPS result, on the other hand, closely matched the surface phase diagram. As a result, there are discrepancies between the results obtained from STM and XPS when compared through the surface phase diagram. To resolve these discrepancies, a thorough study of STM alloys prepared with the identical conditions as the XPS alloys should be prioritized. Similarly, the opposite study can be completed too, where the prepared STM alloys can be identically prepared and investigated with an XPS. When the results from the STM and XPS for the PdPt alloys in this study are compared, no correlations could be established. It is

therefore recommended to attempt preparation and close comparison of the results from this extensive XPS study with similar or identical surfaces prepared in STM.

5.5 The use of surface sensitive techniques

In the present MSc thesis, an STM and an XPS are used for structural and compositional identification of PtPd and PtRh surfaces. For more detailed information about the instruments see Sections 2.2.1 and 2.2.2, respectively. The employment of these instruments in the same study is important to gain complementary information about of the surface. Both techniques are surface sensitive, which implies that the information obtained is limited to the top few nanometres of the surface. Additionally, since chemical reactions, e.g. catalytic reactions, take place at the surface, insight into the chemical state and structures at the surface is highly valuable for studying catalysts and surfaces that undergo a chemical transition.

In order to produce reliable results, the norm is to employ instruments with complementary information. This is because the results can be used to either verify each other or give indication of further work necessary to gain a complete understanding of the surface. For instance, multiple papers used as literature references in this thesis have employed multiple instruments. Kibis *et al.* [37] used both XPS and scanning electron microscope (SEM) to study oxidation of Pd, Puglia *et al.* [30] used XPS, AES, and LEED, and two other spectroscopy methods, to study oxidation of Pt, and Zheng *et al.* [24] used STM, XPS, LEED, and AES to evaluate RhPt/Pt(111) surfaces. LEED is often used to verify the cleanliness and formation of oxides for surfaces prepared, annealed, and oxidized in an STM [25], which can be complemented with XPS to evaluate the cleanliness. Another important and generally employed tool to give a whole picture of surfaces is density functional theory (DFT) computations. DFT is used for modelling surfaces and calculating catalytic surface properties, such as reaction rate and product selectivities. For instance, Ma *et al.* [17] used DFT to compare the ammonia oxidation over Pd, Rh, and Pt surfaces. The combination of theoretic modelling and computations, structural experiments, and compositional experiments is important to create a full image of catalytic surfaces.

The use of surface sensitive techniques is often challenging due to the delicate and advanced nature of the equipment and requirement for well-defined (model) samples used. As explained in Sections 2.2.1.2 and 2.2.2.2, an STM is sensitive to internal and external vibrations and higher pressures outside of a chemistry cell, and an XPS is sensitive to magnetic fields, such as the earth's, and higher pressures outside of a chemistry cell. In addition, all instruments can be subjected to faulty equipment, which leads to bad results. In the case of the STM used in this thesis, scanning proved difficult because of two main reasons, as discussed in Section 5.2.1,: 1) the Pd(111) crystal required more cleaning, and 2) multiple instances of electronic interference, particularly for oxidized surfaces and Pd/Pt(111) surfaces. The second reason is more likely related to the STM itself, rather than the human error of insufficient cleaning. There are two likely reasons: 1) the STM was subjected to external vibrations, or 2) internal vibrations. It is not likely that external vibrations are the cause of the noise, because the STM laboratory is located on a floating floor – disconnected fully from the ground. Notably, prior to installation of the STM, the floor was by means of vibration measurements proved to be very solid and free of vibration. This implies further that the vibrations stemming from public transportation should not influence the scanning. Thus, internal vibrations are more likely the cause due to faulty equipment. Since scanning improved after working with the PtPd system, it is difficult to accurately determine the cause of the noise. Oxidized surfaces, however, are known to be difficult to scan in general. Nevertheless, the problems related to scanning experienced in this MSc thesis, accurately depicts the challenges with working with highly sensitive and advanced equipment and instruments.

Surface sensitive techniques are highly relevant in catalytic studies. The chemical reactions occurring during catalysis are contained to the surface and interfaces. Extracting structural and compositional information about the reactions are vital for understanding the mechanisms of these reactions. However, most of traditional surface science instruments are operable in UHV or air at cryogenic or room temperature. Implementation of dedicated chemistry cells or operando ambient/high pressure instrumentation allows for operation at higher pressures and temperatures, bridging the so-called pressure gap and temperature gap. Thus, it is now possible to explore catalytic reactions in realistic or industrially relevant conditions. In this MSc thesis, the preparation of XPS PtPd surfaces oxidized at higher temperatures with an oxygen pressure of 0.21 bar were performed in a chemistry cell. Additionally, both PtPd and PtRh surfaces were oxidized at oxygen pressures from 10^{-7} mbar to 10^{-3} mbar and subsequently scanned. The ability to prepare and

evaluate samples at higher pressures and temperatures are important to move from UHV and low temperature conditions to more realistic pressure and temperature conditions, at which the performance of the surfaces actually will be evaluated and have high importance.

6 Conclusion

Three different experimental topics have been completed in this thesis: 1) study of high coverage Rh/Pt(111) bimetallic surfaces using STM, 2) study of PtPd bimetallic surfaces using STM, and 3) study of a series of PtPd bulk samples in XPS, bare and oxidized at 500 and 900 ℃.

The study of high coverage Rh/Pt(111) bimetallic surfaces in STM resulted in an observation of a new surface reconstruction, named the honeycomb pattern. It formed as a result of post annealing (PA) at both 600 and 700 K, and is proved to have a high temperature stability, as well as forming highly uniformly and continuously over the steps, terraces and islands. It is found to have no similarity to the ad-island reconstruction on Pt/Rh(111) surfaces reported by Pettersen *et al.* [27]. On the other hand, it has some resemblance to the network reconstruction on lower coverage Rh/Pt(111) surfaces, also reported by Pettersen *et al.* [27]. The as prepared (AP) temperature has no observed effect on the formation of the reconstruction. PA at 700 K resulted in larger Rh islands compared to PA at 600 K. The honeycomb pattern is concluded to form only at higher Rh/Pt(111) coverage surfaces, found for 1.5 ML and above, as a result of reconstruction of Rh on the surface. A roadmap was made to summarize the findings of as prepared and post annealed high coverage Rh/Pt(111) surfaces. When lower surface layers are exposed, these layers appear to reconstruct as the network reconstruction mentioned above. Oxidation of the surfaces at a $p(O_2)$ of 10^{-3} mbar gave little to no difference. The surface prepared at 350 K and PA at 600 K has indication of a Moiré pattern in some areas, thus may have been partially oxidized. Notably, the honeycomb pattern had been retained. Oxidation of surfaces after PA at 700 K led to disappearance of the honeycomb pattern completely, and instead formed a new unknown reconstruction, similar to the network reconstruction mentioned above. Thus, it is concluded that oxide formation is dependent on the extent of alloying, governed by the AP temperature.

PtPd surfaces studied in STM was divided into three parts: 1) Pd/Pd(111), 2) Pt/Pd(111), and 3) Pd/Pt(111). Only a few literature references were found on this topic, thereby increasing the difficulty to properly compare with reported results. The Pd(111) surface was, unfortunately, found to not be clean enough after the applied cleaning procedure. Furthermore, the scanning of all the surfaces, particularly Pd/Pt(111), were heavily influenced by electronic interference. Nevertheless,

some good results were obtained. The AP surfaces of all three systems were found to be very similar. The main features are: defects visible as holes in the terraces, irregular ad-islands connected to the steps, and smaller islands on the terraces. The surfaces are highly similar to the reported results on Pd/Pt(111) and the growth mode was proven to be 3D growth mode, as found in literature [28,29]. PA of the Pd/Pt(111) surfaces resulted in no significant difference. The defects formed on the AP surfaces did not heal, and instead seemed to combine into larger holes in the surface. Oxidation of Pd/Pt(111) resulted in rounder islands and even larger defects than observed for the PA surfaces. No oxides were observed formed on the surface, despite the expectation from the Pd-O surface phase diagram. There was not found any relevant literature for oxidation of the PtPd systems.

The XPS study was performed on a series of six PtPd surfaces: Pt_xPd_{100-x} , $x = \{0.5, 10, 27, 50, 90, 100\}$. No similar studies were found at the time of writing. The six surfaces were subjected to four treatments in the following sequence: 1) cleaning 1, 2) oxidation at 900 °C = 1173 K, 3) cleaning 2, and lastly 3) oxidation at 500 °C. The XPS spectra of the surfaces after cleaning did only show metallic Pt and Pd species, thus followed expectation. Oxidation at 900 °C resulted in some chemisorbed O on Pt for higher Pt content samples, Pt27 and higher. Most interestingly, bulk PdO was formed on the lowest Pt content alloy, Pt0.5. None of the other samples had any oxide formed. The formation of PdO is not expected according to the Pd-O surface phase diagram, and O on Pd may form. However, the chemisorbed O were found to be formed on Pt instead. This is hypothesized to indicate formation of PtO_x. Oxidation at 500 °C led to formation of three oxides on the PtPd alloys: Pt_xPd_{100-x}, $x = \{0.5, 10, 27, 50, 90\}$. The oxides found was PdO, PtO, and PtO_2. Both PdO and PtO was formed on the five alloys, in varying degrees. The two higher Pt content alloys, Pt50 and Pt90, were found to additionally contain PtO_2. It was concluded that Pd content was necessary for formation of Pt oxides, supported by the observation of no oxides having formed on the reference sample Pt100 and the high PtO to Pt metal ratio for the lower Pt content alloys. Chemisorbed O on Pt was found to form on Pt50 and higher Pt content alloys and hypothesized to be a precursor to formation of PtO_2. In stark contrast to reported literature at similar conditions, see Table 1.1 for the reported binding energies and species, the surface 2D oxide Pd_5O_4 was not found on any surface, neither during oxidation at 900 nor 500 °C. This is contradictive to the surface phase diagram at these conditions, particularly for oxidation at 500 °C.

Comparison of the PtPd sample results between STM and XPS proved difficult. The results do not indicate any correlation. The samples are prepared and oxidized at different conditions but may have some similarity when compared through the surface phase diagram. Unfortunately, as mentioned earlier, only the bulk PtPd examined by XPS agreed with the surface phase diagram, thereby contributing to the discrepancy between the results. For instance, the PtPd surfaces prepared and examined in STM had no indication of oxidation, while the bulk PtPd samples examined in XPS proved to oxidize in a high degree depending on the conditions employed.

Lastly, the use of the highly sensitive and advanced instruments such as STM and XPS proved to be challenging. No discernible problems were experienced during XPS operation, on the other hand, the STM had multiple detrimental problems, in particular for the PtPd alloys.

7 Perspectives

The MSc work had focus on: 1) high coverage Rh/Pt(111) bimetallic surfaces investigated using STM, 2) PtPd surfaces investigated using STM, and 3) a series of PtPd bulk samples/surfaces investigated using XPS.

The high coverage Rh/Pt(111) surfaces presented a new reconstruction, called honeycomb pattern. The reconstruction is found to be thermally stable over a wide range of both deposition temperature and post annealing temperature. Because this reconstruction was recently discovered, a thorough investigation into understanding the mechanism of the reconstruction should be prioritized. Focus should be placed on varying the AP temperature and the PA temperature to investigate the thermal stability, and examining surfaces prepared at lower Rh coverage to determine the critical surface coverage for the reconstruction to appear (around 1.5 ML). Furthermore, it will aid in completing the roadmap of high coverage Rh/Pt(111) surfaces in Figure 5.1 In order to determine the surface elemental composition of the reconstruction, an XPS study of the identical surfaces prepared in the STM should also be prioritized. Additional oxidation treatments of the surfaces with the honeycomb pattern are necessary to determine if indeed a Moiré pattern is formed, as well as what hinders and promotes the oxide formation, and what effect oxidation has on honeycomb pattern. A series of surface prepared at around 350 K and oxidized at 600 K should be prioritized.

PtPd surfaces were prepared and scanned using an STM. In general, these results were poor, because of high amounts of electronic interference and that the Pd(111) crystal was not clean enough. If further experiments are planned for the Pd(111) crystal, it is firstly important to determine a good and reliable cleaning procedure for the crystal. This mainly includes determining if the employed surface procedure is harsh enough or if more cycles need to be performed. Additionally, now as the ReactorSTM is equipped with an XPS, the cleanliness of the crystal could be evaluated consecutively with the cleaning. The Pt/Pd(111) and Pd/Pt(111) surfaces were found to have either none or very few literary references. A meticulous study of the surfaces should be performed to determine trends of morphology and mixing, as well as to provide a reference for later studies of the systems. This includes varying the coverage and AP and PA temperature to form a large series of surfaces. Furthermore, an XPS study of the surfaces is necessary to determine

the surface composition, which is easier to accomplish with the new XPS installation in place. After post annealing, the surfaces had not been properly healed of the hole defects. Further investigation into different post annealing conditions, for instance over 700 K, can provide an explanation. Lastly, the result obtained from oxidation of Pd/Pt(111) and Pd/Pt(111) in this thesis does not match the expectation from the surface phase diagram in Figure 1.4. These discrepancies could be solved with an STM study and an XPS study into the surfaces at various conditions, both AP, PA, and oxidized.

Finally, PtPd samples were explored with an XPS, both bare and after oxidation at 900 and 500 °C. The Pt0.5 sample appeared to contain PdO after oxidation at 900 °C = 1173 K with $p(O_2)$ = 0.21 bar = 157.5 Torr, however, yielded no Pt-oxide formation. Additionally, some chemisorbed O were found on Pt. Per the surface phase diagram, it is difficult to accurately determine what structures are expected to form, however, crude extrapolation may say chemisorbed O on Pd is expected to form. A thorough investigation into these and similar oxidation conditions is essential to understand why the chemisorbed O is formed on Pt rather than Pd, as well as to understand the PdO formation of the Pt0.5 alloy. Two observed trends for the samples oxidized at 500 °C = 773 K with $p(O_2)$ = 0.21 bar = 157.5 Torr states that: 1) all Pd content alloys form both PdO and PtO, and 2) PtO_2 formation increases with increasing Pt content but is reported to be volatile in the temperature conditions in these experimental works. In order to determine if these trends are reproducible, a higher Pt content sample than Pt90, for instance Pt99Pd1, should be prepared and tested at similar oxidizing conditions. Furthermore, the last trend should be examined in order to determine if it can be generalized to other bimetallic surfaces, as for instance, PtRh oxidized at lower pressures is observed with a similar trend [26].

Comparison of the PtPd results studied in STM and XPS gave clear indication of discrepancies between the results and no observed correlation. For instance, the XPS results were mostly in good agreement with the Pd-O surface phase diagram, while the STM results were not. In fact, no oxides were observed forming on the alloy surfaces in STM. A thorough study is therefore recommended to attempt preparation and close comparison of the results from this extensive XPS study with similar or identical surfaces prepared in STM. Similarly, the STM surfaces should also be studied in the XPS.

Lastly, all the experiments done in this thesis should be complimented with *operando* experiments, preferably *in situ*, which is now possible for XPS because of the new installation of an XPS to the ReactorSTM. The motivation behind the experiments is to understand their mechanism, such that they can be implemented under relevant conditions for industrial processes. The behaviour and the obtained results will differ in higher pressures and temperatures. Especially the bulk samples oxidized in 900 ℃ in the XPS should be performed in higher $p(O_2)$ closer to the pressures used in the process, 1 – 10 bars, to examine the behaviour of the oxygen structures PtO, PtO_2, and O on Pt.

8 Literature

1. Hannevold L, Nilsen O, Kjekshus A, Fjellvåg H. Reconstruction of platinum–rhodium catalysts during oxidation of ammonia. *Appl Catal Gen*. 2005;284(1-2):163-176. doi:10.1016/j.apcata.2005.01.033

2. Fjellvåg AS, Jørgensen PS, Waller D, Wragg DS, Michiel MD, Sjåstad AO. Mechanism of grain reconstruction of Pd and Pd/Ni wires during Pt–catchment. *Materialia*. 2022;21:101359. doi:10.1016/j.mtla.2022.101359

3. Chen S, Perathoner S, Ampelli C, Centi G. Chapter 2 - Electrochemical Dinitrogen Activation: To Find a Sustainable Way to Produce Ammonia. In: Albonetti S, Perathoner S, Quadrelli EA, eds. *Studies in Surface Science and Catalysis*. Vol 178. Horizons in Sustainable Industrial Chemistry and Catalysis. Elsevier; 2019:31-46. doi:10.1016/B978-0-444-64127-4.00002-1

4. Ritchie H, Roser M. Fertilizers. *Our World Data*. Published online October 26, 2013. Accessed February 28, 2022. https://ourworldindata.org/fertilizers

5. Vojvodic A, Medford AJ, Studt F, et al. Exploring the limits: A low-pressure, low-temperature Haber–Bosch process. *Chem Phys Lett*. 2014;598:108-112. doi:10.1016/j.cplett.2014.03.003

6. How fertilizers are made? Fertilizers Europe. Accessed March 29, 2022. https://www.fertilizerseurope.com/fertilizers-in-europe/how-fertilizers-are-made/

7. Ajiwibowo MW, Darmawan A, Aziz M. Towards clean palm oil processing: Integrated ammonia production from empty fruit bunch and palm oil effluent. *J Clean Prod*. 2019;236:117680. doi:10.1016/j.jclepro.2019.117680

8. Giddey S, Badwal SPS, Kulkarni A. Review of electrochemical ammonia production technologies and materials. *Int J Hydrog Energy*. 2013;38(34):14576-14594. doi:10.1016/j.ijhydene.2013.09.054

9. Clark J. The Haber Process. Chemistry LibreTexts. Published August 15, 2020. Accessed April 25, 2022. https://chem.libretexts.org/Bookshelves/Physical_and_Theoretical_Chemistry_Textbook_Maps/Supplemental_Modules_(Physical_and_Theoretical_Chemistry)/Equilibria/Le_Chateliers_Principle/The_Haber_Process

10. Jones AV, Higton A, Clemmet M, Golding E. *Access to Chemistry*.; 1999. doi:10.1039/9781847550040

11. *N-Fertilizer, Where Does It Come From?*; 2017. Accessed March 7, 2022. https://www.youtube.com/watch?v=QEz2nyHO3fA

12. How we make our fertilizer | Yara International. Yara None. Published January 10, 2018. Accessed February 28, 2022. https://www.yara.com/crop-nutrition/why-fertilizer/production-of-fertillizer/

13. The Nobel Prize in Chemistry 1909. NobelPrize.org. Accessed March 9, 2022. https://www.nobelprize.org/prizes/chemistry/1909/ostwald/facts/

14. Krähnert R. Ammonia Oxidation over Polycrystalline Platinum: Surface Morphology and Kinetics at Atmospheric Pressure. Published online December 23, 2005. doi:10.14279/depositonce-1270

15. Inger M, Dobrzyńska-Inger A, Rajewski J, Wilk M. Optimization of Ammonia Oxidation Using Response Surface Methodology. *Catalysts*. 2019;9(3):249. doi:10.3390/catal9030249

16. Ammonia oxidation pathways and nitrifier denitrification are significant sources of N2O and NO under low oxygen availability. doi:10.1073/pnas.1219993110

17. Ma H, Schneider WF. DFT and microkinetic comparison of Pt, Pd and Rh-catalyzed ammonia oxidation. *J Catal*. 2020;383:322-330. doi:10.1016/j.jcat.2020.01.029

18. Kamphus DM. Emission monitoring in nitric acid plants. Published online 2014:6.

19. Fjellvåg AS, Waller D, Skjelstad J, Sjåstad AO. Grain Reconstruction of Palladium and Palladium-Nickel Alloys for Platinum Catchment. *Johns Matthey Technol Rev*. 2019;63(4):236-246. doi:10.1595/205651319X15597236291099

20. Holzmann DH. Platinum Recovery in Ammonia Oxidation Plants. Published online 1969:7.

21. Hessevik J, Fjellvåg AS, Iveland O, et al. LaNiO3 as a Pt catchment material in the ammonia oxidation process. *Mater Today Commun*. 2022;33:104084. doi:10.1016/j.mtcomm.2022.104084

22. Massalski TB, Murray JL, Bennett LH, Baker H. *Binary Alloy Phase Diagrams: Vol. 1 : Ac-Au to Fe-Rh*. Vol Vol. 1. American Society for Metals; 1986.

23. Ketteler G, Ogletree DF, Bluhm H, Liu H, Hebenstreit ELD, Salmeron M. In Situ Spectroscopic Study of the Oxidation and Reduction of Pd(111). *J Am Chem Soc*. 2005;127(51):18269-18273. doi:10.1021/ja055754y

24. Zheng J, Ivashenko O, Fjellvåg H, Groot IMN, Sjåstad AO. Roadmap for Modeling RhPt/Pt(111) Catalytic Surfaces. *J Phys Chem C*. 2018;122(46):26430-26437. doi:10.1021/acs.jpcc.8b08124

25. Pettersen C. *Preparation, Characterization and Oxidation of Nanostructured Pt-Rh Surfaces*. 2020.

26. Ivashenko O, Johansson N, Pettersen C, et al. How Surface Species Drive Product Distribution during Ammonia Oxidation: An STM and Operando APXPS Study. *ACS Catal*. 2021;11(13):8261-8273. doi:10.1021/acscatal.1c00956

27. Pettersen C, Sjåstad AO, Ivashenko O. Near-Surface Alloys of PtRh on Rh(111) and Pt(111) Characterized by STM. *J Phys Chem C*. 2021;125(45):25140-25147. doi:10.1021/acs.jpcc.1c05627

28. Narihiro E, Umezawa K, Ohira Y, Yoshimura M. Scanning Tunneling Microscopy Study of Pd Adsorption on Pt(111). *Jpn J Appl Phys*. 2007;46(8B):5595-5597. doi:10.1143/JJAP.46.5595

29. Umezawa K, Narihiro E, Ohta Y, Ohira Y, Yoshimura M. Pd/Pt(111) surface structure and metal epitaxy by time-of-flight impact-collision ion scattering spectroscopy and scanning tunneling microscopy: Does lattice mismatch really determine the growth mode? *Nucl Instrum Methods Phys Res Sect B Beam Interact Mater At*. 2008;266(8):1903-1907. doi:10.1016/j.nimb.2008.01.050

30. Puglia C, Nilsson A, Hernnäs B, Karis O, Bennich P, Mårtensson N. Physisorbed, chemisorbed and dissociated O2 on Pt(111) studied by different core level spectroscopy methods. *Surf Sci*. 1995;342(1-3):119-133. doi:10.1016/0039-6028(95)00798-9

31. Miller DJ, Öberg H, Kaya S, et al. Oxidation of Pt(111) under Near-Ambient Conditions. *Phys Rev Lett*. 2011;107(19):195502. doi:10.1103/PhysRevLett.107.195502

32. Parkinson CR, Walker M, McConville CF. Reaction of atomic oxygen with a Pt() surface: chemical and structural determination using XPS, CAICISS and LEED. *Surf Sci*. 2003;545(1-2):19-33. doi:10.1016/j.susc.2003.08.029

33. Shyu JZ, Otto K. Identification of platinum phases on γ-alumina by XPS. *Appl Surf Sci*. 1988;32(1):246-252. doi:10.1016/0169-4332(88)90085-2

34. Zemlyanov D, Aszalos-Kiss B, Kleimenov E, et al. In situ XPS study of Pd(111) oxidation. Part 1: 2D oxide formation in 10−3mbar O2. *Surf Sci*. 2006;600(5):983-994. doi:10.1016/j.susc.2005.12.020

35. Gabasch H, Unterberger W, Hayek K, et al. In situ XPS study of Pd(111) oxidation at elevated pressure, Part 2: Palladium oxidation in the 10−1mbar range. *Surf Sci*. 2006;600(15):2980-2989. doi:10.1016/j.susc.2006.05.029

36. Titkov AI, Salanov AN, Koscheev SV, Boronin AI. Mechanisms of Pd(110) surface reconstruction and oxidation: XPS, LEED and TDS study. *Surf Sci*. 2006;600(18):4119-4125. doi:10.1016/j.susc.2006.01.131

37. Kibis LS, Titkov AI, Stadnichenko AI, Koscheev SV, Boronin AI. X-ray photoelectron spectroscopy study of Pd oxidation by RF discharge in oxygen. *Appl Surf Sci*. 2009;255(22):9248-9254. doi:10.1016/j.apsusc.2009.07.011

38. Otto K, Haack LP, deVries JE. Identification of two types of oxidized palladium on γ-alumina by X-ray photoelectron spectroscopy. *Appl Catal B Environ*. 1992;1(1):1-12. doi:10.1016/0926-3373(92)80003-I

39. Militello MC, Simko SJ. Palladium Oxide (PdO) by XPS. *Surf Sci Spectra*. 1994;3(4):395-401. doi:10.1116/1.1247784

40. Militello MC, Simko SJ. Elemental Palladium by XPS. *Surf Sci Spectra*. 1994;3(4):387-394. doi:10.1116/1.1247783

41. Nyholm R, Berndtsson A, Martensson N. Core level binding energies for the elements Hf to Bi (Z=72-83). *J Phys C Solid State Phys*. 1980;13(36):L1091-L1096. doi:10.1088/0022-3719/13/36/009

42. Banse BA, Koel BE. Interaction of oxygen with Pd(111): High effective O 2 pressure conditions by using nitrogen dioxide. *Surf Sci*. 1990;232(3):275-285. doi:10.1016/0039-6028(90)90120-W

43. Smirnov MYu, Klembovskii IO, Kalinkin AV, Bukhtiyarov VI. An XPS Study of the Interaction of a Palladium Foil with NO2. *Kinet Catal*. 2018;59(6):786-791. doi:10.1134/S0023158418060150

44. Leng Y. *Materials Characterization: Introduction to Microscopic and Spectroscopic Methods*. 2nd edition. Wiley-VCH; 2013.

45. Kittel C. *Introduction to Solid State Physics*. 8th ed. Wiley; 2005.

46. Kibler LA. *Preparation and Characterization of Noble Metal Single Crystal Electrode Surfaces*.; 2003.

47. Chegg.com. Accessed November 1, 2022. https://www.chegg.com/homework-help/questions-and-answers/2-surface-energy-single-crystal-depends-crystallographic-orientation-respect-surface-expla-q26513856

48. epitaxy | crystallography | Britannica. Accessed October 30, 2022. https://www.britannica.com/science/epitaxy

49. Fu JX. *Coherent near Infrared Photodetection with Indium Gallium Arsenide Based Optoelectronic Devices /*. 2005.

50. Silicon Based Epitaxial Thin Films. Accessed October 30, 2022. https://www.mks.com/n/silicon-epitaxial-thin-films

51. Stevie FA, Garcia R, Shallenberger J, Newman JG, Donley CL. Sample handling, preparation and mounting for XPS and other surface analytical techniques. *J Vac Sci Technol A*. 2020;38(6):063202. doi:10.1116/6.0000421

52. Venables JA. *Introduction to Surface and Thin Film Processes*. 1st ed. Cambridge University Press; 2000. doi:10.1017/CBO9780511755651

53. El-Henawey MI, Kubas M, El-Shaer A, Salim E. The effect of post-annealing treatment on the structural and optoelectronic properties of solution-processed TiO2 thin films. *J Mater Sci Mater Electron*. 2021;32(16):21308-21317. doi:10.1007/s10854-021-06633-8

54. Over H, Seitsonen AP. Oxidation of Metal Surfaces. *Science*. 2002;297(5589):2003-2005. doi:10.1126/science.1077063

55. Rogers B, Adams J, Pennathur S. *Nanotechnology: Understanding Small Systems*. 3rd ed. CRC; 2015.

56. Frenken J, Groot I. *Operando Research in Heterogeneous Catalysis*. Vol 114. Springer International Publishing AG; 2017. doi:10.1007/978-3-319-44439-0

57. tunneling | physics | Britannica. Accessed August 26, 2022. https://www.britannica.com/science/tunneling

58. van Spronsen MA, Frenken JWM, Groot IMN. Observing the oxidation of platinum. *Nat Commun*. 2017;8(1):429. doi:10.1038/s41467-017-00643-z

59. Sjåstad AO, Ivashenko O. The Reactor STM - Department of Chemistry. Accessed August 31, 2022. https://www.mn.uio.no/kjemi/english/research/groups/nafuma/laboratories/operando-methods/the-reactor-stm/index.html

60. Diplas S. X-ray photoelectron spectroscopy - An introduction. Presented at: 2017.

61. Engstfeld AK, Hoster HE, Behm RJ. Formation, atomic distribution and mixing energy in two-dimensional PdxAg1−x surface alloys on Pd(111). *Phys Chem Chem Phys*. 2012;14(30):10754. doi:10.1039/c2cp41104k

62. Højrup Hansen K, Šljivančanin Ž, Hammer B, Lægsgaard E, Besenbacher F, Stensgaard I. An STM and DFT study of the ordered structures of NO on Pd(). *Surf Sci*. 2002;496(1-2):1-9. doi:10.1016/S0039-6028(01)01620-X

63. Rose MK, Borg A, Mitsui T, Ogletree DF, Salmeron M. Subsurface impurities in Pd(111) studied by scanning tunneling microscopy. *J Chem Phys*. 2001;115(23):10927-10934. doi:10.1063/1.1420732

64. Klikovits J, Napetschnig E, Schmid M, et al. Surface oxides on Pd(111): STM and density functional calculations. *Phys Rev B*. 2007;76(4):045405. doi:10.1103/PhysRevB.76.045405

65. Weirum G, Kratzer M, Koch HP, et al. Growth and Desorption Kinetics of Ultrathin Zn Layers on Pd(111). *J Phys Chem C*. 2009;113(22):9788-9796. doi:10.1021/jp9017376

66. Vang RT, Wang JG, Knudsen J, et al. The Adsorption Structure of NO on Pd(111) at High Pressures Studied by STM and DFT. *J Phys Chem B*. 2005;109(30):14262-14265. doi:10.1021/jp052519t

67. Leisenberger FP, Koller G, Sock M, et al. Surface and subsurface oxygen on Pd(111). *Surf Sci*. 2000;445(2-3):380-393. doi:10.1016/S0039-6028(99)01084-5

68. Zheng G, Altman EI. The oxidation of Pd(111). *Surf Sci*. 2000;462(1-3):151-168. doi:10.1016/S0039-6028(00)00599-9

69. Horcas I, Fernández R, Gómez-Rodríguez JM, Colchero J, Gómez-Herrero J, Baro AM. WSXM: A software for scanning probe microscopy and a tool for nanotechnology. *Rev Sci Instrum*. 2007;78(1):013705. doi:10.1063/1.2432410

70. Least-Squares Curve Fitting Program Winspec. Published online 2001.

71. Origin 2021b. Published online 2021. Accessed November 1, 2022. https://www.originlab.com/

72. Moulder JF, Chastain J. *Handbook of X-Ray Photoelectron Spectroscopy: A Reference Book of Standard Spectra for Identification and Interpretation of XPS Data*. Physical Electronics; 1995.

73. Rose MK, Borg A, Dunphy JC, Mitsui T, Ogletree DF, Salmeron M. Chemisorption of atomic oxygen on Pd(111) studied by STM. *Surf Sci*. 2004;561(1):69-78. doi:10.1016/j.susc.2004.04.037

74. Lundgren E, Kresse G, Klein C, et al. Two-Dimensional Oxide on Pd(111). *Phys Rev Lett*. 2002;88(24):246103. doi:10.1103/PhysRevLett.88.246103

75. Li T, Bagot PAJ, Marquis EA, Edman Tsang SC, Smith GDW. Atomic engineering of platinum alloy surfaces. *Ultramicroscopy*. 2013;132:205-211. doi:10.1016/j.ultramic.2012.10.012

A Appendix

A.1 Coverage estimation

Based on estimations from the experimental data of coverages of prepared Rh/Pt(111) surfaces in the paper by Pettersen *et al.* [27], it is possible to estimate the Rh/Pt(111) surfaces in this MSc thesis. In the paper, 16 min of Rh evaporation at a flux of 8 nA on Pt(111) gave 1 ML. If a linear coverage increase is assumed, 24 and 32 min of an 8 nA flux Rh deposition should result in 1.5 and 2 ML of Rh/Pt(111), respectively. Based on the obtained Rh/Pt(111) surfaces in Figure 4.2, where the effect of deposition time of 24 and 32 min is compared, there are little to no observed difference, even after post annealing and oxidation. Henceforth, the surfaces were assumed to have a similar coverage. Because this estimation suggests otherwise, it is important to properly estimate the coverage of the obtained Rh/Pt(111) surfaces, as well as the other obtained surfaces in this thesis.

A.2 Additional PtPd STM images

In this section, STM images of Pt/Pd(111) as prepared, post annealed, and oxidized are presented, as they were not collected by the writer of this thesis, but a supervisor. However, the images are highly relevant to the previously reported in Section 4.2.2 because of the matching conditions. The surface was prepared at 425 K for 15 min with a flux of 12 nA, then subsequently post annealed at 775 K for 30 min and oxidized at 775 K for 30 min in a $p(O_2)$ of $2 \cdot 10^{-7}$ mbar. As can be seen by the Pt/Pd(111) surface presented in Figure A.8.1, the as prepared surfaces are similar to the other reported results of Pt/Pd(111) surfaces. Post annealing (PA) of the surface lead to formation of small rhombuses covering the entire surface. This appears as a reconstruction, and is similar to the observed spoked wheel structure and seen in Figure 2.3 [58].

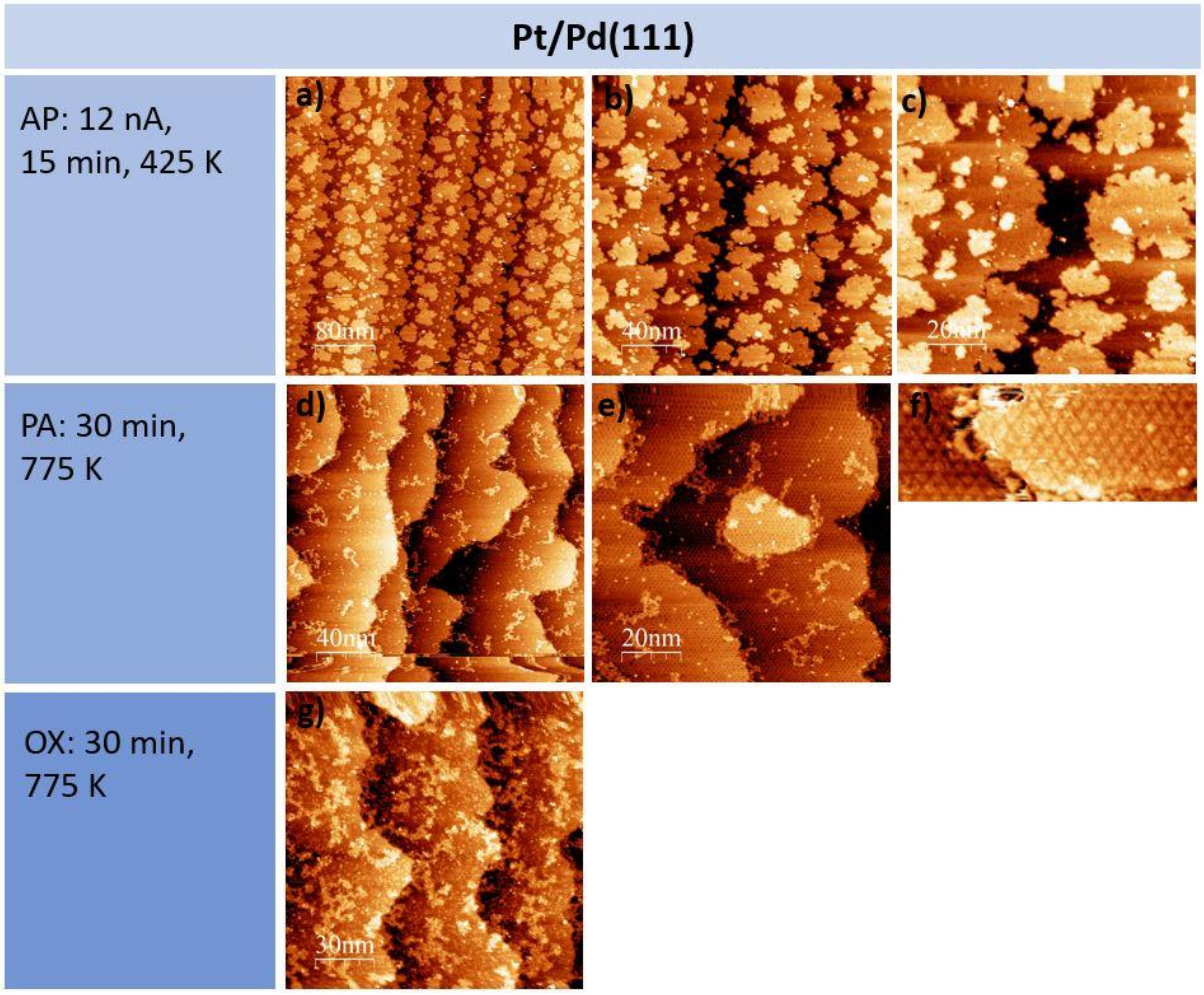

Figure A.8.1: STM images of a Pt/Pd(111) surface after preparation at 425 K for 15 min with a flux of 12 nA. Subsequent post annealing (PA) was performed at 775 K for 30 min, and the oxidation (OX) at 775 K for 30 min. The $p(O_2)$ was $2 \cdot 10^{-7}$ mbar.